

VOLUME 39

MARCH 1961

NUMBER 3

# Canadian Journal of Physics

*Editor:* H. E. DUCKWORTH

*Associate Editors:*

L. G. ELLIOTT, *Atomic Energy of Canada, Ltd., Chalk River*  
J. S. FOSTER, *McGill University*  
G. HERZBERG, *National Research Council of Canada*  
L. LEPRINCE-RINGUET, *Ecole Polytechnique, Paris*  
B. W. SARGENT, *Queen's University*  
G. M. VOLKOFF, *University of British Columbia*  
W. H. WATSON, *University of Toronto*  
G. A. WOONTON, *McGill University*

*Published by* THE NATIONAL RESEARCH COUNCIL  
OTTAWA CANADA

## CANADIAN JOURNAL OF PHYSICS

Under the authority of the Chairman of the Committee of the Privy Council on Scientific and Industrial Research, the National Research Council issues THE CANADIAN JOURNAL OF PHYSICS and five other journals devoted to the publication, in English or French, of the results of original scientific research. Matters of general policy concerning these journals are the responsibility of a joint Editorial Board consisting of: members representing the National Research Council of Canada; the Editors of the Journals; and members representing the Royal Society of Canada and four other scientific societies.

### EDITORIAL BOARD

#### Representatives of the National Research Council

I. McT. Cowan (Chairman), *University of British Columbia*  
Léo Marion, *National Research Council*

H. G. Thode, *McMaster University*  
D. L. Thomson, *McGill University*

#### Editors of the Journals

D. L. Bailey, *University of Toronto*  
T. W. M. Cameron, *Macdonald College*  
F. E. Chase, *Ontario Agricultural College*  
H. E. Duckworth, *McMaster University*

Léo Marion, *National Research Council*  
J. F. Morgan, *Department of National Health and Welfare, Ottawa*  
J. A. F. Stevenson, *University of Western Ontario*

#### Representatives of Societies

D. L. Bailey, *University of Toronto*  
Royal Society of Canada  
T. W. M. Cameron, *Macdonald College*  
Royal Society of Canada  
H. E. Duckworth, *McMaster University*  
Royal Society of Canada  
Canadian Association of Physicists  
P. R. Gendron, *University of Ottawa*  
Chemical Institute of Canada

D. J. Le Roy, *University of Toronto*  
Royal Society of Canada  
J. F. Morgan, *Department of National Health and Welfare, Ottawa*  
Canadian Biochemical Society  
R. G. E. Murray, *University of Western Ontario*  
Canadian Society of Microbiologists  
J. A. F. Stevenson, *University of Western Ontario*  
Canadian Physiological Society

#### Ex officio

Léo Marion (Editor-in-Chief), *National Research Council*  
J. B. Marshall (Administration and Awards), *National Research Council*

*Manuscripts* for publication should be submitted to Dr. H. E. Duckworth, Editor, Canadian Journal of Physics, Hamilton College, McMaster University, Hamilton, Ontario.

For instructions on preparation of copy, see **NOTES TO CONTRIBUTORS** (back cover).

*Proof, correspondence concerning proof, and orders for reprints* should be sent to the Manager, Editorial Office (Research Journals), Division of Administration and Awards, National Research Council, Ottawa 2, Canada.

*Subscriptions, renewals, requests for single or back numbers, and all remittances* should be sent to Division of Administration and Awards, National Research Council, Ottawa 2, Canada. Remittances should be made payable to the Receiver General of Canada, credit National Research Council.

The journals published, frequency of publication, and subscription prices are:

Canadian Journal of Biochemistry and Physiology	Monthly	\$9.00 a year
Canadian Journal of Botany	Bimonthly	\$6.00 a year
Canadian Journal of Chemistry	Monthly	\$12.00 a year
Canadian Journal of Microbiology	Bimonthly	\$6.00 a year
Canadian Journal of Physics	Monthly	\$9.00 a year
Canadian Journal of Zoology	Bimonthly	\$5.00 a year

The price of regular single numbers of all journals is \$2.00.







# Canadian Journal of Physics

Issued by THE NATIONAL RESEARCH COUNCIL OF CANADA

VOLUME 39

MARCH 1961

NUMBER 3

## PRODUCTION OF $\text{Lu}^{178}$ BY THE $\text{Ta}^{181}(n, \alpha)\text{Lu}^{178}$ REACTION IN THE NRX REACTOR<sup>1</sup>

P. GLENTWORTH<sup>2</sup> AND R. H. BETTS

### ABSTRACT

A rare earth activity of half-life  $19 \pm 1$  min, produced by irradiating tantalum in the fast neutron flux of the NRX reactor has been shown to be a lutetium nuclide. The  $19 \pm 1$  min activity was ascribed to  $\text{Lu}^{178}$  produced by the  $\text{Ta}^{181}(n, \alpha)\text{Lu}^{178}$  reaction. Three  $\gamma$  rays of  $450 \pm 15$  kev,  $320 \pm 15$  kev, and  $680 \pm 15$  kev (very weak) are associated with the  $19 \pm 1$  min  $\text{Lu}^{178}$  activity.

### INTRODUCTION

At the start of this work two attempts to produce  $\text{Lu}^{178}$  had been reported in the literature: Butement (1951) and Stribel (1957). Butement irradiated hafnium with  $\gamma$  rays of energies up to 23 Mev, and observed an activity of 22-min half-life which he tentatively ascribed to  $\text{Lu}^{178}$  produced by a  $(\gamma, p)$  reaction on hafnium. Stribel bombarded a tantalum target with 14-Mev neutrons and produced a  $18 \pm 0.5$  min activity which had  $\gamma$  rays of 342 kev, 445 kev, and 550 kev (very weak) associated with it. Chemical identification of the  $18 \pm 0.5$  min activity was not carried out, but Stribel proposed that the probability of producing a short-lived nuclide other than  $\text{Lu}^{178}$  was very low. Recently, two further investigations have been published: Aten and Funke-Klopper (1960), and Poularikas *et al.* (1960). Both groups of workers produced a 22-min activity by fast neutron bombardments of  $\text{Ta}^{181}$ , and ascribed it to  $\text{Lu}^{178}$  on the basis of the yields observed. Poularikas *et al.* reported the following photopeaks to be associated with this 22-min activity:  $327 \pm 15$  kev,  $434 \pm 15$  kev,  $560 \pm 30$  kev,  $674 \pm 30$  kev, and  $780 \pm 30$  kev. None of the papers reported to date have chemically identified the 22-min activity as a lutetium isotope.

In the work reported here, the NRX reactor was used as a source of  $\geq 14$  Mev neutrons. Roy and Wuschke (1959) have shown that for the irradiation position used the flux of neutrons having energies in excess of 14 Mev is approximately  $1 \times 10^9$  neutrons/cm<sup>2</sup> sec. Tantalum metal was the target. It was irradiated under cadmium to reduce the level of extraneous radionuclides

<sup>1</sup>Manuscript received November 28, 1960.

Contribution from the Research Chemistry Branch, Atomic Energy of Canada Limited, Chalk River, Ontario.

Issued as A.E.C.L. No. 1166.

<sup>2</sup>N.R.C. Fellow 1959-60. Present address: Department of Chemistry, Leeds University, Leeds 2, England.

arising from thermal neutron capture in impurities in the tantalum. After the irradiation, very rigorous chemical procedures were used to isolate and purify a lutetium fraction. Finally, the radioactive decay of this fraction was followed by both  $\beta$ - and  $\gamma$ -counting methods.

#### EXPERIMENTAL

The tantalum target, approximately 1 gram of metal, was irradiated in an empty fuel-rod position in the NRX reactor for 1 hour. It was contained inside a 0.030-in. thick cadmium container to reduce the flux of thermal neutrons, and hence the radioactivities produced by thermal neutron capture in impurities.

After the irradiation, the tantalum was dissolved in a mixture of concentrated hydrofluoric and nitric acids and 2 mg of thulium as a rare earth carrier was added. The rare earth fluoride precipitate was centrifuged out, and dissolved in a mixture of concentrated nitric acid and saturated boric acid. The rare earth hydroxide was precipitated by addition of concentrated ammonium hydroxide, centrifuged off, and washed with dilute ammonia before being taken into solution with about 1 ml of 15 *N* nitric acid. The total rare earth fraction was extracted into tributylphosphate and then back-extracted from the tributylphosphate into water. The rare earth hydroxide was precipitated from the aqueous solution with a few drops of ammonium hydroxide, centrifuged out, and then dissolved in 1–2 ml of 0.1 *N* HCl. The lutetium fraction was separated from the total rare earth fraction by ion-exchange techniques similar to those employed by Choppin and Silva (1956).

In the ion-exchange procedure, a 0.4 *M* solution of  $\alpha$ -hydroxyisobutyric acid, pH = 3.6, was used to elute the lutetium fraction from a 16% cross-linked Dowex-50 ion-exchange column, 20 cm long by 0.2 cm diameter. The ion-exchange column was maintained at 87° C. The Dowex-50 resin was in the ammonium form and had been graded by water flotation to obtain particles which settled at between 0.3–0.5 cm/minute. An elapsed time of 2½ hours from the end of the irradiation was required to isolate the lutetium fraction from the irradiated target.

The decay of the activities referred to below was determined with a methane-flow proportional  $\beta$ -counter. Measurements of  $\gamma$  rays were made with a 3×3 in. NaI (Tl-activated) crystal optically coupled to a photomultiplier in connection with a 100-channel pulse height analyzer.

#### RESULTS AND DISCUSSION

Figure 1 is a typical decay curve of a sample from the lutetium peak eluted from the ion-exchange column, and is resolved into three components of half-lives  $19 \pm 1$  min, 3.6 hr, and 6.8 days. The latter two activities were identified as  $\text{Lu}^{176}$  and  $\text{Lu}^{177}$ , respectively, by their half-lives and  $\gamma$ -ray spectra. The formation of these nuclides indicates the fortuitous presence of lutetium impurity in the tantalum, since it is inconceivable that  $\text{Lu}^{176}$  and  $\text{Lu}^{177}$  could have been produced by neutron irradiation of tantalum. However, their presence in the same fraction with the 19-min activity clearly demonstrates that the latter activity is also a lutetium nuclide.

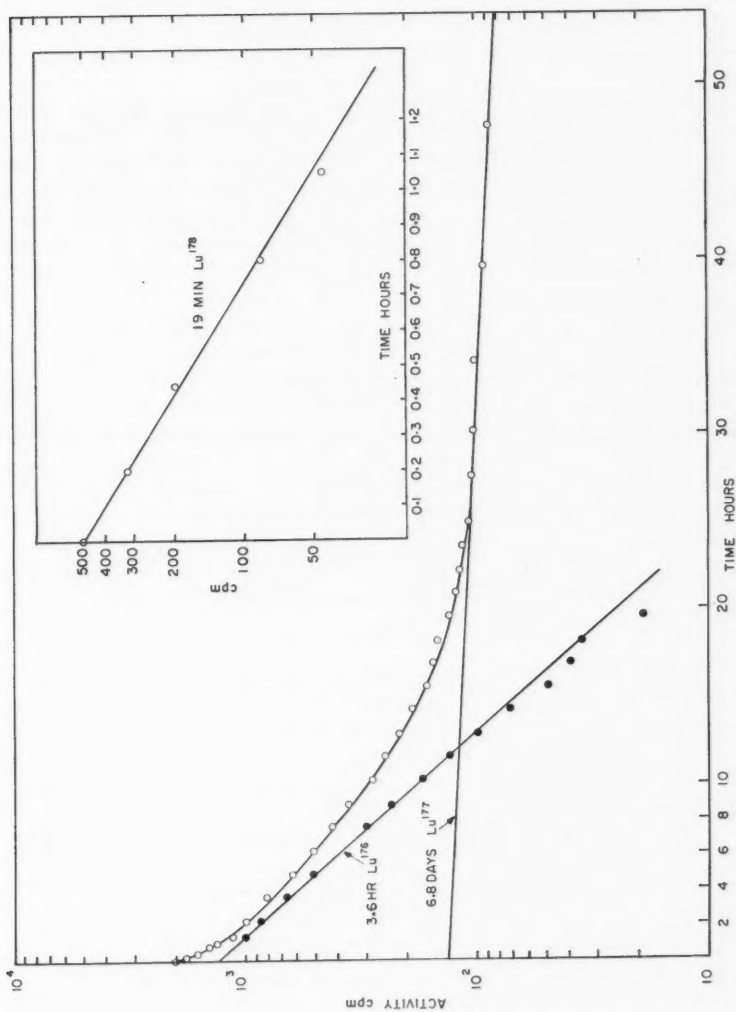


FIG. 1. Radioactive decay of lutetium fraction.

In principle, two alternate modes of formation of the 19-min activity are available. The first, involving successive neutron capture in  $\text{Lu}^{176}$ , may be dismissed on the grounds that separate irradiations of pure lutetium failed to produce a 19-min activity. The second alternative, involving the reaction  $\text{Ta}^{181}(n, \alpha)\text{Lu}^{178}$ , appears to be the only likely source of this activity. It is concluded therefore that the  $19 \pm 1$  min activity observed in this work is  $\text{Lu}^{178}$ .

The gamma-ray spectrum of the lutetium fraction showed that the decay of the 19-min activity was associated with peaks of energies  $450 \pm 15$  kev,  $320 \pm 15$  kev, and possibly a weak  $\gamma$  ray at  $680 \pm 15$  kev. These gamma rays are similar in energy to those reported by Poularikas *et al.* (1960); the failure in the present work to detect the 560-kev and 780-kev photopeaks may have been attributable to the low activity of the  $\text{Lu}^{178}$  fraction, which was the result of the elapse of 6-7 half-lives before isolation of the lutetium fraction from the irradiated tantalum.

#### ACKNOWLEDGMENTS

One of the authors, P. Glentworth, is indebted to the National Research Council of Canada for a Postdoctoral Fellowship (1959-60), and to Atomic Energy of Canada Limited, in whose laboratories this work was carried out.

#### REFERENCES

- ATEN, A. H. W. and FUNKE-KLOPPER, A. G. 1960. *Physica*, **26**, 79.  
BUTEMENT, F. D. S. 1951. *Proc. Phys. Soc. (London)*, A, **64**, 395.  
CHOPPIN, G. R. and SILVA, R. J. 1956. *J. Inorg. & Nuclear Chem.* **3**, 153.  
POULARIKAS, A., CUNNINGHAM, J., McMILLAN, W., McMILLAN, J., and FINK, R. W. 1960. *J. Inorg. & Nuclear Chem.* **13**, 196.  
ROY, J. C. and WUSCHKE, D. 1959. A.E.C.L. Report No. 877.  
STRIBEL, T. 1957. *Z. Naturforsch.* **12a**, 519.

# THE ROLE OF REPULSIVE CORES IN THE PHOTONUCLEAR EFFECT<sup>1</sup>

JOHN W. CLARK

## ABSTRACT

The dipole sum rule is used to investigate the effect of nuclear forces on the integrated photonuclear cross section  $\sigma_{\text{int}}$  of a large nucleus, for a Serber potential containing a hard core. A Jastrow wave function is assumed to describe the nuclear ground state, and the first term in the cluster expansion of the resultant expression for  $\sigma_{\text{int}}$  evaluated under two different sets of assumptions for the potential and correlation function, corresponding to two different studies of the nuclear matter problem. The presence of a repulsive core in the potential is found to enhance considerably the calculated  $\sigma_{\text{int}}$ , compared with the result for a potential without a core which fits the same (low-energy) two-nucleon data.

## INTRODUCTION

For several years it has been common practice to base studies of the nuclear photoeffect on certain sum rules, which express a given moment

$$(1) \quad \sigma_m = \int \sigma(E) E^m dE$$

of the photon absorption cross section in terms of the expectation value of an appropriate operator in the nuclear ground state. Here  $E$  is the photon energy and the integral extends over all  $E$ . The particular sum rule that interests us is the dipole sum rule for the integrated cross section,

$$(2) \quad \sigma_0 \equiv \sigma_{\text{int}} = \int \sigma(E) dE.$$

Under the assumption that the neutron-proton potential  $v_{np}$  is

$$(3) \quad v_{np} = (1-x+xP_{np})w_{np},$$

where  $x$  is the fraction of Majorana exchange and  $P_{np}$  the Majorana exchange operator, and  $w_{np}$  is an unspecified static potential (possibly spin dependent), one may show (Levinger and Bethe 1950) that in the dipole approximation

$$(4) \quad \sigma_{\text{int}} = \frac{2\pi e^2 \hbar}{Mc} \frac{(A-Z)Z}{A} (1+\mathcal{C}x),$$

where the "exchange correction"  $\mathcal{C}$  is given quite well by

$$(5) \quad \mathcal{C} = -\frac{2M}{\hbar^2} \frac{1}{6} \int \Psi_0^* \sum_n \sum_p r_{np}^2 w_{np} P_{np} \Psi_0 / \int \Psi_0^* \Psi_0$$

for  $Z \approx A/2$ . The integral sign in this last expression implies integrations over the space co-ordinates  $\mathbf{r}_1, \dots, \mathbf{r}_A$  and sums over the spin variables  $s_1, \dots, s_A$  of the  $A$  nucleons  $1, \dots, A$ .  $\sum_n$  extends over all  $A-Z$  neutron indices, and  $\sum_p$  over all  $Z$  proton indices.  $r_{np}$  is the neutron-proton separation and  $M$  the nucleon mass.  $\Psi_0$  is the *ground-state* wave function of the nucleus.

<sup>1</sup>Manuscript received October 31, 1960.

Contribution from Palmer Physical Laboratory, Princeton University, Princeton, N.J.

Most earlier calculations of  $\sigma_{\text{int}}$  for complex nuclei have been made on the basis of a nuclear ground-state wave function appropriate to some independent-particle model (in particular, the Fermi gas model (Levinger and Bethe 1950) and the harmonic oscillator model (Levinger 1955)). In view of our recently increased knowledge of the nature of the true nuclear ground-state wave function, which has come hand in hand with a clearer picture of the nature of the two-nucleon potential, it is of interest to repeat these calculations for more realistic  $\Psi_0$ 's. Okamoto (1959) has gone one step in this direction by using a wave function from first order Rayleigh-Schrödinger perturbation theory (with plane-wave single-particle basis functions) in an attempt to take account of dynamical correlations due to the nuclear forces. Naturally, it was impossible to include a strong repulsion in the assumed neutron-proton interaction; his  $w$  was an entirely attractive central one of Gaussian shape with parameters taken from Blatt and Jackson (1949). However, the high-energy scattering data requires the presence of a repulsive core in the two-nucleon interaction, of radius roughly 0.5 fermi. Furthermore, the work of Brueckner and Gammel (1958), of Iwamoto and Yamada (1957), and of Gomes, Walecka, and Weisskopf (1958) indicates that this strong short-range repulsion has a profound correlating effect on the nuclear wave function, an effect, though, which extends only over distances rather short compared to the range of the attraction. The attractive part of the potential produces "relatively little" further modulation of the independent-particle wave function. This latter conclusion is consistent with the results of Okamoto, who was led to a  $\sigma_{\text{int}}$  only a few per cent larger than the independent-particle model value.

Here we present a simple estimate of the effect of nuclear forces on the integrated photonuclear cross section, for a neutron-proton potential containing a hard core.

#### ASSUMPTIONS AND METHOD OF CALCULATION

We suppose the nuclear ground-state wave function to have the Jastrow structure

$$(6) \quad \Psi_0 = \prod_{i < j=1}^A f(r_{ij}) \Phi_0,$$

where  $\Phi_0$  is a suitable (normalized) independent-particle model wave function and  $f(r_{ij})$  a correlation function characterized by

$$(7) \quad \begin{aligned} f(r_{ij}) &= 0, & r &\leq C, \\ f(r_{ij}) &\rightarrow 1, & r &\gg C, \end{aligned}$$

for a hard core radius  $C$ . This wave function would seem to provide a reasonable approximation to the true wave function for nuclear matter so long as  $f(r_{ij})$  is properly chosen. It should be equally useful in studies of finite nuclei.

Now we consider a large nucleus with  $Z = A/2$  and adopt for  $\Phi_0$  a product of two Slater determinants, one for the neutrons and one for the protons. The single-particle spatial wave functions are taken as plane waves satisfying periodic boundary conditions in a normalization volume  $\Omega$ , all available single-

particle states with momentum less than  $k_F$  (the Fermi momentum) being occupied. Keeping only the first term in the cluster expansion\* of the resulting  $\mathcal{C}$  (the error introduced by the neglect of higher-order cluster contributions will be discussed later), and carrying out the spin sums and angular integrations, we find

$$(8) \quad \mathcal{C}^{(0)} = -\frac{8M}{\hbar^2} \frac{k_F}{\pi} \int_0^\infty f^2(r) \left( \frac{1}{4} w_s(r) + \frac{3}{4} w_t(r) \right) j_1^2(k_F r) r^2 dr,$$

where  $w_s$  is the singlet and  $w_t$  the triplet component of the central part of  $w$ , and  $j_1$  is the spherical Bessel function of first order.

Our calculations of  $\mathcal{C}^{(0)}$  were performed under two different sets of assumptions for the nucleon-nucleon potential and correlation function, corresponding to two different studies of the nuclear matter problem, those of Iwamoto and Yamada (1957) and Brueckner and Gammel (1958). In both cases  $v_{np}$  has the exchange character (3), with  $x = \frac{1}{2}$  (Serber mixture).

#### I. Iwamoto-Yamada (I-Y) Assumptions

The potential appropriate to this case is

$$(9) \quad w_{ij} = w_C(r_{ij}) + S_{ij} w_T(r_{ij}),$$

where  $S_{ij}$  is the tensor operator for nucleons  $i, j$ , and  $w_C$  is spin independent and of exponential form outside a hard core of radius  $C$ :

$$(10) \quad w_C(r) = \begin{cases} \infty, & r \leq C, \\ -Be^{-\beta(r-C)}, & r > C. \end{cases}$$

The parameters in  $w_C$  were chosen to fit the singlet effective range and zero energy scattering length, for a proposed core radius  $C = 0.6$  fermi. Along with this potential, Iwamoto and Yamada assumed a correlation function

$$(11) \quad f(r) = \begin{cases} 0, & r \leq C, \\ 1 - e^{-\mu(r-C)}, & r > C, \end{cases}$$

and determined  $\mu$  variationally by the condition that the "best" wave function of the type considered gives the lowest energy per particle for the nuclear medium;† they quote  $\mu = 5.0$  fermis<sup>-1</sup>. For  $r_0$  we take the equilibrium radius parameter obtained in the Iwamoto-Yamada calculation, namely  $r_0 = 1.1$  fermis, which yields  $k_F = (9\pi)^{1/3}/2r_0 = 1.34$  fermis<sup>-1</sup>.

The corresponding potential for  $C = 0$  is readily obtainable from Blatt and Jackson. Such a potential cannot be used in the nuclear matter problem, of course, since it does not saturate, but it will provide us with a basis for determining the specific effect of the hard core on the integrated cross section.

\*There is now a considerable literature on Jastrow wave functions and the cluster expansions they generate. See, for example, Clark and Feenberg (1959) and references quoted therein, and Hartogh and Tolhoek (1958a, b, c).

†Since the cluster expansion of the expectation value for the energy must be terminated at some cluster order, the extremum property is actually lost, so this procedure is dangerous unless convergence of the cluster expansion for the optimum correlation function (assuming one exists for the order considered) is quite good. For a non-monotonic correlation function which exceeds unity, serious difficulties are encountered if one keeps only the lowest order and tries to minimize. In this connection, see Emery (1958).



## II. Brueckner-Gammel (B-G) Assumptions

Here we adopt the potential used by Brueckner and Gammel in their first extensive nuclear matter calculation, this being the best of a set of phenomenological potentials constructed by Gammel, Christian, and Thaler (1957). B-G put all odd state interactions equal to zero. So again  $w_{ij}$  has the form (9), but now with a spin-dependent  $w_C$ , of Yukawa shape cut off by a core of radius  $C = 0.5$  fermi. The parameter values chosen (including that for  $C$ ) participate in adequate fits of the deuteron properties and the n-p scattering data up to 310 Mev (as well as all the p-p data in this range except the 100-310 Mev polarizations). Following Amado (1958) (who has studied the effects of correlations on nuclear magnetic moments), we take for the correlation function

$$(12) \quad f(r) = \begin{cases} 0, & r \leq C, \\ 1 - (C/r)e^{-\mu'(r-C)}, & r > C, \end{cases}$$

where  $\mu'$  is picked to satisfy

$$(13) \quad \mu' = \sqrt{\frac{2}{5}} k_F.$$

This correlation function is a momentum-independent approximation to the factor multiplying  $\sin kr/kr$  in the relative  $S$ -state wave function, in nuclear matter, of a pair of nucleons of relative momentum  $k$ , calculated in the Brueckner formalism but (1) taking into account only the hard core part of the interaction, (2) representing the Pauli effect by the addition of a mean excitation energy

$$\frac{\hbar^2 \mu'^2}{M} = \frac{\hbar^2 k_F^2}{M} - \frac{3}{5} \frac{\hbar^2 k_F^2}{M}$$

to the energy denominator of the Green's function, and (3) neglecting the dispersive effect of the medium. We choose the nuclear radius parameter  $r_0$  to be 1.0 fermi, in essential agreement with the result of the detailed Brueckner-Gammel calculation. Then  $k_F = 1.52$  fermis<sup>-1</sup> and  $\mu' = 0.96$  fermi.

Here there is no corresponding  $C = 0$  potential, since  $C \neq 0$  is needed to fit the high energy data. But for the sake of comparison with a non-core calculation, we have selected a reasonable  $C = 0$  potential from Table I of Ohmura, Morita, and Yamada (1956) (singlet parameters), in conjunction with Table I of Gammel, Christian, and Thaler (1957) (triplet parameters).

For calculation I it was convenient to let

$$(14) \quad \int_C^\infty = \int_0^\infty - \int_0^C$$

and expand the spherical Bessel function in the integrand in powers of  $k_F r$  for  $r \leq C$ , dropping terms of order  $(k_F r)^2$  and higher (which have negligible effect on the final result). This procedure leads to

$$(15) \quad \begin{aligned} \mathcal{G}^{(0)} = & \frac{8M k_F}{\hbar^2 \pi} B e^{\beta C} \{ I(\beta, k_F) - 2e^{\mu C} I(\beta + \mu, k_F) + e^{2\mu C} I(\beta + 2\mu, k_F) \} \\ & - \frac{1}{9} \frac{8M k_F^3}{\hbar^2 \pi} B e^{\beta C} \{ J(\beta; C) - 2e^{\mu C} J(\beta + \mu; C) + e^{2\mu C} J(\beta + 2\mu; C) \}, \end{aligned}$$



where the integrals involved,

$$(16) \quad \begin{aligned} I(a, k_F) &= \int_0^\infty e^{-ar} j_1(k_F r) r^2 dr, \\ J(a; C) &= \int_0^C e^{-ar} r^4 dr, \end{aligned}$$

are easily evaluated analytically.

For calculation II this method was not advantageous. Instead  $\mathcal{C}^{(0)}$  was written in the exact form ( $\alpha_s = 1/4$ ,  $\alpha_t = 3/4$ )

$$(17) \quad \begin{aligned} \mathcal{C}^{(0)} &= \frac{8M}{\hbar^2} \frac{k_F}{\pi} \sum_{q=s,t} \alpha_q \frac{B_q e^{\beta_q C}}{\beta_q} \{ K_1(\beta_q, k_F; C) - 2C e^{\mu' C} K_0(\beta_q + \mu', k_F; C) \\ &\quad + C^2 e^{2\mu' C} K_{-1}(\beta_q + 2\mu', k_F; C) \}, \\ K_l(a, k_F; C) &= \int_C^\infty e^{-ar} j_l^2(k_F r) r^l dr, \end{aligned}$$

and the required  $K$ 's obtained numerically.

A summary of assumed parameters and results is given in Tables I and II.

TABLE I  
Exchange correction  $\mathcal{C}^{(0)}$  under Iwamoto-Yamada assumptions,  $r_0 = 1.1$  f ( $f = \text{fermi}$ )

$C(f)$	$B$ (Mev)	$\beta(f^{-1})$	$\mu(f^{-1})$	$\mathcal{C}^{(0)}$
0.6	397.3	2.627	5.0	1.5
0.6	397.3	2.627	$\infty$	1.9
0	397.3	2.627	$\infty$	0.43
0	109.5	1.404	$\infty$	0.67

TABLE II  
Exchange correction  $\mathcal{C}^{(0)}$  under Brueckner-Gammel assumptions,  $r_0 = 1.0$  f ( $f = \text{fermi}$ )

$C(f)$	$B_s$ (Mev)	$\beta_s(f^{-1})$	$B_t$ (Mev)	$\beta_t(f^{-1})$	$\mu'(f^{-1})$	$\mathcal{C}^{(0)}$
0.5	905.6	1.7	6395	2.936	.96	3.0
0.5	905.6	1.7	6395	2.936	$\infty$	6.4
0	905.6	1.7	6395	2.936	$\infty$	1.9
0	47.7	0.854	61.7	0.900	$\infty$	0.64

#### DISCUSSION OF RESULTS

The inclusion of a core in the two-nucleon interaction is seen to have a rather striking effect on the exchange correction. One might at first think that the presence of the core would manifest itself in a small decrease in  $\mathcal{C}^{(0)}$ , because for each pair of particles there is forbidden a range of  $r$  values near the origin in which their potential would otherwise be attractive, thus slightly\* suppressing the integral in (5). However, there are two other effects which must be considered:

\*Note that, due to the presence of  $r_{np}^2$ , the region of small  $r_{np} \equiv r$  is de-emphasized in this integral.

(i) The core "pushes" the region of strongest attraction out to a range of  $r$  values that is relatively more important in the integral. This tends to *increase*  $\mathcal{C}^{(0)}$ .

(ii) To maintain a fit of the two-nucleon data, the attraction must be made stronger (tending to *increase*  $\mathcal{C}^{(0)}$ ) and of shorter range (tending to *decrease*  $\mathcal{C}^{(0)}$ ).

Apparently, the battle is won by the factors favoring an increase in  $\mathcal{C}^{(0)}$ . Their relative contributions to this victory may be inferred from the first, third, and fourth sets of entries in the tables.

There is considerable uncertainty in the experimental values for  $\sigma_{\text{int}}$ , largely because one does not know where to set the upper limit on the photon energy scale for the integration of the experimental data: at high energies mesonic effects abound and the Siegert theorem, embodied in (4) and (5), no longer holds. It seems clear, nonetheless, that the values given by the independent-particle model (here represented by the calculations given last in the two tables—those for which  $C = 0$  and the two-nucleon potential parameters *do* fit the low-energy data) are inevitably too low to be consistent with experiment, too low by a factor of roughly  $\frac{3}{2}$  (and at best  $\frac{3}{4}$ ). For  $x = \frac{1}{2}$ , which is the exchange-mixture parameter appropriate to both potentials we have used, the  $\sigma_{\text{int}}$  from calculation I is consistent with experiment, while that from calculation II is a bit high. So it would seem quite possible, by proper choice of potential and parameter values, to achieve the "experimentally pleasing" value of  $\mathcal{C}^{(0)} = 2$ . In this connection the second potential that B-G used, one of the potentials of Gammel and Thaler (1960), which fit all the two-nucleon data up to 310 Mev, looks especially promising. However, this potential has a more general exchange character than (3), so our simple formula (5) does not apply.

We might say a few words about the sensitivity of the calculation to the "choice" of  $r_0$ . Obviously  $\mathcal{C}^{(0)}$  is larger the nearer the maximum of  $k_F j_1^2(k_F r)$  is to the peak of  $-fw_C r^2$ . Since  $-fw_C r^2$  definitely has a relative maximum, we suspect that there will be a range of  $r_0$  values ( $0 \leq r_0 < r_{0m}$ , say) in which  $\mathcal{C}^{(0)}$  increases with  $r_0$ , followed by a range ( $r_{0m} < r_0 < \infty$ ) in which  $\mathcal{C}^{(0)}$  decreases with  $r_0$ . Both our calculations would then lie in the latter region. Be that as it may, the variation of  $\mathcal{C}^{(0)}$  with  $r_0$  is not expected to be particularly rapid over the physically relevant range.

On the other hand, the sensitivity of our calculations to the correlation function parameter ( $\mu$  or  $\mu'$ , as the case may be) is quite marked. By virtue of this sensitivity there arises the possibility, for a given two-nucleon potential, of setting an (admittedly weak) restriction on the behavior of the two-nucleon correlation function.

We must still discuss the error introduced by neglecting the higher-order cluster corrections to  $\mathcal{C}^{(0)}$ . It is known from the work of Iwamoto and Yamada (1957) and Dabrowski (1958a, b) that these corrections are of order  $(A\omega/\Omega)\mathcal{C}^{(0)}$ , where  $\omega = \int (f^2(r) - 1)\phi^2(r)dr$ ,  $\phi$  being the  $S$ -state relative wave function of a pair of particles of the model. We conclude then that the deviation of  $\mathcal{C}^{(0)}$  from  $\mathcal{C}$  for calculation I (based on I-Y parameters) should be well within

experimental errors, since for this case the convergence parameter  $A\omega/\Omega$  is of the order of  $1/9$ . This cannot be asserted for calculation II (based on the B-G parameters), however, because the correlation function in this case has a rather long range, so that there may be sizable corrections from the higher-order cluster terms. But we believe a shorter range (short enough so that the higher-order cluster terms are not troublesome) to be more appropriate than the one we used. In the first place, the inclusion of the attractive part of the interaction will certainly shorten the range of a monotonic correlation function like (12), since the probability of two particles being close together is increased. (This effect should be quite important, since in this case the attractive well is very deep and of very short range.) Secondly, if we treat the dispersive effect of the medium in the same fashion as the Pauli effect, that is, by adding a constant energy of excitation  $\hbar^2\gamma^2/M$  in the energy denominator of the Green's function for the two-body motion, then the form of the correlation function is unchanged from (12) but the range is again shortened. (A crude estimate based on the work of Moszkowski and Scott (1960) gives  $\gamma^2 \approx 0.33 k_F^2$ , and hence  $\sqrt{(\mu'^2 + \gamma^2)} \approx 1.3 \text{ fermi}^{-1}$  for the inverse range with dispersion, as compared to  $\mu' = 0.96 \text{ fermi}^{-1}$  without.) Thus the inclusion of both originally neglected effects shortens the range of the correlation function, if we are restricted to the form (12). More generally, we expect a smaller  $A\omega/\Omega$  than would be given by the correlation function of calculation II. This conjecture is substantiated by Fig. 5 in the Brueckner-Gammel paper, showing the quantitative behavior of the *S*-state wave function in nuclear matter, computed without resort to the approximations (1), (2), (3).

If, as suggested above, a considerably shorter range were used for the correlation function in calculation II, the resulting estimate for  $\mathcal{C}^{(0)}$  would be even larger than that in Table II. And since the higher cluster corrections should then be small, we would be led to the conclusion that the central part of the Gammel-Christian-Thaler potential considered does not by itself allow an understanding of the photonuclear data. Such a conclusion is not particularly hard to accept—one has the feeling that this potential is much too singular—but only a detailed calculation would be truly convincing. For one thing, we have used an *S*-state correlation function for all relative angular momentum states, which somewhat overestimates the effects of correlation. In fact, to be consistent, we should actually take a suitable state-independent average correlation function from a careful analysis of Brueckner and Gammel's detailed, quantitative results (as a function of relative momentum and relative angular momentum) for the two-nucleon wave function in nuclear matter. Such a correlation function would clearly be non-monotonic, and hence would lead us out of the family of functions (12). To keep within the calculational framework of the present paper, one could alternatively perform a variational type of calculation (as in the I-Y case) for the potential in question, assuming a correlation function of the style (12).

A set of calculations with the Gammel-Thaler potential mentioned earlier (which has a much less singular central component than the Gammel-Christian-Thaler potential, but contains a strong spin-orbit term) for a range of

$r_0$  values, and for realistic, non-monotonic correlation functions, should be very enlightening, and will be considered in a later paper, together with an explicit examination of the terms of first order in  $A\omega/\Omega$ .

It may be profitable to carry out a similar reanalysis of some of the other moments of the photonuclear cross section.

#### ACKNOWLEDGMENTS

I wish to acknowledge financial support from Washington University, where a portion of this work was done, and from the National Science Foundation. I am indebted to Professor E. Feenberg and Professor J. S. Levinger for their advice and encouragement.

#### REFERENCES

- AMADO, R. D. 1958. *Phys. Rev.* **111**, 548.  
BLATT, J. M. and JACKSON, J. D. 1949. *Phys. Rev.* **76**, 18.  
BRUECKNER, K. A. and GAMMEL, J. L. 1958. *Phys. Rev.* **109**, 1023.  
CLARK, J. W. and FEENBERG, E. 1959. *Phys. Rev.* **113**, 388.  
DABROWSKI, J. 1958a. *Proc. Phys. Soc. (London)* **A, 71**, 658.  
——— 1958b. *Proc. Phys. Soc. (London)* **A, 72**, 499.  
EMERY, V. J. 1958. *Nuclear Phys.* **6**, 585.  
GAMMEL, J. L., CHRISTIAN, R. S., and THALER, R. M. 1957. *Phys. Rev.* **105**, 311.  
GAMMEL, J. L. and THALER, R. M. 1960. *Progress in cosmic ray physics*, Vol. V, edited by J. G. Wilson and S. A. Wouthuysen (North Holland Publishing Company, Amsterdam), Chap. II.  
GOMES, L. C., WALECKA, J. D., and WEISSKOPF, V. F. 1958. *Ann. Phys.* **3**, 241.  
HARTOGH, C. D. and TOLHOEK, H. A. 1958a. *Physica*, **24**, 721.  
——— 1958b. *Physica*, **24**, 875.  
——— 1958c. *Physica*, **24**, 896.  
IWAMOTO, F. and YAMADA, M. 1957. *Progr. Theoret. Phys. (Japan)* **18**, 345.  
LEVINGER, J. S. 1955. *Phys. Rev.* **97**, 122.  
LEVINGER, J. S. and BETHE, H. A. 1950. *Phys. Rev.* **78**, 115.  
MOSZKOWSKI, S. A. and SCOTT, B. L. 1960. *Ann. Phys.* **11**, 65.  
OHMURA, T., MORITA, M., and YAMADA, M. 1956. *Progr. Theoret. Phys. (Japan)* **15**, 222.  
OKAMOTO, K. 1959. *Phys. Rev.* **116**, 428.

# INTERFÉROMÈTRE MICRO-ONDE À FOND COHÉRENT<sup>1,2</sup>

A. BOIVIN ET R. TREMBLAY<sup>3</sup>

## RÉSUMÉ

Dans cet article, nous décrivons un nouveau type d'interféromètre micro-onde à propagation libre du signal de référence. Cet appareil est destiné à l'étude de la distribution de l'amplitude dans le champ diffracté associé à un système optique micro-onde parfait ou aberrant. La méthode de mesure est basée sur le principe de l'observation de phase en présence d'un fond cohérent. La mise en oeuvre de ce principe fait appel à la fois à une polarisation appropriée des sources, et aux propriétés remarquables de l'antenne tourniquet utilisée comme détecteur. Deux balayages successifs du champ diffracté permettent de déterminer la distribution de l'amplitude complexe, et cela sous la forme cartésienne, partie réelle et partie imaginaire.

À l'aide de l'interféromètre à fond cohérent, réalisé dans ce laboratoire, nous avons étudié la distribution de l'amplitude diffractée dans différents plans de l'espace image d'un système micro-onde parfait. Ces résultats, qui présentent une correspondance remarquable avec les résultats théoriques, ont permis d'évaluer les caractéristiques et les possibilités de cette méthode interférométrique.

Alliant d'une manière heureuse des techniques empruntées aux domaines des hyperfréquences et de l'optique du visible, ce procédé interférométrique facilitera l'étude des phénomènes de la diffraction au domaine des ondes millimétriques.

## 1. INTRODUCTION

L'étude de la distribution d'intensité dans l'espace image d'un système optique ne fournit qu'une information bien incomplète. À celle-ci, il convient d'ajouter la mesure de la distribution de phase de sorte que l'état vibratoire, en tout point du champ diffracté, soit complètement déterminé.

### 1.1 Mesure d'une vibration électromagnétique

L'expression d'une vibration en un point  $P$  d'un champ diffractionnel est une fonction sinusoïdale du temps que l'on peut écrire, utilisant la notation imaginaire

$$(1) \quad U_P = A_P e^{i(\omega t - \varphi_P)},$$

où  $A_P$  est le module de l'amplitude complexe,  $\omega$  la pulsation et  $\varphi_P$  la phase de la vibration en  $P$ . La mesure d'une vibration impose donc, d'après l'équation (1), la détermination de  $A_P$  et  $\varphi_P$ . De plus, il faut remarquer que la mesure ne peut être statique. Les termes exponentiels en  $i\omega t$  et  $i\varphi_P$  exigent que l'unité de mesure soit elle-même une vibration dite de référence. La vibration  $U_P$  et celle de référence  $U_r$  doivent avoir la même période d'oscillation et leurs phases liées. De plus, elles doivent être parallèles. La vibration de référence peut donc s'écrire:

$$(2) \quad U_r = A_r e^{i(\omega t - \varphi_r)}.$$

La comparaison entre l'inconnue et l'unité de mesure a lieu par interférence.

<sup>1</sup>Manuscrit reçu le 4 novembre, 1960.

<sup>2</sup>Contribution du Centre de Recherches en Physique de l'Université Laval, Québec, Qué.

<sup>3</sup>Ce mémoire constitue une partie de la thèse qui sera présentée par R. Tremblay en vue de l'obtention du Doctorat en Sciences physiques à l'Université Laval.

<sup>4</sup>Bénéficiaire d'une bourse d'études du Conseil National des Recherches.

En conséquence, un appareil susceptible de déterminer la distribution en amplitude, module et phase, d'un champ diffracté est nécessairement un type quelconque d'interféromètre.

### 1.2 Interféromètres micro-ondes

Les techniques micro-ondes ont déjà permis la réalisation de nombreux types d'interféromètres qui se distinguent de leurs prédécesseurs optiques sous bien des aspects (Pavlassek 1958; Tremblay 1960). On peut décrire brièvement le système fondamental de mesure interférométrique en micro-onde de la façon suivante: le signal émis d'un klystron est divisé par une jonction hybride (*T* magique) en deux ondes, dont l'une excite la source ponctuelle qui illumine l'ouverture diffringente et l'autre, qui servira de référence, se propage jusqu'au système de détection. D'autre part, une sonde explore le champ diffracté et transmet au système de détection une onde proportionnelle à la vibration échantillonnée, cette onde interférant avec l'onde dite de référence. De plus, mentionnons l'emploi d'un circuit auxiliaire pour la détermination de la fréquence des vibrations émises par le klystron, comme aussi la présence d'atténuateurs et de déphaseurs de précision pour modifier les relations de phase et d'amplitude entre les deux ondes. Par ailleurs, il faut remarquer dans ces interféromètres la présence de bras de guide, articulés par des joints rotatifs. Ces tronçons de ligne établissent un lien guidé mobile entre le circuit de détection et la sonde, permettant à cette dernière les déplacements nécessaires à l'exploration de tout l'espace image.

On peut grouper les interféromètres micro-ondes en quatre catégories.

#### *Interféromètres à détection par interférence directe*

(a) *Interférence simple* (Blair 1958; Redheffer et Winkler 1945; Froome 1952, 1954; Ajioka 1955; Lenyel 1949).—Dans ce procédé, on additionne à l'aide d'un *T* magique les deux vibrations  $U_p$  et  $U_r$ . La vibration résultante induit aux bornes d'un détecteur à cristal un voltage qui, amplifié par un amplificateur audio accordé à la fréquence de modulation, prend la forme suivante:

$$(3) \quad e_0 = C_1[A_p^2 + A_r^2 + 2A_p A_r \cos(\varphi_p - \varphi_r)].$$

On explicite l'information désirée, le module et la phase de la vibration  $U_p$ , en annulant le signal résultant à l'aide d'un déphaseur et d'un atténuateur. L'équation (3) implique alors les deux relations suivantes:

$$(4) \quad \begin{cases} A_p = A_r \\ \varphi_p = \varphi_r \pm (2K+1)\pi \end{cases} \quad (K = 0, 1, 2, 3 \dots).$$

Ainsi, relativement à la référence, on peut déterminer le module et la phase de l'amplitude complexe en tout point de l'espace image. Ce procédé exige une mesure point par point et ne peut être automatisé.

(b) *Interférence composée* (Richmond 1955; Bacon 1954).—Dans ce système de mesure on fait subir simultanément aux ondes  $U_r$  et  $U_p$  une double interférence dans un *T* magique. L'une est constructive,  $U_+ = U_r + U_p$ , l'autre destructive,  $U_- = U_r - U_p$ . Les vibrations résultantes,  $U_+$  et  $U_-$ , sont propagées séparément dans deux des branches du *T* magique jusqu'aux détecteurs

qui terminent ces tronçons de ligne. La différence entre les voltages  $e_+$  et  $e_-$ , obtenue à l'aide d'un transformateur audio balancé, donne:

$$(5) \quad e_0 = e_+ - e_- = 4A_p A_r \cos(\varphi_r - \varphi_p).$$

Pour un signal de référence dont le module et la phase sont constants, le signal résultant devient donc directement proportionnel à la partie réelle de  $U_p$ ,  $\text{Re}[U_p]$ . Subséquemment, un déphasage de  $\pi/2$  du signal de référence permet d'obtenir par le même procédé la partie imaginaire de l'amplitude complexe,  $\text{I}[U_p]$ .

*Interféromètres à détection sur une fréquence intermédiaire* (Barrett et Barnes 1952; Brooks 1951)

Dans cette catégorie d'interféromètres, les signaux  $U_p$  et  $U_r$  subissent, par l'emploi d'un oscillateur local et de mélangeurs de fréquences, une translation au domaine des fréquences intermédiaires (I.F.). La relation initiale de phase entre les signaux micro-ondes demeure inchangée lors de cette transposition et la mesure de phase devient beaucoup plus aisée à ce domaine de fréquences. Toutefois, ce procédé présente des inconvénients graves. Pour conserver la relation initiale de phase, les caractéristiques des récepteurs doivent être identiques et les variations de fréquence du klystron transmetteur et du klystron employé comme oscillateur local doivent être très faibles. Toutes ces exigences rendent instables les appareils de mesure basés sur ce procédé de détection.

*Interféromètres basés sur la modulation de l'un des signaux*

Les interféromètres groupés dans cette catégorie transposent la mesure de la phase micro-onde à une fréquence audio, en modulant l'une des vibrations selon une technique appropriée. La modulation de phase a été employée par Lavrench (1955) et Worthington (1947). D'autres auteurs ont utilisé un signal de référence, soit S.S.B. (Mariner 1953), soit à onde latérale plus l'onde porteuse (Mittra 1957) ou à ondes latérales (Vernon 1952; Pavlasek 1958).

Bien que fondamentalement dans ces procédés la mesure de phase s'obtienne par interférence directe, la modification de la nature de l'une des vibrations interférentes amène un signal résultant fort différent de celui présenté par l'équation (3). La mesure de la phase devient indépendante de l'amplitude relative des vibrations  $U_p$  et  $U_r$ , de sorte que ces appareils se prêtent facilement à l'automatisation.

*Interféromètres à propagation libre du signal de référence*

Il existe quelques interféromètres micro-ondes qui reproduisent assez fidèlement les techniques de mesures de l'interférométrie optique. Dans ces appareils, intentionnellement, on se préoccupe peu de tirer profit de tous les avantages offerts par les techniques micro-ondes. Mentionnons dans cette catégorie les interféromètres du type Michelson, réalisés par Hull (1952) pour fins de démonstration et par Culshaw (1950) pour la détermination précise d'une longueur d'onde, comme aussi l'interféromètre micro-onde du type Fabry-Pérot construit par Culshaw (1953).

Il est un point important qu'il convient de souligner ici. A notre connaissance, deux auteurs seulement (Harden 1952; Ajioka 1955) ont utilisé avant nous l'interférométrie micro-onde à propagation libre de la référence pour



l'étude des champs diffractés. Toutefois, il s'agit là d'une application partielle de ce principe, puisqu'on y compare les états vibratoires en deux points différents du champ diffracté.

### 1.3 Caractéristiques d'un appareil pour la mesure de la phase

Dans la réalisation d'un appareil de mesure, on doit appliquer les principes et les procédés qui conduisent au système le plus simple, sans sacrifier par ce choix la caractéristique principale, la précision. L'étude des différents types d'interféromètres micro-ondes précédemment décrits nous incite à choisir, comme étant la plus simple, la technique de mesure à détection par interférence directe et composée. De plus, le choix de ce procédé de mesure permet d'automatiser facilement le système. L'automatisme n'est pas une caractéristique à dédaigner, bien qu'elle diminue quelque peu la précision des mesures.

Quant à la caractéristique essentielle d'un système de mesure, la précision, elle doit porter dans le cas présent sur les deux termes suivants: le module  $A_p$  et la phase  $\varphi_p$  de la vibration électromagnétique  $U_p$ . Les erreurs qui affectent la mesure de ces quantités proviennent du déphaseur, des réflexions parasites et des joints rotatifs. Celles qui proviennent du déphaseur et des réflexions parasites peuvent être facilement minimisées. Quant à la présence de composantes électrodynamiques (joints rotatifs) dans le système de mesure, l'étude de résultats expérimentaux montre qu'elle devient au domaine des ondes centimétriques une cause d'erreur très importante. Ce résultat sera encore plus marqué au domaine des ondes millimétriques.

Pour obtenir une précision convenable ( $\pm 2^\circ$ ) sur la détermination de la phase au domaine des fréquences  $> 24$  kMc/sec, il se présente alors deux solutions: la première consisterait à améliorer les caractéristiques des joints rotatifs; la seconde, à les éliminer du système de mesure. Les possibilités de succès suivant la première voie nous ont parues reposer sur trop de facteurs aléatoires. Par contre, l'application de la seconde méthode nous a amenés à reconsidérer les techniques optiques. Ainsi, cette étude nous a conduits à la réalisation d'un nouveau type d'interféromètre micro-onde à propagation libre du signal de référence.

## 2. INTERFÉROMÈTRE MICRO-ONDE À FOND COHÉRENT

### 2.1. Diffraction en présence d'un fond cohérent

La distribution du signal de référence dans l'espace image doit être facilement réalisable et représentée par une expression mathématique simple. En conséquence, le champ électromagnétique émis d'une source ponctuelle semble tout indiqué. Dans ce cas, l'amplitude complexe en un point  $P$ , situé à une distance  $R$  de la source s'écrit:

$$(6) \quad U_p = U_0 (e^{-ikR}/R),$$

où  $U_0$  est l'amplitude de la vibration émise à la source et  $k = 2\pi/\lambda$  sa constante de propagation. Toutefois, la distribution représentée par l'équation (6) ne semble pas remplir les conditions propres à un standard de mesure puisqu'elle n'est pas uniforme en module et en phase dans un plan d'observation quelconque. À la section suivante on établira hors de tout doute que cette remarque



n'est pas justifiée, en montrant que le front d'onde sphérique convient mieux à la mesure des figures de diffraction en amplitude que le front d'onde plan.

Mentionnons de plus que la distribution de fronts d'onde sphériques est facilement réalisable à l'aide d'une source ponctuelle (guide ouvert).

En optique, ce procédé interférométrique est utilisé pour observer des variations de phase sous le nom de diffraction en présence d'un fond cohérent (Zernike 1934; Flügge 1956). Mentionnons que Nienhuis (1948), en employant cette méthode, observa le phénomène de l'inversion de phase aux zéros de la figure de diffraction associée à un système optique dans le visible.

## 2.2. Systèmes conventionnels et procédé interférométrique à fond cohérent

Considérons l'intégrale de diffraction qui exprime l'amplitude de la vibration excitée en un point  $P$  de l'espace image. Selon la notation courante en optique, la position de ce point  $P$  sera indiquée par les valeurs de deux paramètres "y" et "z", le premier caractérisant le plan hors de foyer étudié et le second désignant le cercle de ce plan sur lequel est situé  $P$ . En tant que déphasage ces deux paramètres sont des nombres purs (Boivin 1960). Dans le cas de non révolution, il faut de plus spécifier l'angle  $\psi$  du plan méridien contenant  $P$ . Dans ces conditions l'amplitude diffractée a pour expression

$$(7) \quad U(y, z, \psi) = \text{Cte} \frac{e^{-ikR}}{R} \int_0^1 \int_0^{2\pi} u(r, \phi) e^{ik[g(y, z, \psi, r, \phi) + V(r, \phi)]} r dr d\phi,$$

où le point  $M(r, \phi)$  explore la pupille,  $u(r, \phi)$  représente le module de la vibration au point  $M$  et  $V(r, \phi)$  la phase. De plus, la fonction  $g(y, z, \psi, r, \phi)$  détermine le chemin optique propre à la position géométrique de  $M$  et  $P$ , et  $R$  la distance entre le point  $P$  et le centre de l'ouverture diffringente. La solution de l'équation (7) peut s'écrire sous la forme polaire:

$$(8) \quad U(y, z, \psi) = \text{Cte} \frac{e^{-i(kR + \varphi_I)}}{R} h_I(y, z, \psi),$$

où  $h_I(y, z, \psi)$  représente le module de la vibration résultant de l'intégrale de l'équation (7) et  $\varphi_I$  la phase de cette même vibration. Quant à la phase de la vibration  $U(y, z, \psi)$ , elle provient de la somme de deux termes; le premier,  $kR$ , représente la phase au point  $P$  d'une onde sphérique émise du centre de la pupille de sortie; le second,  $\varphi_I$ , provient de la contribution de l'intégrale.

À ce point, il convient de faire une remarque importante à propos des systèmes conventionnels. D'une part, dans ces appareils, le signal de référence est constant, en module et phase, quelle que soit la position de la sonde. En conséquence, la phase détectée à l'aide de ces interféromètres peut s'écrire:

$$(9) \quad \delta = \frac{2\pi}{\lambda} R + \varphi_I,$$

où  $2\pi R/\lambda$  représente le terme de phase sphérique et  $\varphi_I$ , la contribution de l'intégrale.

D'autre part, dans un phénomène diffractif, pour un déplacement  $\Delta R$ , la variation de phase due au terme sphérique est beaucoup plus importante que celle qui provient de l'intégrale. Par exemple, dans l'étude de la diffraction

le long de l'axe d'un système micro-onde parfait de révolution et d'ouverture numérique  $f/5$  ( $f = 100$  po.),  $\Delta\varphi_I = (1/400)(2\pi/\lambda)\Delta R$  tandis que la contribution du front d'onde sphérique varie comme  $(2\pi/\lambda)\Delta R$ . Conséquemment, toute erreur sur la détermination de  $R$ , distance entre le centre de phase de la sonde et le centre de l'ouverture diffringente, masque  $\varphi_I$  ou l'entache d'une erreur importante. Aussi, à la fréquence d'opération 24 kMc/sec, pour une mesure de phase précise à  $\pm 2^\circ$ , il nous faut déterminer  $R$  à  $\pm 0.003$  po., et au domaine millimétrique (72 kMc/sec), cette exigence atteindra  $\pm 0.001$  po.

Mentionnons de plus que les études sur la diffraction portent, en général, sur l'intégrale. Elles négligent donc le terme en  $e^{-ikR}$ , et les résultats qu'elles donnent ne contiennent que la contribution due à l'intégrale. En conséquence, les mesures obtenues jusqu'ici avec les interféromètres micro-ondes conventionnels et représentées par l'équation (9) se comparent difficilement aux résultats théoriques.

Voici pourquoi l'emploi d'un front d'onde sphérique émis du centre de la pupille convient parfaitement bien comme référence: il élimine du processus de mesure le terme en  $e^{-ikR}$ , et ne laisse que la contribution de l'intégrale de diffraction ( $\varphi_I$ ), de sorte que les inconvénients mentionnés ci-dessus n'existent plus.

A cette caractéristique du procédé de mesure en présence d'un fond cohérent, il faut ajouter les suivantes: une meilleure précision dans les mesures due à l'élimination des joints rotatifs, une grande simplicité de réalisation et, de plus, l'absence de difficulté d'isolation entre les circuits de détection et d'alimentation.

### 2.3. Interféromètre micro-onde à fond cohérent réalisé dans ce laboratoire

#### *Description de l'appareil*

Le montage est le suivant (figure 1): un guide ouvert (source ponctuelle  $C_1$ ) excite une ouverture  $\Sigma$ , qui, en un plan  $x'O'y'$ , produit une figure de diffraction  $U_\Sigma$ . La distribution angulaire de cette figure est fonction de la nature de l'ouverture et de ses dimensions. Mentionnons qu'au domaine des ondes centimétriques et millimétriques, les systèmes étudiés sont diaphragmés par des ouvertures dont les dimensions sont  $\geq 30\lambda$ , de sorte que l'étalement de la figure de diffraction demeure faible.

Au centre de l'ouverture  $\Sigma$ , on place une seconde source ponctuelle  $C_2$ , laquelle est alimentée par le même générateur d'ondes qui excite la source primaire  $C_1$ . Cette seconde source, dite de référence, distribue des fronts d'ondes sphériques dans tout l'espace image. Au plan  $x'O'y'$  tout se passe comme si on superposait à la figure de diffraction  $U_\Sigma$  un front d'onde sphérique et cohérent. Ainsi, le signal de référence se trouve distribué dans tout l'espace image et, en conséquence, il n'est plus nécessaire d'établir un lien guidé entre les circuits de détection et d'alimentation.

### 2.4. Description du circuit et des composantes micro-ondes

#### *(i) Circuit micro-onde*

Le champ électromagnétique, excité dans un premier tronçon de guide par un klystron opérant à la fréquence  $\nu = 24$  kMc/sec, est divisé en deux ondes

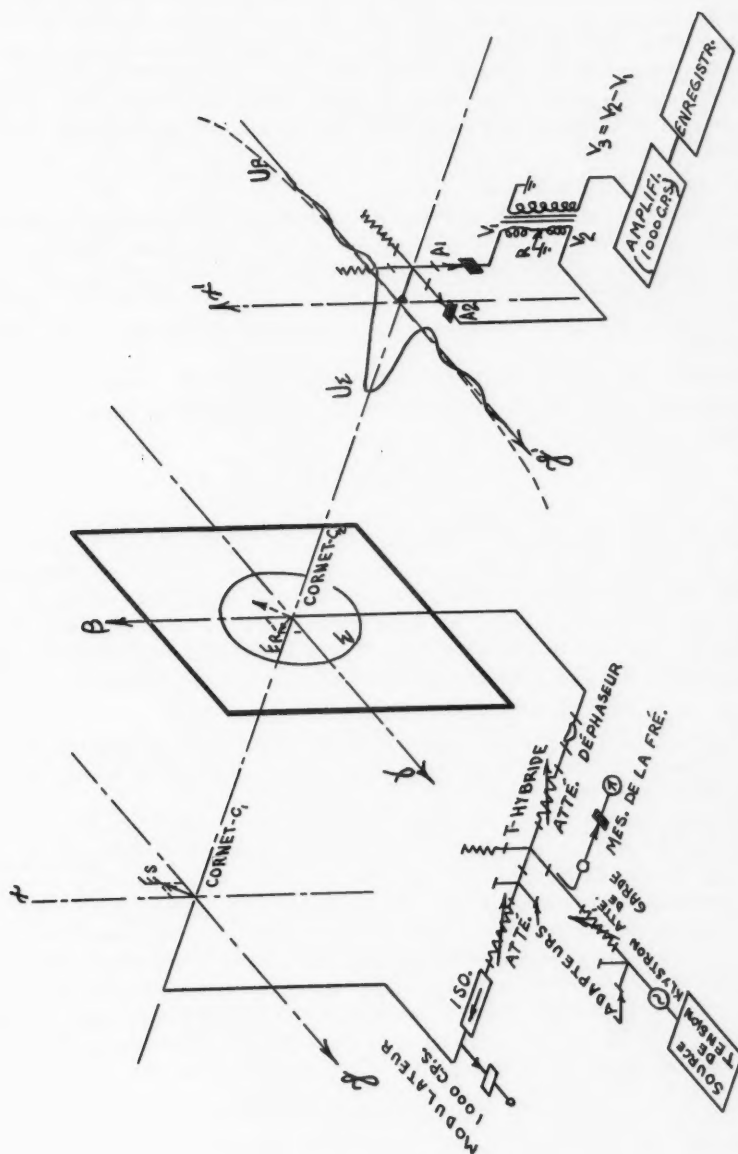


Fig. 1. Interféromètre à fond cohérent pour l'étude de la figure de diffraction associée à un système micro-onde.

par un  $T$  magique. Ces dernières sont propagées dans deux autres tronçons de guide jusqu'aux cornets sources. Par ailleurs, l'insertion dans un de ces tronçons de guide d'un déphaseur et d'un atténuateur permet d'établir toute relation de phase et d'amplitude désirée entre ces deux ondes. Mentionnons aussi la présence d'un circuit guidé auxiliaire pour la détermination de la fréquence d'opération et de composantes pour l'adaptation et l'isolation (voir figure 1).

(ii) *Déphaseur de précision*

Un nouveau type de déphaseur variable qui permet de déterminer la phase d'une vibration à  $\pm 1/2^\circ$  a été mis au point dans ce laboratoire. Toutefois, la construction du modèle expérimental n'était pas terminée lors de la mise au point de cet interféromètre. Nous avons alors utilisé un procédé fort simple pour modifier la relation de phase entre les ondes émises par les sources ponctuelles.

Un déplacement  $\Delta R$  de l'une des sources suivant l'axe du faisceau diffracté introduit une différence de marche entre les deux fronts d'onde et de là un déphasage qui peut s'écrire:

$$(10) \quad \varphi = (2\pi/\lambda)\Delta R.$$

En conséquence, un déplacement total de  $\lambda/2$  suffit à établir toutes les relations de phase nécessaires à l'étude de la distribution de l'amplitude complexe dans un champ diffracté. Toutefois, il faut remarquer que ce procédé de déphasage modifie légèrement la courbure du front d'onde sphérique déplacé longitudinalement. Cette erreur s'identifie à un léger défaut de mise au point qui affecte la mesure de  $1.1^\circ$  au maximum. Il sera donc préférable d'employer le déphaseur variable à prismes diélectriques lorsqu'il sera disponible.

(iii) *Système de détection*

Le système de détection contribue pour une bonne part à l'originalité de cette méthode interférométrique et sa mise au point a constitué la principale difficulté de cette réalisation.

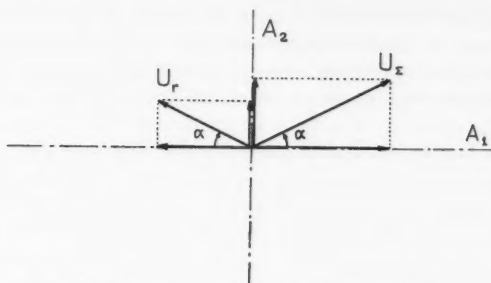
Dans ce procédé de mesure, la sonde qui explore la figure de diffraction reçoit, en tout point  $P$  de l'espace image, un signal résultant de la composition de deux vibrations. Si elles sont parallèles et si l'on utilise un guide ouvert comme sonde, le signal détecté sera représenté par l'équation (3).

D'un point de vue différent, considérons maintenant un guide ouvert comme étant un analyseur sensible à la polarisation. Modifions par ailleurs la polarisation des sources, de sorte que les champs issus de la source primaire et de la source de référence soient polarisés linéairement et fassent respectivement des angles  $\alpha$  et  $(180^\circ - \alpha)$  par rapport à la direction privilégiée de l'analyseur  $A_1$  (figure 2). Le signal détecté par l'analyseur  $A_1$  peut s'écrire:

$$(11) \quad e_1 = C_1 |U_{A_1}|^2 = C_1 \cos^2 \alpha |U_z - U_r|^2,$$

où  $C_1$  est une constante qui tient compte de la réponse de l'analyseur et du cristal détecteur. Plaçons maintenant à ce même point  $P$  un autre analyseur,  $A_2$ , perpendiculaire au premier. On peut donc écrire:

$$(12) \quad e_2 = C_2 \sin^2 \alpha |U_z + U_r|^2.$$

FIG. 2. Composantes des vibrations  $U_r$  et  $U_z$  suivant deux axes perpendiculaires.

Pour une valeur de  $\alpha$  telle que

$$(13) \quad C_1 \cos^2 \alpha = C_2 \sin^2 \alpha = C,$$

nous obtenons les résultats suivants:

$$(14) \quad \begin{aligned} e_1 &= C|U_z - U_r|^2 \\ e_2 &= C|U_z + U_r|^2. \end{aligned}$$

À ce point nous sommes ramenés à la théorie de l'interférence directe et composée.

Dans les expressions (5) et (14) posons arbitrairement  $\varphi_r = 0$ . Si  $U_z(\sigma)$  représente le signal en un point situé à une distance  $\sigma$  de l'axe dans la figure de diffraction  $U_z$  associée à une ouverture circulaire, la différence entre  $e_1$  et  $e_2$ , obtenue à l'aide d'un transformateur audio balancé, donne alors:

$$(15) \quad e_0 = 4CA_r A(\sigma) \cos[\varphi(\sigma)].$$

Ce résultat est donc directement proportionnel à la partie réelle de l'amplitude complexe  $U_z(\sigma)$ . Par ailleurs, un déphasage de  $\pi/2$  du signal de référence donne la partie imaginaire de cette vibration.

Quant à la sonde, notre choix a porté sur l'antenne tourniquet (Ragan 1947; Allen 1956; Meyer et Goldberg 1955). Cette antenne (figure 3) consiste en

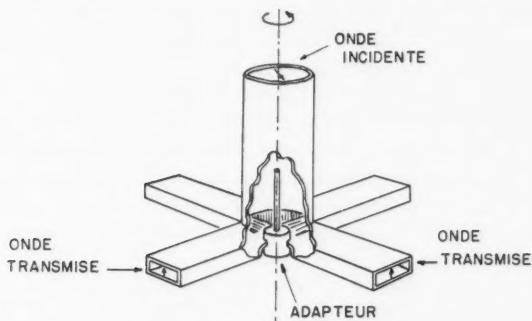


FIG. 3. Antenne tourniquet.

deux bras de guide rectangulaire, placés en croix, leur partie commune supportant une section de guide circulaire montée perpendiculairement et dirigée suivant l'axe du faisceau diffracté. Dans ces conditions, le guide circulaire est utilisé comme sonde et l'antenne peut tourner autour du tronçon circulaire, de sorte que les bras agissent deux à deux tout comme des analyseurs croisés. La figure 4 présente le diagramme de la polarisation des champs et de la décompo-

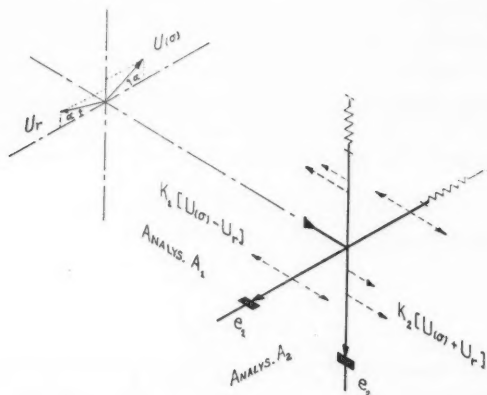


FIG. 4. Polarisation des champs et décomposition des vibrations dans l'antenne tourniquet.

sition des vibrations dans l'antenne tourniquet. Ce système réalise physiquement la méthode de détection par interférence directe et composée. Mentionnons aussi comme partie intégrante du système de détection la modulation en onde carrée variant à un taux audio (1000 c/sec) de l'amplitude de l'une ou des deux ondes émises par les sources. Cette modulation permet d'augmenter la sensibilité du système.

### 2.5. Orientation initiale de la polarisation des champs

Pour l'ajustement du système de détection, deux des composantes suivantes, les sources et la sonde, doivent permettre une rotation de leur direction de polarisation dans un plan perpendiculaire à l'axe du faisceau diffracté. Dans le cas présent, la source primaire et la sonde offrent cette possibilité.

Tout d'abord, on met le klystron en opération et ensuite on procède de la façon suivante: une première étape consiste à éteindre à l'aide d'atténuateurs, la source qui illumine le système micro-onde étudié de sorte que les vibrations qui se propagent dans l'espace image proviennent de la seule source de référence. On tourne alors la sonde jusqu'à ce que le voltage induit aux bornes du transformateur audio, préalablement balancé, soit nul. A ce stage, la relation (13) est vérifiée pour la décomposition de la vibration de référence, suivant les bras de l'antenne tourniquet.

A la seconde étape, on éteint cette fois la source de référence et on tourne la direction de polarisation de la source primaire jusqu'à ce que le signal

déecté soit nul. De nouveau, la relation (13) est vérifiée, cette fois pour l'analyse du champ diffracté dans l'espace image.

Ces ajustements faits, l'interféromètre est au point et prêt à mesurer la distribution de l'amplitude complexe dans un champ diffracté.

### 3. RÉSULTATS OBTENUS

Pour déterminer les caractéristiques expérimentales de ce procédé interférométrique, nous avons étudié à l'aide de l'appareil réalisé dans ce laboratoire la distribution de l'amplitude diffractée dans différents plans de l'espace image d'un système optique micro-onde dénué d'aberration.

Ce dernier est constitué de la façon suivante: un objectif aplanétique de très bonne qualité et diaphragmé par une ouverture circulaire transforme en un front d'onde plan le front d'onde sphérique émis par une source ponctuelle (guide ouvert) placée à son foyer. Ensuite, de manière à obtenir l'image de la source ponctuelle, une seconde lentille, aplanétique et identique à la première, reconstitue le front d'onde sphérique et forme ainsi l'image géométrique de la source.

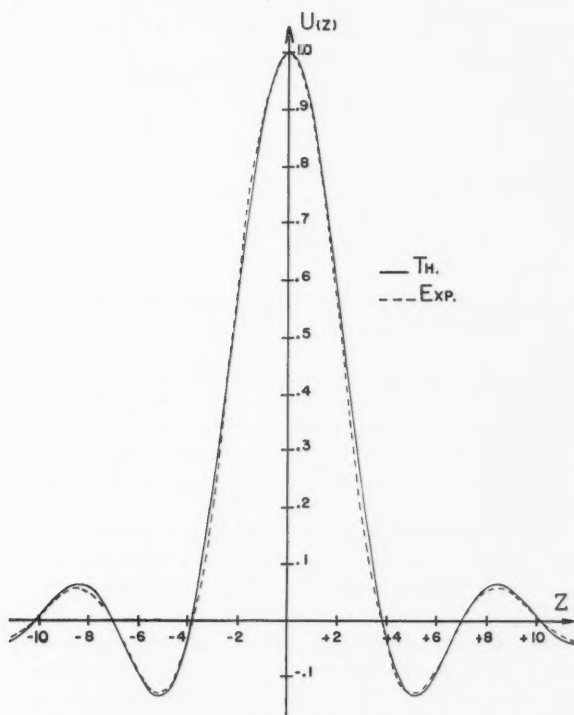


FIG. 5. Distribution de l'amplitude diffractée au plan focal d'un système micro-onde parfait (ouverture circulaire;  $\lambda = 1.25$  cm).

Toutefois, ce front d'onde, ayant été découpé par l'ouverture, présente dans tout l'espace image un phénomène diffractif classique, celui associé à une ouverture circulaire illuminée par une onde plane.

La figure 5 représente la distribution en amplitude du champ diffracté observé au plan focal, plan perpendiculaire à l'axe du faisceau diffracté et qui contient l'image géométrique de la source ponctuelle. Cette figure de diffraction est d'ailleurs bien connue sous le nom de figure d'Airy.

Par la suite, notre travail a porté encore sur l'étude des figures de diffraction associées à un système micro-onde parfait, mais cette fois pour des plans d'observation correspondant à certains défauts de mise au point. La figure 6

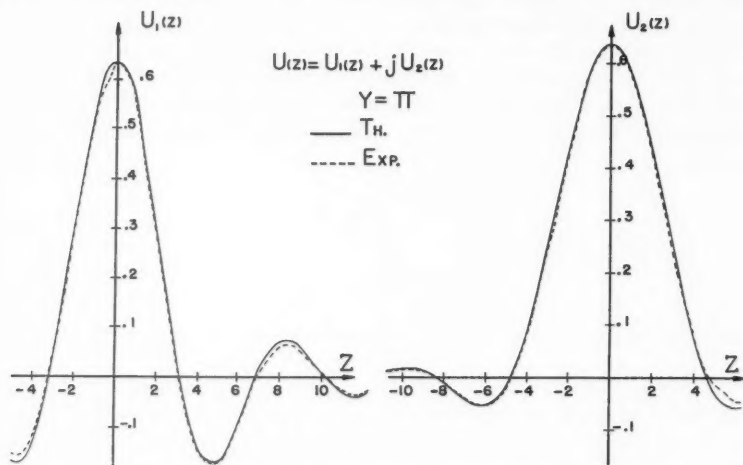


FIG. 6. Distribution de l'amplitude diffractée en présence d'un défaut de mise au point " $y$ " =  $\pi$  (ouverture circulaire;  $\lambda = 1.25$  cm).

représente un cas où l'onde émergeant du système présente un défaut de mise au point de " $y$ " =  $\pi$ . Rappelons ici que le nombre pur " $y$ " représente le double de la différence de phase associée aux chemins optiques du rayon axial et du rayon marginal, comptés depuis l'ouverture jusqu'au centre du plan d'observation. Ce cas a été déterminé sous la forme cartésienne, partie réelle et partie imaginaire.

A ces résultats, nous avons ajouté l'étude de figures de diffraction présentant des défauts de mise au point plus accentués. Par exemple, les figures 7 et 8 s'appliquent à des plans d'observation où " $y$ " est égal respectivement à  $3\pi$  et  $4\pi$ . Ces derniers cas ont été déterminés à l'aide d'un déphaseur variable. Voilà pourquoi l'information fournie est représentée sous la forme polaire, module et phase. De plus, mentionnons que pour l'observation de ces derniers phénomènes (" $y$ " =  $3\pi$ , " $y$ " =  $4\pi$ ), le système optique micro-onde avait été modifié par l'élimination de la seconde lentille aplanétique, de sorte qu'ils ont été observés dans la zone de Fresnel. Pour une étude plus détaillée des



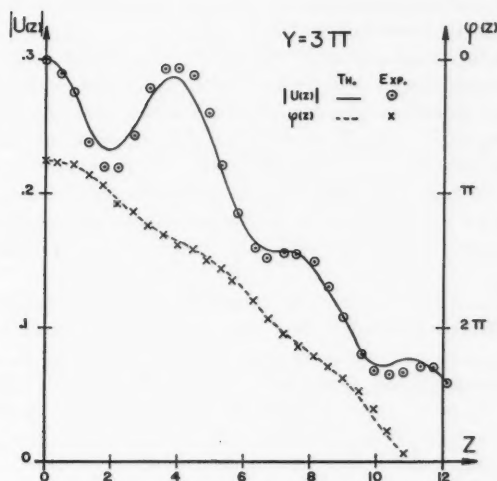


FIG. 7. Distribution de l'amplitude diffractée (forme polaire) en présence d'un défaut de mise au point "y" =  $3\pi$  (ouverture circulaire;  $\lambda = 1.25$  cm).

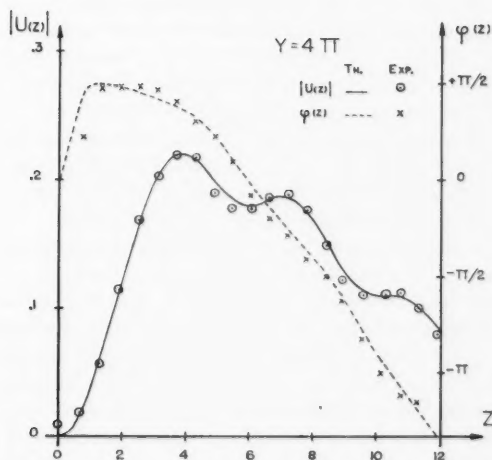


FIG. 8. Distribution de l'amplitude diffractée (forme polaire) en présence d'un défaut de mise au point "y" =  $4\pi$  (ouverture circulaire;  $\lambda = 1.25$  cm).

différents dispositifs utilisés pour l'observation des figures de diffraction associées à une ouverture circulaire illuminée par une onde plane, le lecteur voudra bien consulter Boivin (1960).

Compte tenu de la précision de l'appareil, tous les résultats obtenus présentent une correspondance satisfaisante avec les courbes théoriques, celles-ci étant basées sur la théorie scalaire de la diffraction telle que développée par l'optique classique. Les résultats sont normalisés de sorte que l'amplitude complexe au centre de la figure de diffraction soit identique à celle du point correspondant de la distribution axiale normalisée relativement au foyer. Les courbes théoriques de comparaison utilisées dans cet ouvrage ont été tirées du mémoire classique de Lommel (1885). Mentionnons de plus que les résultats obtenus sont en plein accord avec ceux de Farnell (1958).

Nous aurions eu grand intérêt à étudier les anomalies de phase aux zéros de la figure d'Airy et le long de l'axe. Cependant, ces expériences nécessitant une très grande précision dans les mesures, nous avons jugé qu'elles seront faites dans de meilleures conditions lorsque cet appareil sera muni d'un déphaseur de précision et placé dans une chambre anéchoïque de meilleure qualité.

#### 4. PRÉCISION DES MESURES

Lors des mesures prises dans le champ diffracté associé à un système micro-onde parfait, le procédé de déphasage employé consistait à déplacer l'une des sources suivant l'axe du faisceau diffracté. Une analyse simple de ce procédé montre que l'erreur absolue qu'il cause atteint  $1.1^\circ$  au maximum, tel que mentionné précédemment.

Quant aux réflexions parasites, une étude rapide démontre que ces réflexions changent non seulement le module de la vibration  $U_p$ , mais aussi sa phase, puisqu'il y a cohérence entre toutes ces vibrations. On montre aisément qu'une vibration réfléchie, d'amplitude relative  $\rho$ , cause à la mesure de phase une erreur approximativement égale à  $\rho$  exprimé en radian. Cette approximation ne demeure valable que si le coefficient de réflexion est faible ( $\rho \leq 0.1$ ). Dans le cas présent, des mesures nous ont permis d'établir à .025 le coefficient de réflexion de la chambre anéchoïque que possède ce laboratoire. En conséquence, le coefficient de réflexion .025, exprimé en radian, représente une erreur absolue de  $\pm 1.5^\circ$  sur la détermination de la phase.

Dans cet interféromètre, aux causes d'erreur mentionnées ci-dessus il convient d'ajouter la suivante: la présence d'un obstacle dans l'ouverture diffringente. Une série d'essais a montré que la présence dans l'ouverture  $\Sigma$  d'une section de guide et d'un cornet électromagnétique causait sur  $U_\Sigma$  des variations inférieures à la précision de détection de l'appareil. Ce résultat s'explique facilement puisque la surface relative obstruée est inférieure à 1% et que la section du support faisant obstacle ne dépasse pas  $\lambda/2$ . Toutefois, il faut mentionner que la ligne de balayage, suivie par la sonde qui explore le champ diffracté, doit être parallèle au tronçon de guide qui alimente le cornet source de référence. On minimise ainsi les perturbations que cet obstacle peut causer à  $U_\Sigma$ . On peut songer aussi à déplacer la source ponctuelle de référence

hors de l'ouverture, éliminant ainsi cette cause d'erreur. Dans ce cas, il faudrait, pour un plan d'observation donné, ajuster la position longitudinale de cette source de manière que la courbure du front d'onde sphérique de référence soit identique à celle due au terme en  $e^{-ikR}$  présent dans l'intégrale de la diffraction. Cette condition limiterait l'exploration à un balayage sur une ligne et rendrait le système pratique seulement pour l'étude des phénomènes diffractonnels de révolution.

De cette brève discussion, nous pouvons conclure que la précision des mesures obtenues est la suivante: l'erreur absolue sur la détermination de la phase atteint approximativement  $\pm 2.5^\circ$ .

### 5. CONCLUSION

L'étude préliminaire de ce nouveau type d'interféromètre micro-onde nous a permis de constater que cet appareil possède des caractéristiques vraiment remarquables et qu'il convient admirablement bien aux mesures de l'optique micro-onde. Parmi les caractéristiques de cet appareil, il faut surtout mentionner les suivantes:

1. L'absence de composantes électrodynamiques (joints rotatifs), qui lui permettra de conserver une grande précision dans les mesures de phase au domaine des ondes millimétriques.

2. Le signal de référence distribué en fronts d'ondes sphériques qui conviennent parfaitement bien à l'étude des phénomènes de la diffraction.

3. Une précision élevée qui, par la présence d'un déphaseur de précision et d'une chambre anéchoïque de très bonne qualité, peut atteindre  $\pm 1^\circ$  sur la détermination de la phase.

4. Une grande simplicité de construction et d'opération relativement aux autres types d'interféromètres micro-ondes.

5. Et enfin, des résultats fournis sous une forme qui convient bien à leur comparaison avec les résultats théoriques.

En résumé, on peut affirmer que cet interféromètre à fond cohérent allie d'une manière heureuse des techniques empruntées aux deux domaines des hyperfréquences et de l'optique ordinaire. Ainsi, cet appareil, de par ses caractéristiques, sera bien adapté à l'étude de phénomènes de la diffraction au domaine des ondes millimétriques, l'intérêt de ces ondes étant de réduire l'encombrement des systèmes d'optique micro-onde et de reproduire plus fidèlement les conditions expérimentales propres à l'optique du visible.

### ABSTRACT

We describe in this paper a new type of microwave interferometer based on the free propagation of the reference signal. This apparatus was developed for the study of the distribution of complex amplitude in the diffraction image produced by a microwave optical system. The method is essentially based on the principle of coherent background, use being made of properly polarized sources and of the "turnstile antenna" as a detector. The diffraction pattern is scanned twice to determine the distribution of complex amplitude in Cartesian form, both the real and imaginary parts.

With the aid of such a coherent background interferometer we have studied the complex amplitude distribution in the diffraction pattern at different planes in the image space of an aberration free microwave system. The results obtained are remarkably close to the theoretically predicted ones and, moreover, permit the evaluation of the characteristics and possibilities of this interference technique.

This study shows that the coherent background interferometer will permit measurements of diffraction phenomena in the domain of millimeter waves, which are more appropriate for this type of study.

#### REMERCIEMENTS

Nous sommes heureux de remercier le Conseil National des Recherches qui a gratifié le département de Physique de l'Université Laval d'un octroi permettant la poursuite de ces recherches, et a fait bénéficier d'une bourse l'un des auteurs, soit R. Tremblay. Des remerciements s'adressent également au docteur André Dion et monsieur Raymond Vaillancourt pour les suggestions utiles qu'ils ont faites ainsi qu'à monsieur Pierre Bourassa pour l'aide importante qu'il nous a apportée lors du montage de l'appareil et au cours des mesures.

#### BIBLIOGRAPHIE

- AJIOKA, J. S. 1955. *Proc. I.R.E.* **43**, 1088.  
 ALLEN, P. J. 1956. *IRE Trans. MTT-4*, 223.  
 BACON, J. 1954. *Proc. Natl. Electronics Conf.* **X**, 256.  
 BARRETT, R. M. et BARNES, M. H. 1952. *Electronics*, **25**, 120.  
 BLAIR, G. R. 1958. *Proc. I.R.E., Natl. Conv. Rec. Part 7*, 48.  
 BOIVIN, A. 1960. *Théorie et calcul des figures de diffraction de révolution*. Thèse de doctorat, Université Laval.  
 BROOKS, F. E. 1951. *Proc. I.R.E.* **39**, 407.  
 CULSHAW, W. 1950. *Proc. Phys. Soc. B*, **63**, 939.  
 — 1953. *Proc. Phys. Soc. B*, **66**, 597.  
 FARNELL, G. W. 1958. *Can. J. Phys.* **36**, 935.  
 FLÜGGE, S. 1956. *Handbuch der Physik*, Band XXIV (Springer-Verlag, Berlin), article de M. FRANÇON, p. 322.  
 FROOME, K. 1952. *Proc. Roy. Soc. A*, **213**, 123.  
 — 1954. *Proc. Roy. Soc. A*, **223**, 195.  
 HARDEN, B. N. 1952. *Proc. Inst. Elec. Engrs.* **99**, Pt. III, 229.  
 HULL, C. H., JR. 1952. *Nuovo Cimento, Suppl.* No. 3, **9**, 288.  
 LAVRENCH, W. 1955. *N.R.C. Scientific Association Meeting*, Ottawa, Jan. 5.  
 LENVEL, B. A. 1949. *Proc. I.R.E.* **37**, 1242.  
 LOMMEL, E. 1885. *Abhandl. bayer. Akad.* **15**, 2, 229.  
 MARINER, P. F. 1953. *Elliot Bros. Ltd.*, London, U.K.  
 MEYER, M. A. et GOLDBERG, H. B. 1955. *IRE Trans. MTT-3*, 40.  
 MITTRA, R. 1957. *IRE Trans.* **16**, 248.  
 NIENHUIS, K. 1948. *Ph.D. Thesis*. Groningen University.  
 PAVLASEK, T. J. F. 1958. *Ph.D. Thesis*, McGill University, Montreal.  
 RAGAN, G. L. et NIEMAN, F. L. 1947. *Microwave transmission circuits*, Radiation Lab. Series, Vol. 9 (McGraw-Hill Book Co.).  
 REDHEFFER, R. M. et WIMKLER, R. L. 1945. *RL Report 483-15*, May 11.  
 RICHMOND, J. H. 1955. *IRE Trans. MTT-3*, 13.  
 TREMBLAY, R. 1960. *Thèse de doctorat*, Université Laval, Québec.  
 VERNON, F. L. 1952. *IRE Trans. AP-4*, 110.  
 WORTHINGTON, H. R. 1947. *Rad. Lab. Series. M.I.T.* Vol. **11**, 915.  
 ZERNIKE, F. 1934. *Physica*, **1**, 689.

# DÉPHASEUR MICRO-ONDE À PRISMES DIÉLECTRIQUES<sup>1</sup>

R. TREMBLAY<sup>2</sup>

## RÉSUMÉ

Un nouveau type de déphaseur micro-onde à sections de lignes de longueurs variables a été réalisé. Dans ce dernier, une lame diélectrique à faces parallèles pénètre à travers deux fentes longitudinales non rayonnantes ménagées au milieu des faces larges d'un guide rectangulaire. Cette lame est formée de deux prismes rectangulaires de mêmes angles et placés en opposition. Le déplacement de l'un des prismes dans une direction parallèle à son hypothénuse entraîne l'allongement de la lame diélectrique sise à l'intérieur du guide, d'où résulte un déphasage de l'onde qui traverse ce quadripôle. Nous mentionnons aussi la possibilité de réaliser ce type de déphaseur avec un seul prisme diélectrique.

Les caractéristiques de ce type de déphaseur variable sont les suivantes: résolution de phase élevée, 0,7°; adaptation facile et T.O.S. (taux d'ondes stationnaires) de 1,05; sensibilité faible aux variations de fréquence; déphasage linéaire en fonction du déplacement de l'un des prismes et réalisation mécanique simple.

## 1. INTRODUCTION

### 1.1. Quadripôle de déphasage

Au domaine des hyperfréquences, certains quadripôles ont pour fonction unique de déphaser l'onde qui les traverse. On les emploie principalement dans les techniques de mesures en propagation guidée, dans les systèmes de modulation de phase, dans la détermination en amplitude des champs diffractés et en radioguidage. Différents types de déphaseurs variables ont été mis au point. On peut les grouper de la façon suivante:

1. Déphaseurs à sonde (Ragan et Nieman 1947).
2. Déphaseurs à longueur d'onde de coupure variable (Brady *et al.* 1952).
3. Déphaseurs à lame diélectrique (Ragan et Nieman 1947)
  - (i) à pénétration variable,
  - (ii) à déplacement variable.
4. Déphaseurs à polarisation circulaire
  - (i) rotation mécanique de la direction du plan de polarisation (Fox 1947; Barnett 1955),
  - (ii) rotation de la direction du plan de polarisation par commande électronique (déphaseurs à ferrites) (Sakiotis 1953; Cacheris 1954).
5. Déphaseurs à sections de lignes variables
  - (i) à trombone (Collin 1955; Adey et Britton 1956),
  - (ii) à plans réflecteurs mobiles (Vaillancourt 1957; Saxton et Miller 1948),
  - (iii) à lame diélectrique mobile longitudinalement (Collin 1955).

Une étude critique des caractéristiques de ces déphaseurs variables a été présentée par Collin (1955).

### 1.2. Choix d'un déphaseur approprié aux mesures interférométriques

Le choix d'un type de déphaseur variable dépend des exigences imposées au système de mesure dont il fera partie.

<sup>1</sup>Manuscrit reçu le 4 novembre, 1960.

Contribution du Centre de Recherches en Physique de l'Université Laval, Québec.

<sup>2</sup>Bénéficiaire d'une bourse d'études du Conseil National des Recherches.

Dans un interféromètre micro-onde, le déphaseur variable tient lieu d'étalon de mesure en vue de la détermination des états vibratoires d'un champ électromagnétique. Cette composante, dont la précision limite celle de tout le système, doit posséder les caractéristiques suivantes:

- (1) résolution de phase la plus élevée possible ( $\pm 1^\circ$  ou mieux);
- (2) le module de l'onde transmise ne doit pas changer appréciablement en fonction du déphasage obtenu (très bonne adaptation);
- (3) faible sensibilité aux variations de fréquence;
- (4) le déphasage doit suivre une loi mathématique simple;
- (5) réalisation mécanique aisée (surtout à 24 kMc/sec);
- (6) la perte d'énergie due à l'insertion de ce quadripôle doit être faible.

Ces conditions sont remplies au mieux par le déphaseur à lame diélectrique mobile longitudinalement. Cependant, le nombre de milieux à impédances caractéristiques différentes impliqués dans ce procédé en rend l'adaptation difficile. Aussi avons-nous songé à un nouveau type de déphaseur basé sur ce même principe (lignes variables à lame diélectrique), mais comportant deux seuls milieux d'indices différents.

## 2. DÉPHASEURS À PRISMES DIÉLECTRIQUES

### 2.1. Théorie

La propagation des ondes dans un guide rectangulaire partiellement rempli de diélectrique a été étudiée en détail par plusieurs auteurs (Chambers 1953). La présence de lames diélectriques dans un guide rectangulaire réduit la vitesse de phase de l'onde propagée à une valeur intermédiaire entre les constantes de propagation dans un guide rempli d'air et dans un guide plein de diélectrique. De plus, la longueur d'onde de coupure augmente.

Considérons le cas suivant: une lame diélectrique rectangulaire de côtés  $t$  et  $b$  et de longueur  $l$  est insérée au centre d'un guide rectangulaire (figure 1).

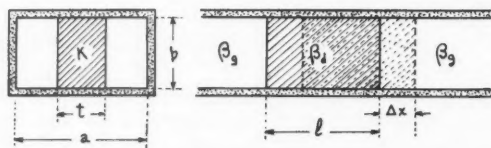


FIG. 1. Guide d'ondes partiellement rempli de diélectrique.

La constante diélectrique  $K$  du matériel utilisé doit être telle que le mode  $TE_{03}$  ne puisse se propager dans ce milieu. Par ailleurs, le mode  $TE_{02}$  n'existe pas, en raison de la symétrie du système.

Collin (1953) a démontré qu'en première approximation la constante de propagation  $\beta_d$  de l'onde guidée dans la section remplie partiellement de diélectrique peut se déduire de l'équation suivante:

$$(1) \quad \beta_d^2 = \beta_0^2 \left[ \frac{t}{a} (K-1) + \left( \frac{K-1}{\pi} \right) \sin \frac{\pi t}{a} \right] - \frac{\pi^2}{a^2},$$

où  $\beta_0$  représente la constante de propagation d'onde dans l'air. La figure 2 donne les valeurs du rapport  $\lambda_d/\lambda_g$  en fonction du paramètre  $t/a$ .

Si l'on varie la longueur  $l$  de la lame diélectrique d'une quantité  $\Delta x$ , le déphasage ainsi obtenu est donné par la relation suivante:

$$(2) \quad \phi = (\beta_g - \beta_d) \cdot \Delta x,$$

dans laquelle  $\beta_g$  représente la constante de propagation de l'onde dans le guide rempli d'air. On remarque que la variation de la phase en fonction de  $\Delta x$  est linéaire. Le terme  $(\beta_g - \beta_d) = \Psi$  représente le taux de variation de la phase en rad/cm. La variation de ce terme pour différentes valeurs des paramètres  $t$  et  $a$  est représentée par les courbes de la figure 3.

Selon l'équation (2), l'allongement de la lame diélectrique insérée dans le guide d'onde nous permettrait d'obtenir un quadripôle de déphasage variable. Nous allons maintenant décrire deux procédés qui conduisent à ce résultat.

### 2.2. Méthode A: prismes semblables placés en opposition

Considérons, en optique, le compensateur de phase suivant: une lame à faces parallèles est formée de deux coins (prismes) de même indice  $n$  placés en opposition (figure 4). À l'aide d'une vis micrométrique, on peut déplacer l'un des prismes par rapport à l'autre dans une direction parallèle aux hypothénuses de ces prismes. Ainsi, l'épaisseur de la lame à faces parallèles varie d'une quantité  $\Delta x$  et l'onde lumineuse qui la traverse subit un déphasage:

$$(3) \quad \phi = (\beta_d - \beta_0) \cdot \Delta x = \frac{2\pi}{\lambda_0} (n-1) \cdot \Delta x.$$

Appliquons maintenant ce principe à la propagation guidée. Dans un guide d'onde rectangulaire, on pratique une fente longitudinale non rayonnante au centre des deux faces larges du guide (figure 5). La largeur de la fente dépend de l'épaisseur  $t$  de la lame diélectrique qu'on désire introduire dans le guide pour obtenir un taux de déphasage  $\Psi$  donné. Introduisons dans ces fentes une lame diélectrique à faces parallèles, d'épaisseur  $t$ , et formée de deux triangles rectangles d'angle  $\alpha$  placés en opposition. L'un de ces prismes est fixe, tandis que l'autre peut se déplacer suivant son hypothénuse. Un déplacement  $\Delta d$  de ce prisme produit un déphasage de l'onde guidée transmise:

$$(4) \quad \phi = (\beta_g - \beta_d) \sin \alpha \cdot \Delta d.$$

On réalise ainsi un déphaseur variable à caractéristique linéaire, basé sur le principe des lignes de longueur variable. On remarquera que ce système peut s'adapter facilement. En effet, pour en réaliser l'adaptation à un guide rempli d'air, il suffit de munir les faces  $AA'$  et  $BB'$  de transformateurs quart-d'ondes en diélectrique (Collin et Brown 1954). Mentionnons, de plus, que l'angle  $\alpha$  fournit un paramètre supplémentaire, permettant de modifier le taux de variation de la phase,  $(\beta_g - \beta_d) \sin \alpha$ .



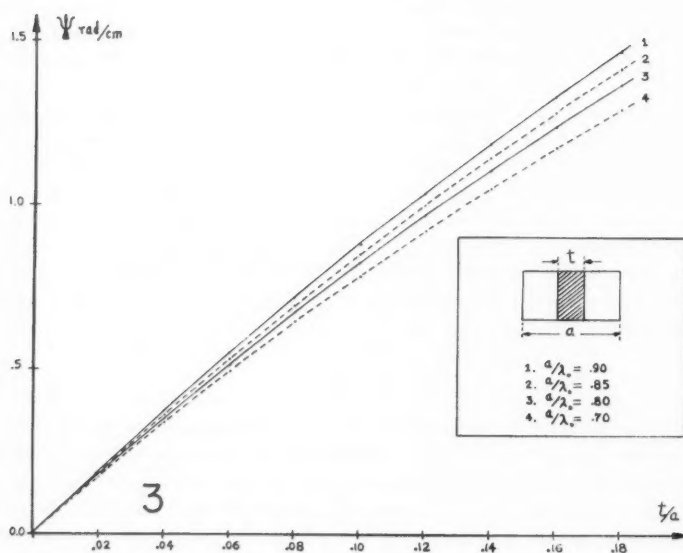
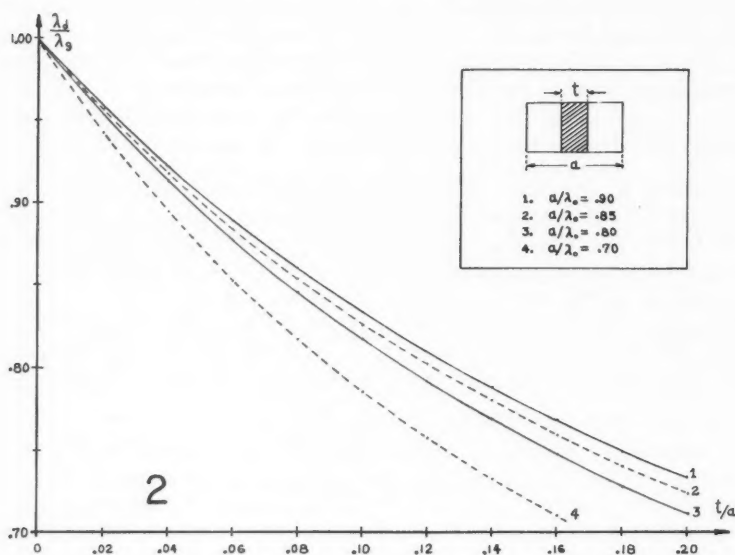


FIG. 2. Guide d'ondes partiellement rempli de diélectrique: Valeurs du rapport  $\lambda_d/\lambda_g$  en fonction de  $t/a$ .

FIG. 3. Guide d'ondes partiellement rempli de diélectrique: Taux de variation de la phase (rad/cm) en fonction de  $t/a$ .



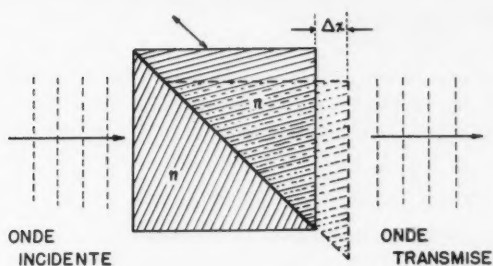


FIG. 4. Compensateur optique.

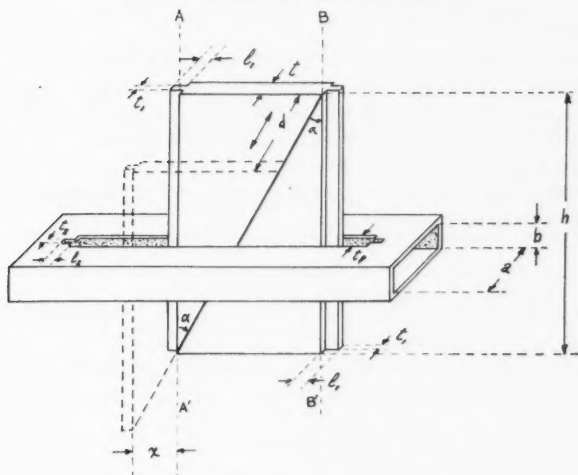


FIG. 5. Déphaseur micro-onde à prismes diélectriques.

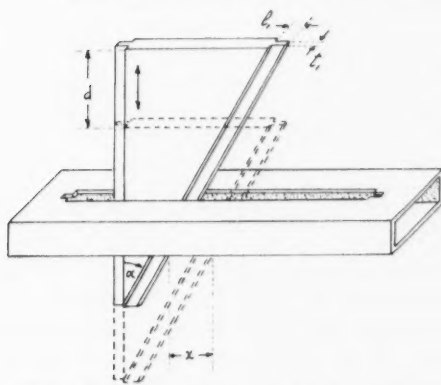


FIG. 6. Déphaseur micro-onde à prisme diélectrique unique.

### 2.3. Méthode B: prisme unique

Cette méthode n'est qu'une modification de la méthode A. La lame diélectrique introduite dans le guide d'onde n'est plus à faces parallèles, mais à angle  $\alpha$ . Ainsi, un seul coin de diélectrique d'épaisseur  $t$  suffit pour réaliser ce déphaseur (figure 6). Le déphasage obtenu peut être représenté par l'équation suivante:

$$(5) \quad \phi = (\beta_g - \beta_d) \tan \alpha \cdot \Delta d.$$

Les caractéristiques de ce déphaseur ne diffèrent pas de celles obtenues par la méthode A.

## 3. RÉALISATION EXPÉRIMENTALE

### 3.1. Description

Dans le but de vérifier les caractéristiques de ce nouveau type de déphaseur à lignes variables, nous en avons construit un exemplaire. La longueur de la lame diélectrique introduite dans le guide varie suivant le procédé décrit à la méthode A. La fréquence d'utilisation est de 24 kMc/sec ( $\lambda_0 = 1.25$  cm), et chacune des faces de la lame possède un adaptateur quart-d'onde calculé à cette fréquence. Le Tableau I groupe les principales dimensions de ce déphaseur. Les symboles réfèrent au schéma de la figure 5.

TABLEAU I  
Principales dimensions du déphaseur

	Symboles et unités	Modèle A
Dimensions du guide d'onde	$a$ , po.	0.420
	$b$ , po.	0.170
Épaisseur de la lame	$t$ , po.	0.033
Constante diélectrique	$K$	2.56
Angle des prismes	$\alpha$ degrés	45
Hauteur des prismes	$h$ , po.	3.50
Largeur de la fente	$t_1$ po.	0.035
Longueur de la fente	$l_1$ po.	4.50
Adaptateurs de la lame		
longueur	$l_1$ po.	0.140
largeur	$t_1$ po.	0.015
Adaptateurs de la fente		
longueur	$l_2$ po.	0.150
largeur	$t_2$ po.	0.016
Allongement maximum de la lame	$X_{\max}$ po.	2.00

Dans la réalisation expérimentale, le prisme fixe a été tronqué. Cela n'amène aucun inconvénient puisque seule la partie intérieure au guide contribue au parallélisme des faces de la lame.

### 3.2. Calibration et caractéristiques expérimentales

#### (i) T.O.S. (taux d'ondes stationnaires)

L'adaptation de ce quadripôle à un guide rempli d'air a été calculée pour une fréquence d'utilisation de 24 kMc/sec. Cependant, d'après la figure 7, cette condition semble mieux remplie à 23.5 kMc/sec. Cet écart s'explique bien, puisque dans les calculs précédents nous n'avons pas tenu compte des

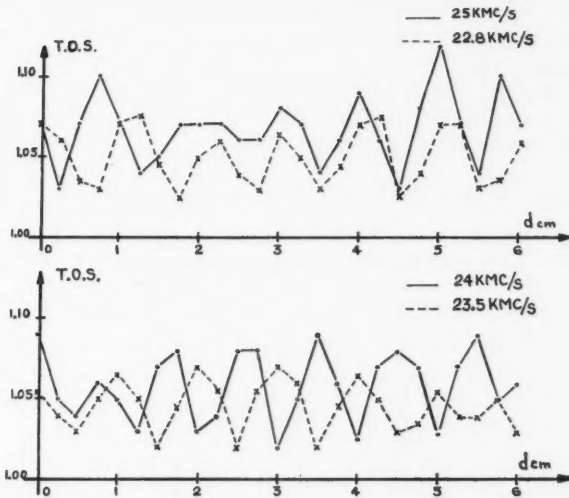


FIG. 7. T.O.S. (taux d'ondes stationnaires) en fonction de l'allongement de la lame diélectrique.

modifications apportées à la constante de propagation de l'onde guidée par la présence des fentes longitudinales non rayonnantes. De plus, le rapport de  $\lambda_d/\lambda_g$ , calculé à l'aide de l'équation (1), ne donne qu'un résultat approximatif (4%). Si l'on tient compte du fait que chaque flasque introduite entre la sonde et la terminaison lors de la mesure du T.O.S. possède un T.O.S. propre de 1.01, on peut affirmer que celui du déphaseur ne dépasse pas 1.05.

En considérant les courbes représentées à la figure 7, on peut observer une caractéristique importante de ce nouveau type de déphaseur. Bien qu'il ait été adapté pour une fréquence unique à l'aide d'un seul transformateur quart-d'onde, le T.O.S. de ce quadripôle demeure très faible sur une largeur de bande assez grande. De 22.8 kMc/sec à 25 kMc/sec, il demeure inférieur à 1.10. Il serait donc facile de parfaire l'adaptation de ce déphaseur sur une telle bande de fréquence. Cette caractéristique découle du fait que pour obtenir un taux de déphasage  $\Psi$  appréciable,  $t/a$  conserve une valeur assez faible (figure 3). Ainsi, le rapport de l'impédance du guide partiellement rempli de diélectrique à celle du guide rempli d'air est près de l'unité (cas présent 1.16) et peu sensible à la variation de la fréquence d'utilisation. Tel n'est point le cas dans les autres types de déphaseurs à lames diélectriques où ce rapport est beaucoup plus élevé, et atteint même des valeurs supérieures à 2. Ils demandent une adaptation beaucoup plus complexe et demeurent plus sensibles aux variations de la fréquence d'utilisation.

#### (ii) Déphasage

La variation de la phase en fonction de l'allongement de la lame a été mesurée par détection de la position des minima de l'onde stationnaire formée

dans un guide terminé par un court-circuit mobile, le déphaseur étant inséré entre la sonde et le court-circuit (Montgomery 1949). Comme l'adaptation du quadripôle n'était pas parfaite, le résultat découle d'une moyenne de deux mesures, l'une pour une position quelconque  $l_1$  du court-circuit, l'autre à  $l_2 = l_1 + \lambda_g/4$ . On sait que cette double mesure élimine les erreurs dues aux réflexions parasites dans le système, si elles ne sont pas trop élevées (cas présent).

Des résultats obtenus (Tableau II) on observe que la déphasage en fonction

TABLEAU II  
Variation de la phase en fonction de l'allongement de la lame diélectrique

$\Delta d$ (cm)	$\phi$ (degrés)	$\Delta\phi$ (degrés)
0.0	0.0	
0.50	14.9	14.9
1.00	30.0	15.1
1.50	44.8	14.8
2.00	59.4	14.6
2.50	74.3	14.9
3.00	89.5	15.2
3.50	105.3	15.8
4.00	122.8	17.5
4.50	140.3	17.5
5.00	158.1	17.8
5.50	174.4	16.3
6.00	189.2	15.8

de la longueur de la lame diélectrique insérée dans le guide suit une relation linéaire à  $\pm 0.7^\circ$ .

Le Tableau III présente la valeur de  $\Psi$  à différentes fréquences. On remar-

TABLEAU III  
Taux de variation de la phase à différentes fréquences d'utilisation

Fréquence (kMc/sec)	25	24.5	24	23.5	23
$\Psi$ (rad/cm)	0.763	0.749	0.738	0.722	0.713

quera, d'après ces résultats, que ce type de déphaseur est peu sensible aux variations de fréquence.

Si l'on considère à nouveau les résultats obtenus (Tableau II), on constate que dans la région  $4 \leq d \leq 5.0$  la mesure s'éloigne de la linéarité par plus d'un degré. Cet écart est dû à la non-uniformité de la lame dans cette région. Ceci nous amène à considérer les tolérances permises dans la construction d'un déphaseur de ce type.

(iii) Causes d'erreurs

Si les discontinuités présentes dans ce quadripôle de déphasage variable sont bien adaptées, l'écart entre la mesure et la linéarité théorique du système peut provenir des trois causes suivantes:

- (a) inhomogénéité du diélectrique,
- (b) mauvais alignement des fentes,

(c) non-uniformité de l'épaisseur de la lame.

La première cause est négligeable, puisque les diélectriques présentement disponibles sur le marché possèdent une homogénéité remarquable.

Les fentes longitudinales non rayonnantes ménagées sur les faces larges du guide introduisent une variation de la longueur d'onde dans le guide, mais ce phénomène n'affecte pas la linéarité. Il ne fait que modifier légèrement le taux de déphasage ( $\Psi$ ). Un mauvais parallélisme de la fente par rapport aux faces étroites du guide imposerait à la lame un déplacement dans un champ électrique non uniforme et, de là, causerait une variation de phase non linéaire en fonction de ce déplacement. Cette erreur s'élimine facilement par une réalisation mécanique soignée.

À quelques pour-cent près, les relations (1) et (2) permettent de déterminer la variation apportée à  $\Psi$  par un changement d'épaisseur de la lame. On trouve l'expression suivante:

$$(6) \quad \frac{\Delta\Psi}{\Delta t} = \frac{\beta_0^2(K-1)}{2\beta_0 a} \left(1 + \cos \frac{\pi t}{a}\right).$$

Dans le cas présentement envisagé ( $\lambda_0 = 1.25$  cm,  $t/a = 0.078$ ), cette relation impose à  $t$  une tolérance de  $\pm 0.001$  cm, si l'on désire que le système soit linéaire à  $\pm \frac{1}{2}^\circ$ . Cette tolérance est faible mais elle demeure cependant mécaniquement réalisable. Du reste, cette exigence d'une construction précise est commune à maintes composantes micro-ondes réalisées pour cette fréquence d'utilisation ( $\nu = 24$  kMc/sec).

#### 4. DISCUSSION

En résumé, ce nouveau type de déphaseur à lignes variables présente les caractéristiques suivantes:

- (1) résolution de phase élevée,  $\pm 0.7^\circ$ ;
- (2) T.O.S., propre au quadripôle, de 1.05;
- (3) très faible sensibilité aux variations de fréquence;
- (4) le déphasage en fonction de l'allongement de la lame suit une loi mathématique simple, une relation linéaire;
- (5) réalisation mécanique précise, mais simple;
- (6) les pertes d'énergie dues à l'insertion de ce quadripôle dans le système sont négligeables.

De plus, par rapport au déphaseur à lame diélectrique mobile longitudinalement (choix initial comme meilleur déphaseur), ce nouveau type présente les avantages suivants:

- (i) adaptation plus facile,
- (ii) encombrement moindre (on peut facilement atteindre un taux de déphasage de 1 rad/cm).

Toutes ces caractéristiques nous amènent à considérer ce type de déphaseur comme une composante micro-onde de précision. Elle remplit toutes les exigences imposées à un système pour la détermination de l'état d'un phénomène vibratoire. Par conséquent, son emploi se trouvera particulièrement indiqué pour l'étude des champs diffractés et pour toutes les autres mesures interférométriques au domaine des ondes centimétriques.

## ABSTRACT

A new type of microwave phase shifter has been constructed, which has line sections of variable length. In this device, a dielectric plate with parallel faces passes through two longitudinal slits on the larger faces of a rectangular waveguide. This plate is formed of two identical prisms placed in opposition. The displacement of one of the prisms relative to the other along the hypotenuse changes the effective length of the dielectric plate within the guide, with a consequent shift of the wave that traverses this quadrupole. The possibility of designing a phase shifter of this type using only a single prism is also discussed.

The characteristics of this type of variable phase shifter are as follows: high phase resolution,  $0.7^\circ$ ; easy matching, S.W.R. of 1.05; weak sensitivity to frequency variations; phase shift linear with respect to the displacement of one of the prisms; and very simple mechanical construction.

## REMERCIEMENTS

Ce travail a été effectué au Centre de Recherches en Physique de l'Université Laval, sous la direction avisée du directeur de la section d'Optique des micro-ondes, le Dr Albéric Boivin, qui a droit à mes remerciements les plus sincères. Je remercie également monsieur Raymond Vaillancourt pour les suggestions qu'il apporta au cours de la rédaction de cette publication. Le Conseil National des Recherches a fait bénéficier l'auteur d'une bourse généreuse, et a gratifié le Centre de Recherches en Physique d'un octroi permettant la poursuite de ces recherches. À cet organisme s'adressent des remerciements spéciaux.

## BIBLIOGRAPHIE

- ADEY, A. et BRITTON, J. 1956. *Can. J. Phys.* **34**, 11, 1112.  
 BARNETT, E. F. 1955. *Hewlett-Packard Journal*, **6**, No. 5.  
 BRADY, J., PEARSON, M. D. et PEOPLES, S. 1952. *Rev. Sci. Instr.* **23**, No. 11, 601.  
 CACHERIS, J. 1954. *Proc. I.R.E.* **42**, No. 8, 1242.  
 CHAMBERS, L. G. 1953. *Brit. J. Appl. Phys.* **4**, No. 2, 39.  
 COLLIN, R. 1953. University of London, Ph.D. Thesis.  
 ——— 1955. *Wireless Eng.* **32**, No. 3, 82.  
 COLLIN, R. et BROWN, J. 1954. *Wireless Eng.* **31**, No. 2, 31.  
 FOX, A. G. 1947. *Proc. I.R.E.* **35**, 1489.  
 MONTGOMERY, C. G. 1949. *Technique of microwave measurements*, Radiation Lab. Series, Vol. 2 (McGraw-Hill Book Co.).  
 RAGAN, G. L. et NIEMAN, F. L. 1947. *Microwave transmission circuits*, Radiation Lab. Series, Vol. 9 (McGraw-Hill Book Co.).  
 SAKIOTIS, N. G. 1953. *Proc. I.R.E.* **41**, No. 1, 87.  
 SAXTON, G. et MILLER, C. W. 1948. *Wireless Eng.* **25**, No. 5, 138.  
 VAILLANCOURT, R. 1957. *IRE Trans. MTT-5*, No. 3, 204.

## THE RAMAN SPECTRUM OF METHANE- $d_4$ <sup>1</sup>

R. A. OLAFSON, M. A. THOMAS, AND H. L. WELSH

### ABSTRACT

The Raman spectrum of  $CD_4$  at 1 atm pressure was photographed with a spectral resolution of  $\sim 0.4 \text{ cm}^{-1}$ , and rotational analyses of the  $\nu_2$  and  $\nu_3$  bands were carried out. The  $B_0$  values obtained from the  $\nu_2$  and  $\nu_3$  bands are  $2.6330 \pm 0.0007$  and  $2.6328 \pm 0.0007 \text{ cm}^{-1}$ , respectively; the value of  $r_0$  determined from the former is  $1.09181 \pm 0.00029 \text{ \AA}$ . The rotational levels of the  $v = 1$  state of  $\nu_2$  are split with effective  $B_1$  values equal to 2.6894, 2.7351, and  $2.7434 \text{ cm}^{-1}$ . Thirteen of the fifteen branches of the  $\nu_3$  band were observed; these also show multiple  $B_1$  values. The value obtained for  $\zeta_3$  is 0.1648. Structure was observed but not analyzed in the  $\nu_1$ ,  $2\nu_4$ , and  $\nu_2 + \nu_4$  bands. On the basis of the Raman data the structures of the  $\nu_2$  and  $\nu_3$  infrared bands are discussed.

### INTRODUCTION

The present communication presents some recent results on the Raman spectrum of methane- $d_4$ , and forms the second in a series of high-resolution studies of the Raman spectra of methane and its deuterated species; the first (Thomas and Welsh 1960) was concerned with the spectrum of methane.

Methane- $d_4$  ( $CD_4$ ), like ordinary methane ( $CH_4$ ), is a spherical top molecule (point-group  $T_d$ ) and has four normal modes of vibration, one totally symmetric,  $\nu_1(a_1)$ , one doubly degenerate,  $\nu_2(e)$ , and two triply degenerate,  $\nu_3(f_2)$  and  $\nu_4(f_2)$ , all of which are active in the Raman effect. The  $\nu_1$ ,  $\nu_2$ , and  $\nu_3$  bands were photographed by Shepherd and Welsh (1957) at a gas pressure of 1 atm with a prism spectrograph giving a reciprocal linear dispersion of  $10.5 \text{ cm}^{-1}$  per mm at  $4358 \text{ \AA}$ . The structure of the  $\nu_2$  fundamental showed that the rotational levels of the upper vibrational state of this vibration are split into two components. An analysis of the  $\nu_3$  band was possible only by assuming different values of the rotational constant  $B_1$  for the three substates (+, 0, -) formed by the Coriolis interaction of the mutually degenerate vibrations. These departures from the simple theory are similar to those observed in the spectrum of ordinary methane (Stoicheff *et al.* 1952; Thomas and Welsh 1960).

The development of a grating spectrograph of high light-power was the pretext for a re-examination of the spectrum of methane- $d_4$ . This instrument, which will be described in detail elsewhere, has a reciprocal linear dispersion of  $6 \text{ cm}^{-1}$  per mm at  $4358 \text{ \AA}$  and a practical resolving power of  $\sim 0.4 \text{ cm}^{-1}$ . The Raman tube, 1.1 m long with a volume of 1.7 l., was equipped with a multiple reflection mirror system, and was irradiated by four hairpin-shaped mercury arcs with water-cooled electrodes operated at 17 amp. The Raman tube was filled with high purity  $CD_4$  gas (Merck and Co.) to a pressure of 1 atm. The  $\nu_1$ ,  $\nu_2$ , and  $\nu_3$  fundamentals were photographed; as in the earlier investigation, the  $\nu_4$  band was too weak to be observed.

In the following the method of analysis of the Raman bands will be outlined.

<sup>1</sup>Manuscript received November 17, 1960.

Contribution from the McLennan Laboratory, University of Toronto, Toronto, Ontario. This research was supported in part by funds from the National Research Council of Canada.



In addition, molecular constants determined from the Raman spectrum will be used in analyses of the  $\nu_2$  and  $\nu_3$  infrared bands which have been recorded at high dispersion by Kaylor and Nielsen (1955).

### THE $\nu_2$ BAND

#### *The Raman Spectrum*

The  $\nu_2$  band is very weak and long exposures were necessary to obtain useful spectrograms. Measurements were made from two plates, one with an exposure time of 115 hours and a spectral slit width of  $0.4 \text{ cm}^{-1}$ , and one with an exposure time of 90 hours and a spectral slit width of  $0.3 \text{ cm}^{-1}$ ; the exciting line was Hg 4358 in both cases. A microphotometer trace of the first of these spectrograms is shown in Fig 1. The frequency shifts, averaged from two independent measurements of each plate, are given in Table I.

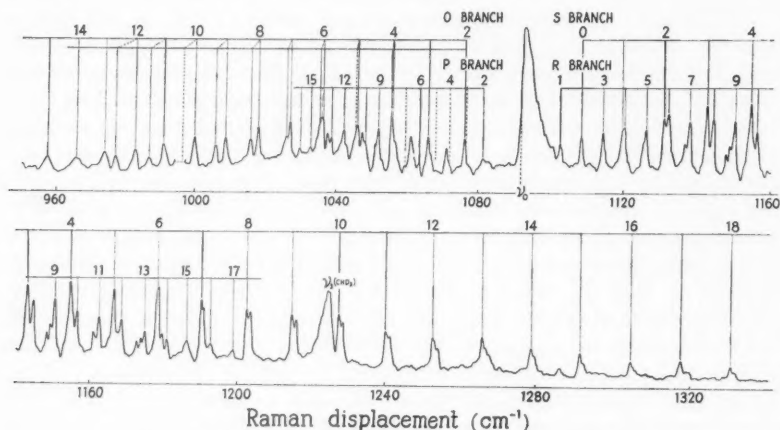


FIG. 1. Microphotometer trace of the  $\nu_2$  Raman band of  $\text{CD}_4$ .

The rotational transitions in the  $\nu_2$  fundamental are expected to follow the selection rules,  $\Delta J = 0, \pm 1, \pm 2$ ,  $J' + J'' \geq 2$ , where  $J$  is the rotational quantum number; the band should therefore show  $O$ ,  $P$ ,  $Q$ ,  $R$ , and  $S$  branches. However, as shown by Shepherd and Welsh (1957), the rotational levels of the upper vibrational state appear to be split into a lower level ( $\alpha$ ) and an upper level ( $\beta$ ). The earlier analysis indicated that  $O^\beta$ ,  $P^\alpha$ ,  $Q^\alpha$ ,  $R^\alpha$ , and  $S^\beta$  branches were present in the Raman spectrum. The better resolved spectrograms obtained in the present investigation show the presence of  $O^\beta$ ,  $O^\alpha$ ,  $P^\beta$ ,  $Q^\alpha$ ,  $R^\alpha$ , and  $S^\beta$  branches; a few lines of an additional  $S$  series, designated  $S^\gamma$ , were also observed. The assignments are given in Table I and in Fig. 1.

The  $O^\beta$  and  $S^\beta$  lines were used in the determination of the ground state molecular constants associated with the band. The rotational energy levels of the  $\nu$ th vibrational state are given by

$$(1) \quad F_v(J) = B_v J(J+1) - D_v J^2(J+1)^2, \quad J = 0, 1, 2, \dots$$

TABLE I  
 Raman frequencies of the  $\nu_2$  band of CD<sub>4</sub>

$\Delta\nu(\text{obs.})$ $\text{cm}^{-1}$	Assignment	$\Delta\nu(\text{calc.})$ $\text{cm}^{-1}$	$\Delta\nu(\text{obs.})$ $\text{cm}^{-1}$	Assignment	$\Delta\nu(\text{calc.})$ $\text{cm}^{-1}$
957.4	$O^\beta(15)$	957.7	1136.7	—	—
965.5	$O^\beta(14)$	965.7	1137.7	$R^\alpha(7)$	1137.7
973.8 <sup>a</sup>	$O^\beta(13)$	973.9	1142.3	$S^\beta(3)$	1142.3
976.7	$O^\alpha(12)$	977.0	1144.0	$R^\alpha(8)$	1143.8
982.2 <sup>a</sup>	$O^\beta(12)$	982.2	1147.8	—	—
986.3	$O^\alpha(11)$	986.5	1148.8	—	—
990.7 <sup>a</sup>	$O^\beta(11)$	990.7	1149.9	$R^\alpha(9)$	1149.9
999.4 <sup>a</sup>	$O^\beta(10)$	999.4	1154.1	$S^\beta(4)$	1154.0
1005.5	$O^\alpha(9)$	1005.6	1155.9	$R^\alpha(10)$	1156.1
1008.2 <sup>a</sup>	$O^\beta(9)$	1008.3	1160.6	—	—
1015.4	$O^\alpha(8)$	1015.4	1162.1	$R^\alpha(11)$	1162.2
1017.3 <sup>a</sup>	$O^\beta(8)$	1017.3	1165.9	$S^\beta(5)$	1165.9
1025.2	$O^\alpha(7)$	1025.2	1168.3	$R^\alpha(12)$	1168.4
1026.2 <sup>a</sup>	$O^\beta(7)$	1026.6	1172.5	—	—
1029.2	$P^\beta(16)$	1030.6	1173.6	—	—
1032.2	$P^\beta(15)$	1033.2	1174.5	$R^\alpha(13)$	1174.5
1035.2	$O^\alpha(6)$	1035.2	1177.9	$S^\beta(6)$	1177.9
1036.0	$O^\beta(6); P^\beta(14)$	1036.1; 1036.0	1178.4	$S^\gamma(6)$	1178.3
1037.1	—	—	1179.4	—	—
1038.3	$P^\beta(13)$	1038.8	1180.7	$R^\alpha(14)$	1180.6
1041.9	$P^\beta(12)$	1041.9	1186.6	$R^\alpha(15)$	1186.6
1045.7	$O^\beta(5); O^\alpha(5); P^\beta(11)$	1045.8; 1045.2; 1045.1	1190.1 <sup>a</sup>	$S^\beta(7)$	1190.1
1046.9	—	—	1190.7	$S^\gamma(7)$	1190.6
1048.0	$P^\beta(10)$	1048.3	1192.7	$R^\alpha(16)$	1192.6
1050.7	—	—	1198.8	$R^\alpha(17)$	1198.4
1051.6	$P^\beta(9)$	1051.8	1202.4 <sup>a</sup>	$S^\beta(8)$	1202.4
1055.6	$O^\beta(4); O^\alpha(4); P^\beta(8)$	1055.7; 1055.4; 1055.5	1203.2	$S^\gamma(8)$	1202.9
1060.9	—	—	1214.8 <sup>a</sup>	$S^\beta(9)$	1214.8
1063.3	$P^\beta(6)$	1063.4	1215.8	$S^\gamma(9)$	1215.4
1065.6	$O^\beta(3); O^\alpha(3)$	1065.8; 1065.8	1224.3	$\nu_2(\text{CD}_3\text{H})(4047)$	—
1071.0	$P^\beta(4)$	1072.1	1227.3 <sup>a</sup>	$S^\beta(10)$	1227.3
1076.0	$O^\beta(2); O^\alpha(2)$	1076.1; 1076.1	1228.2	$S^\gamma(10)$	1228.0
1081.1	$P^\beta(2)$	1081.6	1240.0 <sup>a</sup>	$S^\beta(11)$	1240.0
1092.6	$Q(\text{max})$	—	1241.2	$S^\gamma(11)$	1240.6
1102.4	$R^\alpha(1)$	1102.8	1252.7 <sup>a</sup>	$S^\beta(12)$	1252.7
1108.2	$R^\alpha(2); S^\beta(0)$	1108.4; 1108.3	1253.6	$S^\gamma(12)$	1253.3
1114.1	$R^\alpha(3)$	1114.1	1265.5 <sup>a</sup>	$S^\beta(13)$	1265.5
1119.5	$S^\beta(1)$	1119.5	1278.4 <sup>a</sup>	$S^\beta(14)$	1278.4
1120.0	$R^\alpha(4)$	1119.9	1291.2 <sup>a</sup>	$S^\beta(15)$	1291.2
1125.9	$R^\alpha(5)$	1125.8	1304.1 <sup>a</sup>	$S^\beta(16)$	1304.1
1130.9	$S^\beta(2)$	1130.8	1317.0 <sup>a</sup>	$S^\beta(17)$	1317.0
1131.8	$R^\alpha(6)$	1131.7	1330.2	$S^\beta(18)$	1329.9

<sup>a</sup>Lines used in the determination of the ground state constants.

The Raman shifts of the  $O(\Delta J = -2)$  and  $S(\Delta J = +2)$  lines can therefore be represented by the formula

$$(2) \quad \Delta\nu = a + bm + cm^2 - dm^3 - em^4,$$

where  $m = -2J+1$ ,  $J = 2, 3, \dots$  for the  $O$  branch, and  $m = 2J+3$ ,  $J = 0, 1, \dots$  for the  $S$  branch, and the coefficients are:

$$\begin{aligned} a &= \nu_0 + (3/4)(B_1 - B_0) - (9/16)(D_1 - D_0), \\ b &= (B_1 + B_0) - (3/2)(D_1 + D_0), \\ c &= (1/4)(B_1 - B_0) - (11/8)(D_1 - D_0), \\ d &= (1/2)(D_1 + D_0), \\ e &= (1/16)(D_1 - D_0). \end{aligned}$$

Eighteen unblended and well-defined  $O^{\beta}$  and  $S^{\beta}$  lines, the frequencies of which are marked in Table I by the superscript  $a$ , were used to determine the following values of the coefficients in (2) by a least squares analysis using an IBM 650 electronic computer:

$$\begin{aligned}a &= 1092.01 \pm 0.03, \\b &= 5.3680 \pm 0.0013, \\c &= 0.02547 \pm 0.00012, \\d &= (7.23 \pm 0.25) \times 10^{-5}, \\e &= (0.26 \pm 0.01) \times 10^{-5}.\end{aligned}$$

The errors given here are the probable errors in the coefficients obtained from the least squares calculation; they are a measure of the scatter of the experimental points. From these coefficients the following values of the constants were determined:

$$\begin{aligned}\nu_0 &= 1091.93 \pm 0.03 \text{ cm}^{-1}, \\B_0 &= 2.6330 \pm 0.0007 \text{ cm}^{-1}, \\B_1^{\beta} &= 2.7351 \pm 0.0007 \text{ cm}^{-1}, \\D_0 &= (5.1 \pm 0.3) \times 10^{-5} \text{ cm}^{-1}, \\D_1^{\beta} &= (9.3 \pm 0.3) \times 10^{-5} \text{ cm}^{-1}.\end{aligned}$$

The analysis of the remaining branches was carried out by assuming these values of  $\nu_0$ ,  $B_0$ , and  $D_0$ , and using the observed frequencies,  $\Delta\nu(J)$ , to calculate the rotational energies,  $F_1(J')$ , of the upper vibrational state from the formula

$$(3) \quad F_1(J') = \Delta\nu(J) + F_0(J) - \nu_0.$$

The upper state constants,  $B_1$  and  $D_1$ , for a given series were then determined by a least squares analysis from the equation

$$(4) \quad F_1(J)/J(J+1) = B_1 - D_1J(J+1).$$

Plots of this equation are shown in Figs. 2 and 3.

The  $S^{\beta}$  lines for  $J > 6$  show a splitting into two components (Fig. 1). The higher frequency components of these doublets give points for equation (4) which lie on a well-defined straight line (Fig. 2); the derived constants are  $B_1^{\gamma} = 2.7434 \pm 0.0007$  and  $D_1^{\gamma} = (11.0 \pm 0.5) \times 10^{-5} \text{ cm}^{-1}$ . For comparison, a similar graph of equation (4) for the  $O^{\beta}$  and  $S^{\beta}$  lines, used in the least squares analysis given above, is shown in Fig. 2.

The errors given for the above values are the probable errors resulting from the least squares calculation; they do not take into account the probable errors of the assumed values of  $\nu_0$ ,  $B_0$ , and  $D_0$ . In this case and in similar cases below estimated errors will be given; these were obtained by compounding the probable errors in  $B_1$  or  $D_1$  with the probable errors in  $B_0$  or  $D_0$ . The values thus become  $B_1^{\gamma} = 2.7434 \pm 0.0010$  and  $D_1^{\gamma} = (11.0 \pm 0.6) \times 10^{-5} \text{ cm}^{-1}$ .

The graph of equation (4) for the  $O^{\alpha}$  and  $R^{\alpha}$  lines is shown in Fig. 3. The points

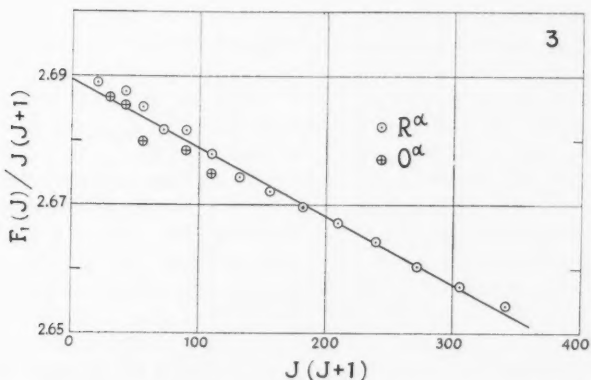
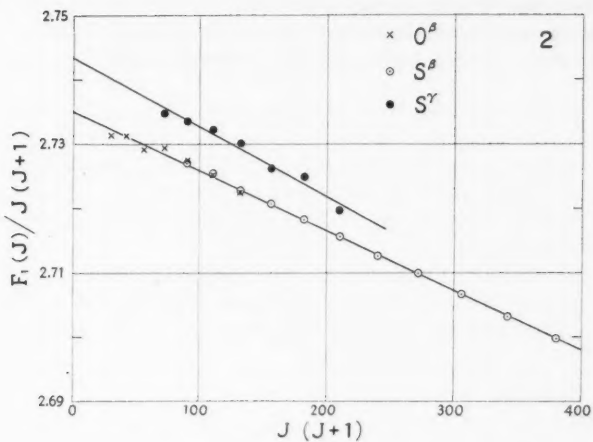


FIG. 2. Determination of the upper state rotational constants of the  $S^\gamma$  branch of the  $\nu_2$  band. For comparison the corresponding plot for the  $O^\beta$  and  $S^\beta$  branches is also shown.

FIG. 3. Determination of the upper state rotational constants of the  $O^\alpha$  and  $R^\alpha$  branches of the  $\nu_2$  band.

for both of these series lie on a single straight line for which a least squares calculation with estimated errors gave  $B_1^\alpha = 2.6894 \pm 0.0008 \text{ cm}^{-1}$  and  $D_1^\alpha = (10.6 \pm 0.4) \times 10^{-5} \text{ cm}^{-1}$ . It is noteworthy that, although an  $O^\alpha$  branch is present, there is no evidence for an  $S^\alpha$  branch, whereas the satellite components,  $S^\gamma$ , have no counterpart in the  $O$  branch.

The  $P$  branch appears to be more strongly perturbed than the other branches. Most of the lines can be fitted with  $B_1^\beta = 2.7351 \text{ cm}^{-1}$  but the value  $B_1 = 2.7345 \text{ cm}^{-1}$  is somewhat better. However, a few of the lines, among which is the strong line at  $1060.9 \text{ cm}^{-1}$  (Fig. 5), do not form a regular series with the other lines.

The individual lines of the  $Q$  branch were not resolved. However, a simple calculation shows that the small extent of the band is consistent with the upper state  $B$  value equal to  $2.6894\text{ cm}^{-1}$ ; the branch should therefore be designated  $Q^\alpha$ .

The constants obtained here for the  $\nu_2$  band do not differ greatly from those obtained from lower dispersion spectrograms by Shepherd and Welsh (1957), but they have a lower probable error. It should be noted that high members of the  $R$  branch,  $J = 30$  to  $J = 38$ , which seemed to be present in the low dispersion spectrograms, were not observed in the present investigation and are believed to be spurious.

For comparison with the observed Raman frequencies Table I also gives calculated frequencies obtained from the constants determined from the above analysis. Except for some of the  $P$  lines the discrepancies are on the average less than  $0.1\text{ cm}^{-1}$ .

### *The Infrared Spectrum*

The infrared  $\nu_2$  band has been examined at high dispersion by Kaylor and Nielsen (1955). Since the band derives its intensity only through Coriolis interaction with  $\nu_4$  it is comparatively weak. The low frequency side is overlapped by the high frequency side of the strong  $\nu_4$  band; however, on the high frequency side of the band origin a good deal of regularity is evident in the rotational structure. Figure 4 is a recorder trace of the band copied from Kaylor and Nielsen (1955). An outstanding feature of the spectrum is a series of triplet lines going to higher frequencies from the band origin. With the constants obtained above from the Raman spectrum the two stronger members of the triplets can be assigned immediately to  $Q^\beta$  and  $Q^\gamma$  lines. The third and weakest members of the triplets form an additional  $Q$  branch with a somewhat lower  $B_1$  value; this will be designated  $Q^\delta$ . An analysis using the  $B_0$  and  $D_0$  values from the Raman spectrum and the infrared frequencies as measured by Kaylor (1954) gave  $B_1^\beta = 2.7338 \pm 0.0008$ ,  $D_1^\beta = (9.2 \pm 0.4) \times 10^{-5}$ ,  $B_1^\gamma = 2.7427 \pm 0.0007$ ,  $D_1^\gamma = (11.6 \pm 0.5) \times 10^{-5}$ ,  $B_1^\delta = 2.7303 \pm 0.0007$ , and  $D_1^\delta = (8.7 \pm 0.3) \times 10^{-5}\text{ cm}^{-1}$ ; the least squares lines obtained in the analysis are shown in Fig. 5. The  $B_1^\beta$  and  $B_1^\gamma$  values agree very well with the Raman values. There is some evidence that a  $Q^\alpha$  branch is also present in the infrared spectrum.

The triplet series of  $Q$  branches obscures the  $R$  lines of the infrared spectrum up to about  $J = 6$ . Most of the higher frequency lines of the band can be assigned to  $R^\alpha$ ,  $R^\beta$ ,  $R^\gamma$ , and  $R^\delta$  series. Of these four branches  $R^\alpha$  is the strongest and an analysis of this series, using the Raman ground state constants, gave  $B_1^\alpha = 2.6902 \pm 0.0008$  and  $D_1^\alpha = (10.9 \pm 0.3) \times 10^{-5}$ ; the least squares line is shown in Fig. 5. Again, the agreement with the Raman values is very satisfactory.

The assignments for the infrared band are shown in Fig. 4. A number of lines in the  $R$  branch remain unassigned and some of these coincide with unassigned Raman lines (Fig. 1); it is probable that these are due to perturbation of certain rotational levels. The  $P$  branches of both the infrared and the Raman band are apparently so confused by perturbations that assignments to sublevels is practically impossible; the infrared band is also overlapped by the

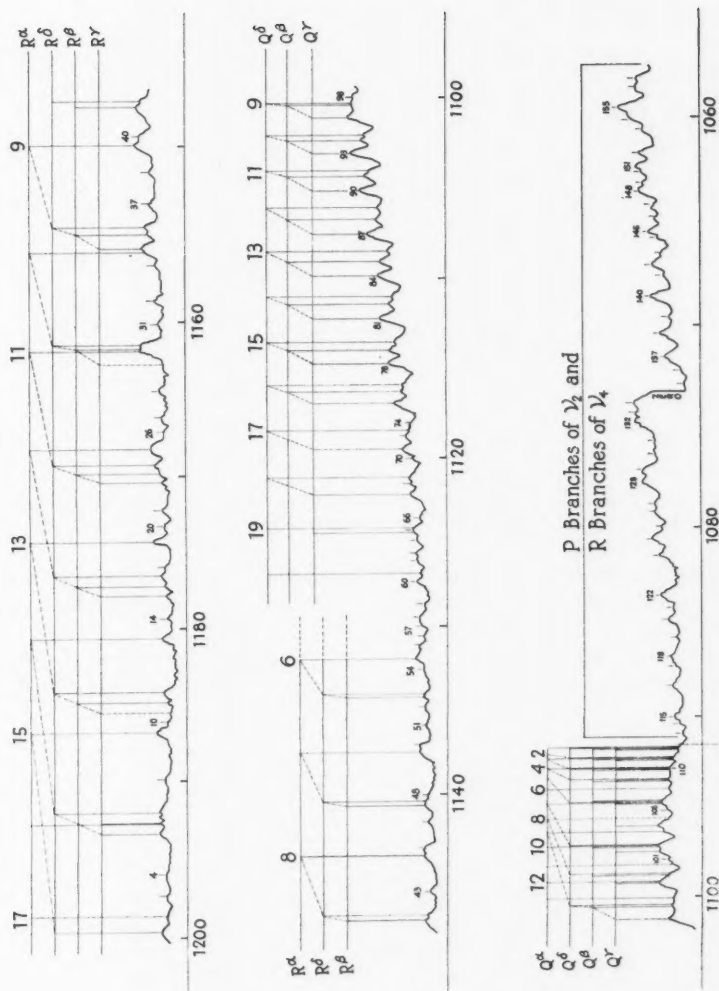


FIG. 4. The  $\nu_2$  infrared band of  $CD_4$  after Kaylor and Nielsen (1955) with assignments based on the analysis of the  $\nu_2$  Raman band.

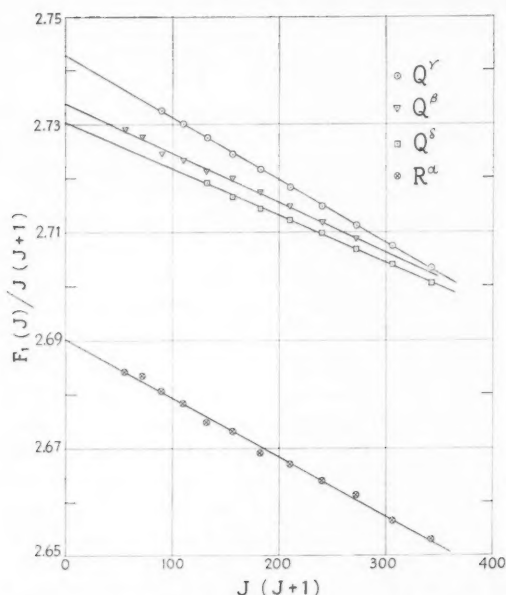


FIG. 5. Determination of upper state rotational constants of the  $Q^\beta$ ,  $Q^\gamma$ ,  $Q^\delta$ , and  $R^\alpha$  lines of the  $\nu_2$  infrared band using ground state constants obtained from the Raman spectrum.

higher frequency lines of the  $\nu_4$  band. The analysis of the infrared band on the basis of the Raman results differs greatly from that given by Kaylor and Nielsen (1955) and for that reason is given in detail here.

The essential constants obtained from the analyses of the Raman and infrared  $\nu_2$  bands are summarized in Table II. It will be noted that  $B_1 - B_0$

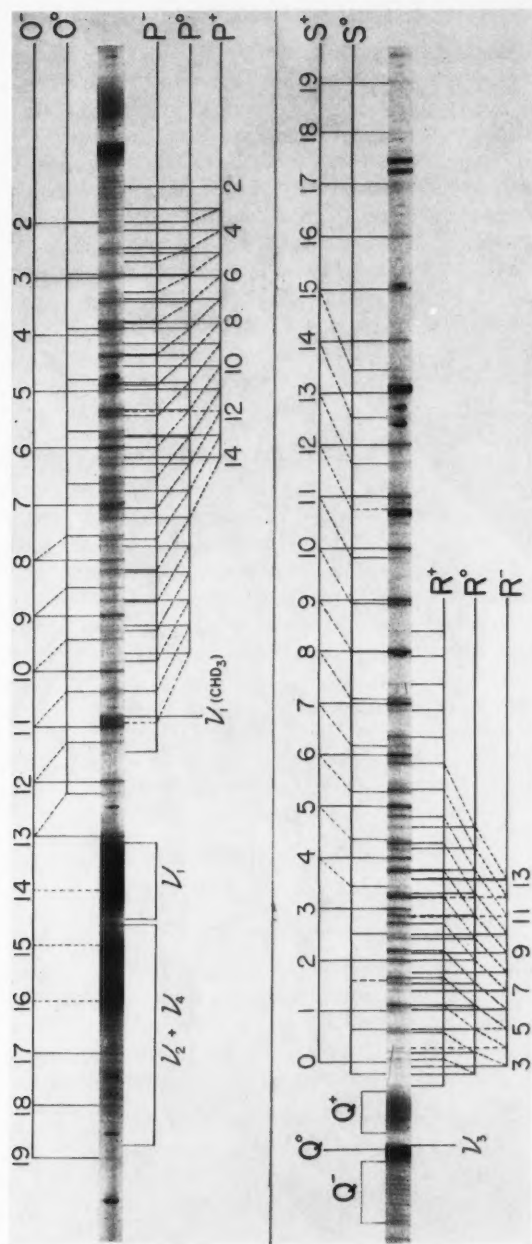
TABLE II  
Constants of the  $\nu_2$  band of  $\text{CD}_4$

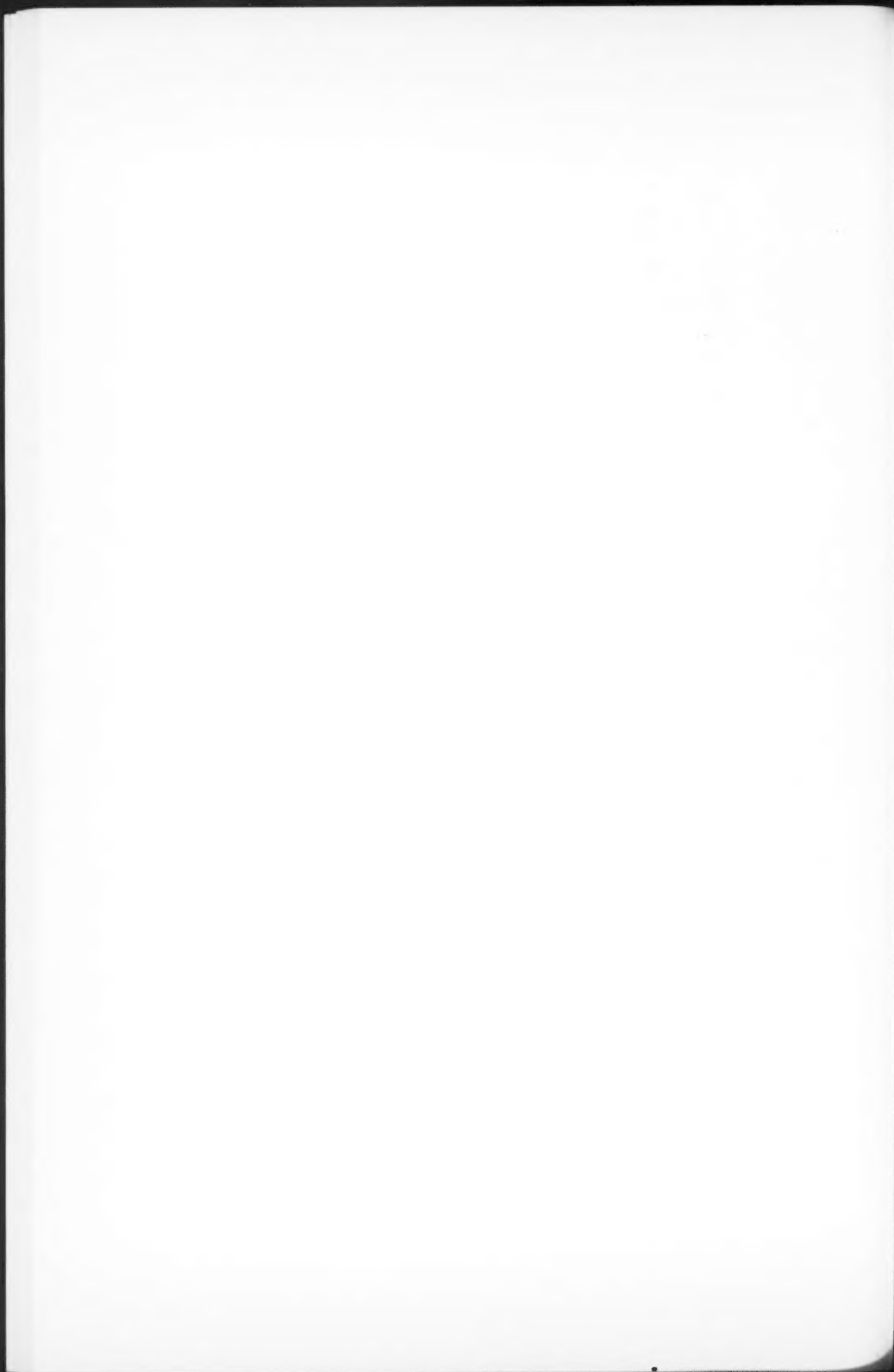
	Raman ( $\text{cm}^{-1}$ )	Infrared* ( $\text{cm}^{-1}$ )
$\nu_0$	$1091.93 \pm 0.03$	—
$B_0$	$2.6330 \pm 0.0007$	—
$B_1^\alpha$	$2.6894 \pm 0.0008$	$2.6902 \pm 0.0008$
$B_1^\beta$	$2.7351 \pm 0.0007$	$2.7338 \pm 0.0008$
$B_1^\gamma$	$2.7434 \pm 0.0007$	$2.7427 \pm 0.0007$
$B_1^\delta$	—	$2.7303 \pm 0.0007$

\*The Raman value of  $B_0$  is assumed.

is positive and comparatively large; the relative enhancement of  $B_1$ , which can be expressed as  $100(B_1 - B_0)/B_0$ , varies from 2% to 4% for the various  $B_1$  values. The enhancement of the  $B_1$  value of the  $\nu_2$  vibration is undoubtedly







a consequence of the Coriolis interaction with  $\nu_4$  which lies at a lower frequency ( $\nu_4 = 995.6 \text{ cm}^{-1}$  according to Kaylor and Nielsen); the  $B_1$  value of  $\nu_4$  would be correspondingly depressed.

It is interesting to compare the structure and constants of the  $\nu_2$  Raman band of  $\text{CH}_4$  with those of  $\text{CD}_4$ . Ordinary methane shows  $O^\beta$ ,  $P^\alpha$ ,  $Q^\alpha$ ,  $R^\alpha$ , and  $S^\beta$  branches with a few weak lines of a  $P^\beta$  branch (Thomas and Welsh 1960); heavy methane shows  $O^\beta$ ,  $P^\beta$ ,  $Q^\alpha$ ,  $R^\alpha$ , and  $S^\beta$  branches accompanied by weaker  $O^\alpha$  and  $S^\gamma$  branches. The relative enhancement of the  $B_1$  values,  $100(B_1 - B_0)/B_0$ , is 1% to 2% in  $\text{CH}_4$  as compared with 2% to 4% in  $\text{CD}_4$ , and the relative perturbation of the  $B_1$  values,  $100(B_1^\beta - B_1^\alpha)/B$ , is 1.2% in  $\text{CH}_4$  and 1.7% in  $\text{CD}_4$ . The smaller perturbation of the  $\nu_2$  band in  $\text{CH}_4$  is evidently due to the greater separation of the  $v = 1$  states of the  $\nu_2$  and  $\nu_4$  vibrations in this molecule ( $\nu_2 = 1533.6$ ,  $\nu_4 = 1306.2 \text{ cm}^{-1}$ ).

#### THE $\nu_2$ BAND

##### *The Raman Spectrum*

Four spectrograms of the  $\nu_2$  band were obtained, two with Hg 4047 as the exciting line and exposure times of 12 and 64 hours and two with Hg 4358 as the exciting line and exposure times of 35 and 45 hours. The instrumental slit was  $0.3 \text{ cm}^{-1}$  in all cases. Since the band extends over  $550 \text{ cm}^{-1}$ , the large dispersion ( $3.5 \text{ cm}^{-1}/\text{mm}$ ) obtained with Hg 4358 as the exciting line necessitated photographing the band in two sections. A reproduction of one of the spectrograms is given in Fig. 6 and a microphotometer trace of the same spectrogram in Fig. 7. The 202 Raman lines measured in the  $1950\text{--}2500 \text{ cm}^{-1}$  region belong to the  $\nu_1$ ,  $2\nu_4$ ,  $\nu_2 + \nu_4$ , and  $\nu_3$  bands; the frequencies given in Table III are weighted averages from the four spectrograms.

The rotational levels of the upper vibrational state ( $F_2$  species) of the  $\nu_3$  band are split by the Coriolis interaction of the rotational and vibrational motions into three sublevels given by:

$$\begin{aligned} F_1^+(J) &= B_1J(J+1) + 2B_1\zeta(J+1) - D_1J^2(J+1)^2, \\ (5) \quad F_1^0(J) &= B_1J(J+1) - D_1J^2(J+1)^2, \\ F_1^-(J) &= B_1J(J+1) - 2B_1\zeta J - D_1J^2(J+1)^2, \end{aligned}$$

where  $\zeta$  is the vibrational angular momentum constant of the  $v = 1$  state (Teller 1934). Transitions are allowed to all three sublevels in Raman scattering; the selection rule,  $\Delta J = 0, \pm 1, \pm 2$ ,  $J' + J'' \geq 2$ , thus gives 15 branches in the rotational structure of the Raman band. The relative intensities of the various branches for large  $J$  values as given by Teller are:

$$\begin{aligned} (6) \quad S^+ : S^0 : S^- &= O^- : O^0 : O^+ = 15 : 5 : 1, \\ R^+ : R^0 : R^- &= P^- : P^0 : P^+ = 10 : 8 : 3, \\ Q^+ : Q^0 : Q^- &= 6 : 9 : 6. \end{aligned}$$

These relations are useful in the assignment of the lines to the different branches.

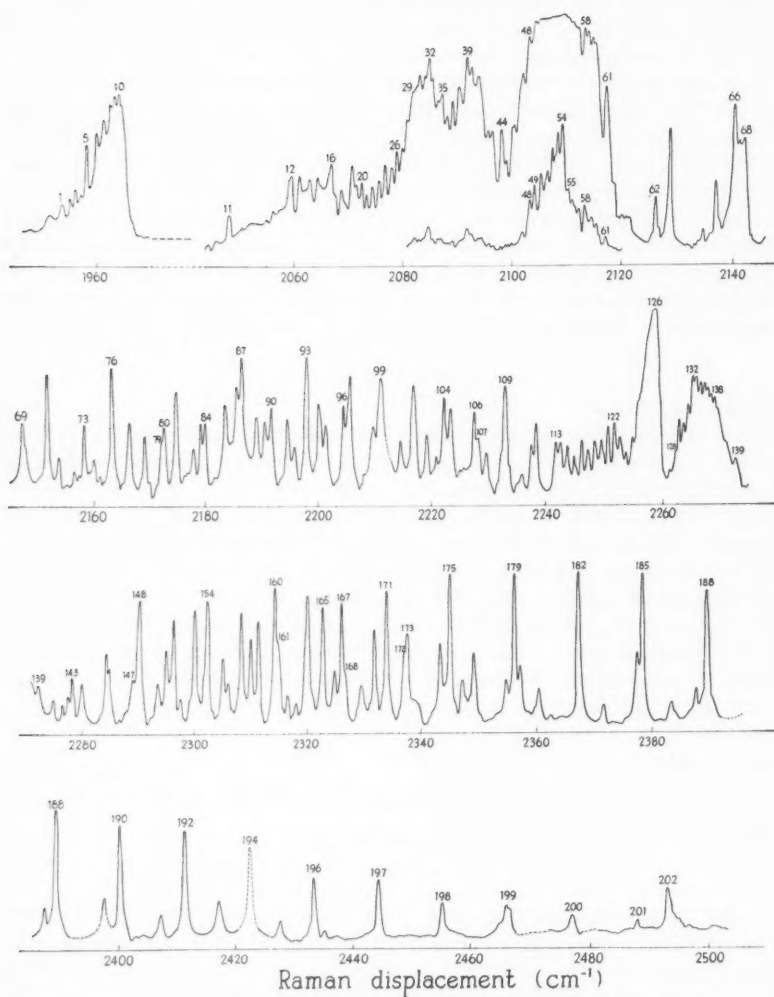


FIG. 7. Microphotometer trace of the spectrogram in Fig. 6, showing the 1950–2500  $\text{cm}^{-1}$  region of the Raman spectrum of  $\text{CD}_4$ . The portion from 2080 to 2120  $\text{cm}^{-1}$  is also shown with a greatly reduced exposure time.

As discussed below most of the lower frequency lines (No. 1–60 in Fig. 7) belong to the  $\nu_1$ ,  $2\nu_4$ , and  $\nu_2 + \nu_4$  transitions; the remaining lines could be assigned to the rotational structure of the  $\nu_3$  band. Evidence for 13 of the 15 branches of the latter was obtained; no lines of the very weak  $O^+$  and  $S^-$  series could be identified.

TABLE III  
 Raman frequencies of the  $\nu_3$  band of CD<sub>4</sub>

Line No.	$\Delta\nu(\text{cm}^{-1})$	Assignment	Line No.	$\Delta\nu(\text{cm}^{-1})$	Assignment
1	1953.2		62	2125.9	$O^0(13)$
2	1954.8		63	2128.5 <sup>a</sup>	$O^-(12)$
3	1955.9		64	2134.6	$P^-(20)$
4	1957.1		65	2136.7	$O^0(12)$
5	1958.2		66	2140.1 <sup>a</sup>	$O^-(11)$
6	1960.0		67	2141.1	$P^-(19)$
7	1961.4		68	2142.0	$\nu_1, Q_{\text{max}}(\text{CHD}_3)$
8	1962.5		69	2147.4 <sup>a</sup>	$O^0(11)$
9	1963.3		70	2151.7 <sup>a</sup>	$O^-(10)$
10	1964.1		71	2153.6	$P^-(17)$
11	2047.6 <sup>a</sup>	$O^-(19)$	72	2156.4	$P^0(19)$
12	2059.2 <sup>a</sup>	$O^-(18)$	73	2158.2 <sup>a</sup>	$O^0(10)$
13	2060.8		74	2160.0	$P^-(16)$
14	2062.8		75	2162.0	$P^0(18)$
15	2064.2		76	2163.1 <sup>a</sup>	$O^-(9)$
16	2066.7		77	2166.3	$P^-(15)$
17	2068.5		78	2168.9 <sup>a</sup>	$O^0(9)$
18	2070.6 <sup>a</sup>	$O^-(17)$	79	2172.1	$P^0(16)$
19	2071.3		80	2172.5	$P^-(14)$
20	2072.4		81	2174.7 <sup>a</sup>	$O^-(8)$
21	2073.2		82	2177.7	$P^0(15)$
22	2074.4		83	2179.0	$P^-(13)$
23	2075.5		84	2179.6 <sup>a</sup>	$O^0(8)$
24	2076.6		85	2183.3	$P^0(14)$
25	2077.8		86	2185.3	$P^-(12)$
26	2078.7		87	2186.2 <sup>a</sup>	$O^-(7)$
27	2079.7		88	2188.9	$P^0(13)$
28	2080.7		89	2190.4 <sup>a</sup>	$O^0(7)$
29	2081.6		90	2191.6	$P^-(11)$
30	2082.9		91	2194.3	$P^0(12)$
31	2083.8		92	2195.7	$P^+(14)$
32	2084.7		93	2197.8 <sup>a</sup>	$O^-(6), P^-(10)$
33	2085.3		94	2200.0	$P^0(11)$
34	2086.3		95	2201.1 <sup>a</sup>	$O^0(6)$
35	2087.0		96	2204.2	$P^-(9)$
36	2087.9		97	2205.4	$P^0(10)$
37	2088.9		98	2209.3 <sup>a</sup>	$O^-(5), P^+(11)$
38	2090.1		99	2210.7	$P^-(8), P^0(9)$
39	2091.6		—	2211.6	$O^0(5)$
40	2092.4		100	2214.3	$P^+(10)$
41	2093.7		101	2216.5	$P^-(7), P^0(8)$
42	2095.4		102	2218.8	$P^+(9)$
43	2096.2		103	2220.5 <sup>a</sup>	$O^-(4)$
44	2098.0		104	2222.0	$P^0(7)$
45	2098.8		105	2223.2	$P^+(8), P^-(6)$
46	2100.1		106	2227.3	$P^0(6)$
47	2101.8		107	2228.0	$P^+(7)$
48	2102.8		108	2229.3	$P^-(5)$
49	2103.8		109	2232.6	$P^+(6), P^0(5)$
50	2105.0		110	2235.5	$P^-(4)$
51	2106.3		111	2237.1	$P^+(5)$
52	2107.1		112	2238.1	$P^0(4)$
53	2108.1		113	2241.5	$P^+(4)$
54	2108.9		114	2242.3	$O^-(16)$
55	2110.1		115	2243.5	$P^0(3), O^-(15)$
56	2110.8		116	2244.5	$O^-(14)$
57	2111.8		117	2246.1	$P^+(3), O^-(13)$
58	2113.0		118	2247.0	$O^-(12)$
59	2114.2		119	2248.2	$O^-(11)$
60	2115.1		120	2249.2	$O^-(10)$
61	2116.9 <sup>a</sup>	$O^-(13)$	121	2250.4	$O^-(9)$

TABLE III (Concluded)

Line No.	$\Delta\nu(\text{cm}^{-1})$	Assignment	Line No.	$\Delta\nu(\text{cm}^{-1})$	Assignment
122	2251.5	$O^-(8)$	163	2317.9	$R^-(13)$
123	2252.5	$O^-(7)$	164	2320.0	$R^+(9), R^0(11)$
124	2253.5	$O^-(6)$	165	2322.7 <sup>a</sup>	$S^+(4)$
125	2254.7	$O^-(5)$	166	2324.6	$R^0(12)$
126	2258.5	$O^0_{\text{max}}$	167	2325.9	$R^+(10)$
127	2261.1	$O^+(1)$	168	2326.5 <sup>a</sup>	$S^0(5)$
128	2262.0	$O^+(2)$	169	2329.4	$R^0(13)$
129	2262.6	$O^+(3)$	170	2331.6	$R^+(11)$
130	2263.4	$O^+(4)$	171	2333.8 <sup>a</sup>	$S^+(5)$
131	2264.2	$O^+(5)$	172	2336.9 <sup>a</sup>	$S^0(6)$
132	2264.9	$O^+(6)$	173	2337.4	$R^+(12)$
133	2265.6	$O^+(7)$	174	2343.2	$R^+(13)$
134	2266.3	$O^+(8)$	175	2345.0 <sup>a</sup>	$S^+(6)$
135	2266.9	$O^+(9)$	176	2347.1 <sup>a</sup>	$S^0(7)$
136	2267.5	$O^+(10)$	177	2349.0	$R^+(14)$
137	2268.1	$O^+(11)$	178	2354.7	$R^+(15)$
138	2268.7	$O^+(12)$	179	2356.1 <sup>a</sup>	$S^+(7)$
139	2272.3	$R^+(1)$	180	2357.1 <sup>a</sup>	$S^0(8)$
140	2274.9	$R^0(2)$	181	2360.3	$R^+(16)$
141	2276.5	$R^-(3)$	182	2367.2 <sup>a</sup>	$S^+(8), S^0(9)$
142	2277.6	$S^+(0)$	183	2371.5	$R^+(18)$
143	2278.4	$R^+(2)$	184	2377.3 <sup>a</sup>	$S^0(10)$
144	2280.0	$R^0(3)$	185	2378.3 <sup>a</sup>	$S^+(9)$
145	2284.4	$R^+(3)$	186	2383.2	$R^+(20)$
146	2285.0	$R^0(4)$	187	2387.2 <sup>a</sup>	$S^0(11)$
147	2289.2 <sup>a</sup>	$S^+(1), R^-(6)$	188	2389.3 <sup>a</sup>	$S^+(10)$
148	2290.4	$R^+(4), R^0(5)$	189	2397.2 <sup>a</sup>	$S^0(12)$
149	2293.5	$R^-(7)$	190	2400.3 <sup>a</sup>	$S^+(11)$
150	2295.1	$R^0(6)$	191	2407.0 <sup>a</sup>	$S^0(13)$
151	2296.3	$R^+(5)$	192	2411.2 <sup>a</sup>	$S^+(12)$
152	2297.6	$R^-(8)$	193	2416.9 <sup>a</sup>	$S^0(14)$
153	2300.2 <sup>a</sup>	$S^+(2), R^0(7)$	194	2422.1 <sup>a</sup>	$S^+(13)$
154	2302.4	$R^+(6)$	195	2427.3	$S^0(15)$
155	2305.1	$R^0(8)$	196	2433.0 <sup>a</sup>	$S^+(14)$
156	2306.0	$S^0(3)$	197	2443.8 <sup>a</sup>	$S^+(15)$
157	2308.3	$R^+(7)$	198	2454.7 <sup>a</sup>	$S^+(16)$
158	2310.0	$R^0(9)$	199	2465.5	$S^+(17)$
159	2311.4 <sup>a</sup>	$S^+(3)$	200	2476.4	$S^+(18)$
160	2314.2	$R^+(8)$	201	2486.9	$S^+(19)$
161	2314.8	$R^0(10)$	202	2491.9	—
162	2316.4 <sup>a</sup>	$S^0(4)$			

<sup>a</sup>Lines used in the determination of  $\nu_0$ ,  $B_0$ , and  $\zeta$ .

The  $O$  and  $S$  branches of the  $\nu_3$  band are particularly suited for the determination of the molecular constants since they cover a large frequency range. The  $O^0$  and  $S^0$  branches terminate in rotational states independent of  $\zeta$ , and can therefore be used for obtaining the ground state constants; the  $O^-$  and  $S^+$  branches, on the other hand, are best suited for an accurate determination of  $\zeta$ .

The  $O^0$  and  $S^0$  frequencies can be represented by equation (2) and an analysis similar to that for the  $\nu_2$  band was carried out. The values of the constants obtained from a least squares analysis of 18  $O^0$  and  $S^0$  lines (designated in Table III by the superscript  $a$ ) are:

$$\nu_0 = 2259.26 \pm 0.04 \text{ cm}^{-1},$$

$$B_0 = 2.6328 \pm 0.0007 \text{ cm}^{-1},$$

$$B_1 = 2.6144 \pm 0.0007 \text{ cm}^{-1},$$

$$D_0 = (3.8 \pm 0.3) \times 10^{-5} \text{ cm}^{-1},$$

$$D_1 = (3.1 \pm 0.3) \times 10^{-5} \text{ cm}^{-1}.$$

The value of  $B_0$  found here agrees with the value,  $2.6330 \pm 0.0007 \text{ cm}^{-1}$ , obtained from the  $\nu_2$  band well within the probable errors.

The  $O^-$  and  $S^+$  lines can be represented by the polynomial of equation (2) with coefficients given by:

$$a = \nu_0 + (3/4)(B_1 - B_0) + 3B_{1\zeta} - (9/16)(D_1 - D_0),$$

$$b = (B_1 + B_0) + B_{1\zeta} - (3/2)(D_1 + D_0),$$

$$c = (1/4)(B_1 - B_0) - (11/8)(D_1 - D_0),$$

$$d = (1/2)(D_1 + D_0),$$

$$e = (1/16)(D_1 - D_0).$$

A least squares analysis gave the following values for the coefficients:

$$a = 2260.63 \pm 0.02,$$

$$b = 5.6832 \pm 0.0011,$$

$$c = 0.00356 \pm 0.00010,$$

$$d = (2.71 \pm 0.12) \times 10^{-5},$$

$$e = (0.042 \pm 0.0078) \times 10^{-5}.$$

Since the five coefficients involve six molecular constants, the value  $B_0 = 2.6330 \text{ cm}^{-1}$  was assumed in determining the other five:

$$\nu_0 = 2259.33 \pm 0.02 \text{ cm}^{-1},$$

$$B_1 = 2.6187 \pm 0.0007 \text{ cm}^{-1},$$

$$B_{1\zeta} = 0.4316 \pm 0.0013 \text{ cm}^{-1},$$

$$D_0 = (3.05 \pm 0.1) \times 10^{-5} \text{ cm}^{-1},$$

$$D_1 = (2.4 \pm 0.1) \times 10^{-5} \text{ cm}^{-1}.$$

From  $B_1$  and  $B_{1\zeta}$  the value,  $\zeta = 0.1648 \pm 0.0006$ , is obtained. It will be noted that  $B_1$  for the  $O^-$  and  $S^+$  branches is significantly different from that for the  $O^0$  and  $S^0$  branches.

In the further analysis the following values of the ground state constants were assumed:  $B_0 = 2.6330$ ,  $D_0 = 3.4 \times 10^{-5} \text{ cm}^{-1}$ . It was also assumed that  $\nu_0 = 2259.30 \text{ cm}^{-1}$  and  $\zeta = 0.1648$ .

All six of the  $P$  and  $R$  branches were observed. The rotational terms of the upper vibrational state,  $F_1(J)$ , were evaluated for each of the branches from the observed frequencies and the constants given in the last paragraph. For the  $R^+$  and the  $P^-$  lines equation (4) becomes

$$(7) \quad \frac{F_1^+(J) - 2B_{1\zeta}(J+1)}{J(J+1)} = B_1 - D_1J(J+1)$$

and

$$\frac{F_1^-(J) + 2B_{1\zeta}J}{J(J+1)} = B_1 - D_1J(J+1),$$

respectively. A plot of the left-hand side of these equations against  $J(J+1)$



for the  $P^-$  and  $R^+$  lines is shown in Fig. 8; it is clear that the two branches form a single series. A least squares analysis of the points in Fig. 8 gave  $B_1 = 2.6205 \pm 0.0009$  and  $D_1 = (2.9 \pm 0.4) \times 10^{-5}$ .

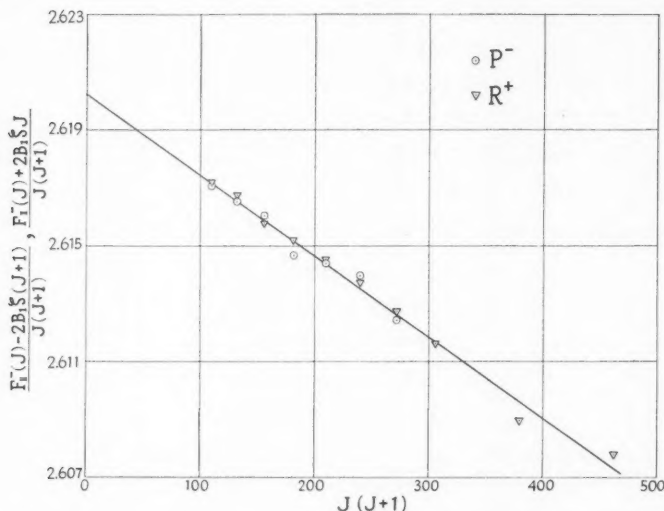


FIG. 8. Determination of the upper state rotational constants of the  $P^-$  and  $R^+$  branches of the  $\nu_3$  band.

The data for the weak  $P^+$  and  $R^-$  branches are more fragmentary. However, the plot for relations analogous to equations (7) shows that the two branches probably form a single series (Fig. 9). A least squares analysis gave  $B_1 = 2.6199 \pm 0.0010$ ,  $D_1 = (3.1 \pm 0.5) \times 10^{-5} \text{ cm}^{-1}$ .

The upper state rotational energies of the  $P^0$  and  $R^0$  lines should follow equation (3) and an analysis by equation (4) should be possible. Figure 10 shows the plot of  $F_1(J)/J(J+1)$  against  $J(J+1)$ . In spite of the considerable scatter of the points for low  $J$  values it is evident that the two branches require different  $B_1$  values. The  $P^0$  lines require  $B_1 = 2.6187 \pm 0.0009$ , as for the  $O^-$  and  $S^+$  branches, and  $D_1 = (3.6 \pm 0.4) \times 10^{-5}$ ; the  $R^0$  branch requires, on the other hand,  $B_1 = 2.6152 \pm 0.0009$ , which is nearly equal to that for the  $O^0$  and  $S^0$  branches, and  $D_1 = (2.3 \pm 0.4) \times 10^{-5}$ .

The three  $Q$  branches expected in the Raman spectrum are easily identified near the band region in Figs. 6 and 7. Equations (5) give the following formulae for the  $Q$  branch frequencies:

$$\begin{aligned}\Delta\nu_Q^+ &= \nu_0 + (B_1 - B_0)J(J+1) + 2B_1J(J+1) - (D_1 - D_0)J^2(J+1)^2, \\ \Delta\nu_Q^0 &= \nu_0 + (B_1 - B_0)J(J+1) - (D_1 - D_0)J^2(J+1)^2, \\ \Delta\nu_Q^- &= \nu_0 + (B_1 - B_0)J(J+1) - 2B_1J(J+1) - (D_1 - D_0)J^2(J+1)^2.\end{aligned}$$

Since  $B_1 - B_0$  is negative and  $2B_1J$  is positive, it is clear that the  $Q^+$  branch will tend to form a band head at a frequency higher than  $\nu_0$  and the  $Q^-$  branch will

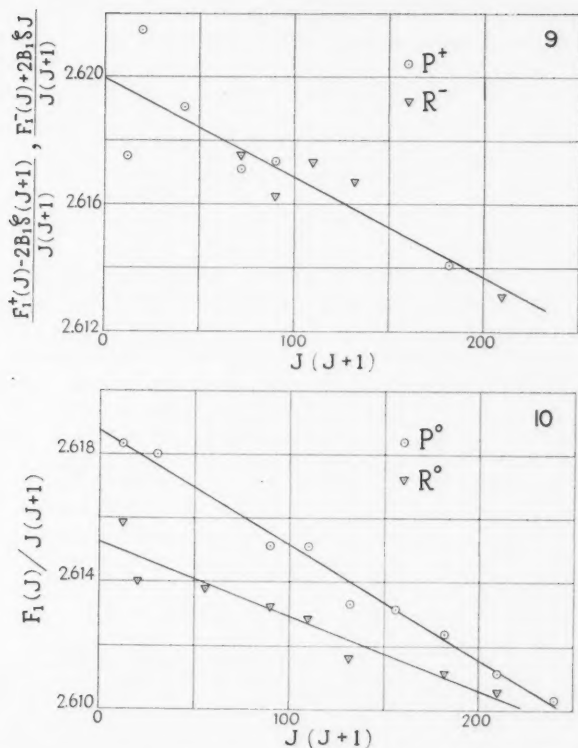


FIG. 9. Determination of the upper state rotational constants of the  $P^+$  and  $R^-$  branches of the  $\nu_3$  band.

FIG. 10. Determination of the upper state rotational constants of the  $P^0$  and  $R^0$  branches of the  $\nu_3$  band.

diverge towards lower frequencies (Fig. 6). The  $Q^0$  branch must undoubtedly be identified with the broad unresolved maximum on the low frequency side of  $\nu_0$ .

The assignments given in Table III for the  $Q^+$  and  $Q^-$  lines are based on calculations from equations (8) with  $B_1 = 2.6187 \text{ cm}^{-1}$ ; the agreement of the calculated with the observed frequencies is very satisfactory. Since the  $Q^0$  branch shows no structure the  $B_1$  value associated with it cannot be determined; however, the extent of the branch is compatible with  $B_1 = 2.6144 \text{ cm}^{-1}$  as for the  $O^0$  and  $S^0$  branches.

A summary of the  $B$  values obtained from the analysis of the  $\nu_3$  Raman band is given in Table IV. Like the  $\nu_3$  band of  $\text{CH}_4$ , the  $\nu_3$  band of  $\text{CD}_4$  requires a multiplicity of  $B_1$  values to reproduce its structure. In both molecules the  $O^0$ ,  $S^0$ ,  $R^0$  branches require a considerably lower  $B_1$  value than the other branches; the difference between the three  $B_1$  values for the other branches are hardly significant from the statistical point of view.

TABLE IV  
Summary of the  $B_1$  values for the  $\nu_3$  Raman  
band of  $\text{CD}_4$

Branch	$B_1(\text{cm}^{-1})$
$O^0, S^0, R^0$	$2.6144 \pm 0.0007$
$O^-, S^+, Q^-, Q^0, Q^+, P^0$	$2.6187 \pm 0.0007$
$P^+, R^-$	$2.6199 \pm 0.0010$
$P^-, R^+$	$2.6205 \pm 0.0008$

### The Infrared Spectrum

According to the selection rules the infrared band should show three branches  $P^+$ ,  $Q^0$ , and  $R^-$ . The infrared spectrum, recorded at high dispersion by Kaylor and Nielsen (1955), showed strong  $P$  and  $R$  branches and an unresolved  $Q$  branch; numerous weak lines were also observed in the band. The analysis of the infrared band alone cannot be used to determine the four constants,  $\nu_0$ ,  $B_0$ ,  $B_1$ ,  $\xi_3$ ; Kaylor and Nielsen therefore adopted the procedure of analyzing simultaneously the  $\nu_3$  and  $\nu_4$  bands and evoking the  $\xi$ -sum rule, which in this case is  $\xi_3 + \xi_4 = 1/2$ . Their results for the  $\nu_3$  band were as follows:

$$\nu_0 = 2259.3 \text{ cm}^{-1},$$

$$B_0 = 2.591 \text{ cm}^{-1},$$

$$B_1 = 2.577 \text{ cm}^{-1},$$

$$\xi_3 = 0.1452.$$

Except for  $\nu_0$  these values show large deviations from the values obtained above from the Raman spectrum. The discrepancy is undoubtedly due to the neglect of centrifugal stretching constants in the infrared analysis and the use of the  $\xi$ -sum rule which holds strictly only for harmonic vibrations. However, the infrared frequencies were very accurately measured by Kaylor (1954), and it is worth while to use them to check the analysis of the Raman band.

The infrared  $P^+$  and  $R^-$  frequencies should of course be the same as the Raman  $P^+$  and  $R^-$  frequencies. Although these are weakest of the Raman  $P$  and  $R$  branches, 16 members were observed (Table III). A comparison showed a gratifying agreement between the measured infrared and Raman frequencies; the mean difference was about  $0.1 \text{ cm}^{-1}$ , the infrared frequencies being in almost all cases higher than the Raman frequencies.

For the  $P^+$  and  $R^-$  lines the fourth degree polynomial of equation 2 has coefficients as follows:

$$a = \nu_0,$$

$$b = B_1 + B_0 - 2B_1\xi,$$

$$c = B_1 - B_0 - (D_1 - D_2),$$

$$d = 2(D_1 + D_2),$$

$$e = D_1 - D_0.$$

Since the six constants involved cannot be determined from the five coefficients, it is necessary to take over the Raman value of one of the constants; the value  $B_0 = 2.6330 \text{ cm}^{-1}$  was therefore used. The coefficients obtained from a least squares analysis of 32 infrared frequencies then gave the following:

$$\nu_0 = 2259.25 \pm 0.01 \text{ cm}^{-1},$$

$$B_1 = 2.6209 \pm 0.0007 \text{ cm}^{-1},$$

$$\xi = 0.1657 \pm 0.0003,$$

$$D_0 = (2.5 \pm 0.2) \times 10^{-5} \text{ cm}^{-1},$$

$$D_1 = (2.4 \pm 0.2) \times 10^{-5} \text{ cm}^{-1}.$$

These show a satisfactory agreement with the Raman values.

#### THE $\nu_1$ , $2\nu_4$ , AND $\nu_2 + \nu_4$ BANDS

The region of Raman shifts from 1950 to 2120  $\text{cm}^{-1}$  contains several structures which do not belong to the  $\nu_3$  band (Figs. 6 and 7). The C—D stretching frequency should occur in this region and, following Shepherd and Welsh (1957), we associate it with the strong band with a maximum at 2108.9  $\text{cm}^{-1}$ . The group of lines with a maximum at 1964.1  $\text{cm}^{-1}$  has a shape similar to the  $Q$  branch of  $\nu_1$  and can be assigned with certainty to  $2\nu_4$  in Fermi resonance with  $\nu_1$ ; the maximum frequency is somewhat lower, as might be expected, than the value 1991.2  $\text{cm}^{-1}$  calculated from  $\nu_4 = 995.6 \text{ cm}^{-1}$  as determined by Kaylor and Nielsen (1955). The group of lines between 2040 and 2100  $\text{cm}^{-1}$  should undoubtedly be assigned to  $\nu_2 + \nu_4$  as suggested previously by Shepherd and Welsh (1957). The band possesses three maxima and resembles in a general way the  $Q$  branch of the  $\nu_3$  band with its three subbranches  $Q^-$ ,  $Q^0$ , and  $Q^+$ ; it probably occurs therefore as a result of Fermi resonance or Coriolis interaction with  $\nu_3$ . The appearance of this band is very interesting since it is of a type not previously observed in Raman spectra of gases.

Each of the bands  $\nu_1$ ,  $2\nu_4$ , and  $\nu_2 + \nu_4$  shows considerable rotational structure which has not yet proved tractable to analysis; the band origins can thus not be accurately determined. The  $\nu_1$  band has a rather perplexing structure. The main part of the intensity is degraded towards lower frequency shifts and one is inclined to place the band origin near 2110.1  $\text{cm}^{-1}$  (line 55 in Fig. 7); however, this would leave the structure at higher frequencies (lines 55–61 in Fig. 7) unaccounted for. It seems more probable that the origin is near 2117  $\text{cm}^{-1}$  (line 61), and that either the lower members of the  $Q$  branch are strongly perturbed or there is an underlying structure belonging to another band, possibly  $(\nu_2 + \nu_4)(F_1)$ . If the interpretation given above for the main  $\nu_2 + \nu_4$  band is correct, its origin should be near 2088  $\text{cm}^{-1}$ ; the value of  $\nu_2 + \nu_4$  calculated from the sum of the fundamental frequencies is 2087.5  $\text{cm}^{-1}$ .

The overtone  $2\nu_2$ , which is present in the spectrum of  $\text{CH}_4$  (Thomas and Welsh 1960), was not observed in the spectrum of  $\text{CD}_4$ .

## THE LENGTH OF THE C—D BOND

From the value,  $B_0 = 2.6330 \pm 0.0007 \text{ cm}^{-1}$ , it is possible to calculate  $r_0$  for the C—D bond in  $\text{CD}_4$ ;  $r_0$  is the effective bond length defined by  $(1/r_0^2) = \overline{(1/r^2)}$ , where the average is taken over the zero point motion of the molecule. Using the relations  $B_0 = h/8\pi^2 cI$  and  $I = (8/3)m_D r_0^2$  and values of the physical constants as given by Cohen, DuMond, Layton, and Rollett (1955) one finds  $r_0(\text{C—D})$  to be  $1.09181 \pm 0.00029 \text{ \AA}$ . The corresponding value for methane,  $r_0(\text{C—H})$ , is  $1.09403 \pm 0.00016 \text{ \AA}$  (Thomas and Welsh 1960).

The determination of the equilibrium bond lengths,  $r_e$ , from electron diffraction and spectroscopic data has been considered quite recently by Bartell, Kuchitsu, and deNeui (1960). By representing the potential energy of the molecule by a suitable modified Urey-Bradley field they calculated the values  $0.009_1$  and  $0.006_8 \text{ \AA}$  for  $r_0 - r_e$  in  $\text{CH}_4$  and  $\text{CD}_4$ , respectively. With the values of  $r_0$  obtained by Thomas and Welsh (1960) for  $\text{CH}_4$  and in the present investigation for  $\text{CD}_4$ , the values of  $r_e$  are thus  $1.084_9$  and  $1.085_0 \text{ \AA}$  for the C—H and C—D bonds, respectively. These values are the same within the probable error; they also show good agreement with the values obtained from electron diffraction measurements by Bartell, Kuchitsu, and deNeui (1960).

## ACKNOWLEDGMENT

The authors are indebted to Professor W. H. Watson, Director of the Computation Center, University of Toronto, for the use of computing facilities.

## REFERENCES

- BARTELL, L. S., KUCHITSU, K., and deNEUI, R. J. 1960. *J. Chem. Phys.* **33**, 1254.  
 COHEN, E. R., DuMOND, J. W. M., LAYTON, T. W., and ROLLETT, J. S. 1955. *Revs. Modern Phys.* **27**, 363.  
 KAYLOR, H. M. 1954. Ph.D. Thesis, University of Tennessee.  
 KAYLOR, H. M. and NIELSEN, A. H. 1955. *J. Chem. Phys.* **23**, 2139.  
 SHEPHERD, G. G. and WELSH, H. L. 1957. *J. Mol. Spectroscopy*, **1**, 277.  
 STOICHEFF, B. P., CUMMING, C. C., ST. JOHN, G. E., and WELSH, H. L. 1952. *J. Chem. Phys.* **20**, 498.  
 TELLER, E. 1934. *Hand-und Jahrbuch d. Chem. Physik*, **9**, II.  
 THOMAS, M. A. and WELSH, H. L. 1960. *Can. J. Phys.* **38**, 1291.

# ANALYSIS OF A TYPE OF ROUGH-TRAIL METEOR ECHO<sup>1</sup>

B. A. McINTOSH

## ABSTRACT

For a particular type of meteor echo, the variation of echo duration with atmospheric height is examined. Theory based on an initially rough meteor trail is substantiated by showing that atmospheric scale heights calculated from measurements on these echoes are in agreement with generally accepted values.

## INTRODUCTION

McNamara and McKinley (1959) have recently commented on the effect of trail irregularities on the interpretation of meteor echoes. They suggest that the initially smooth meteor trail may be the exception, and that irregularity and disorder may be the rule. The *b*-type echoes of the classification of McKinley and Millman (1949) are interesting examples of this disorder. It has been suggested by Rao and Armstrong (1958) and Rao and Millman (unpublished) that the characteristic time-decay contour of *b*-type echoes may be explained on the basis of the rough-trail hypothesis and the drift of two or more effective points of reflection. The purpose of this note is to examine in further detail, and from a slightly different viewpoint, the characteristics of *b*-type echoes.

Although not the primary object of this paper, it will be shown that, provided certain assumptions are satisfied, atmospheric scale height in the meteoric region may be determined from *b*-type echoes. Kaiser (1953) has calculated scale heights from measurements of the height distribution of meteors. It may be that *b*-type echoes will provide a new tool for this purpose.

## THE OBSERVATIONAL EVIDENCE

Three examples of *b*-type echoes as observed on the range-time display of a backscatter radar are shown in Fig. 1. The most prominent feature of these echoes is the complete absence of aspect sensitivity; the echo begins long before the meteor crosses the line-of-sight perpendicular to the trail. The typical leading edge curl may be associated with a head echo as in Figs. 1(a) and 1(c) or have none as in Fig. 1(b). Although not pertinent to this paper it is interesting to note that Fig. 1(a) appears to exhibit two head echoes. After the passage of the meteor the main body echo appears within a time that varies from zero to a few tenths of a second. The character of the echo is typically grainy or nebulous as in Fig. 1(a). If the echo persists for a sufficient length of time, the uniform graininess may be resolved into a number of discrete echoes at different ranges.

It is apparent from the character of these echoes that the meteor trail as

<sup>1</sup>Manuscript received November 9, 1960.

Contribution from the Division of Radio and Electrical Engineering, National Research Council, Ottawa, Canada.

Issued as N.R.C. No. 6176.

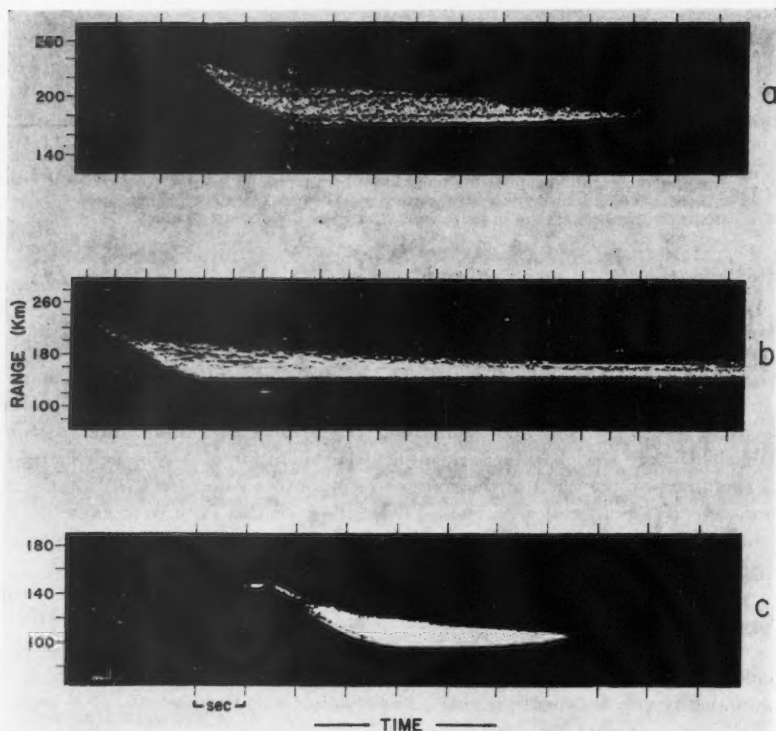


FIG. 1. Three examples of *b*-type echoes as observed on the range-time display of the Ottawa 9.2-meter radar.

initially formed is quite rough, consisting of a large number of scattering centers which, by interference of the reflected radio waves, produce the typical grainy character. As these patches of ionization expand, numbers of them may coalesce into larger, single reflecting centers, or it may be that linear arrays of the smaller patches or long continuous sections of the trail are turned by winds so as to produce stronger, essentially specular echoes. This results in the change from uniform graininess to a few solid echoes at discrete ranges that is characteristic of the later stages of *b*-type echoes.

It is unlikely that small-scale turbulence can account for the initial formation of the small scattering centers. In many cases the body echo begins immediately after the head echo, certainly within less than one-tenth of a second. It appears more likely that the mechanism for the formation of the rough trail is inherent in the meteoroid itself, although the assistance of unusual atmospheric conditions cannot be discounted entirely.

A prevalent view (Jacchia, Kopal, and Millman 1950; Öpik 1958; McKinley 1961) is that most visual meteors are of the "dustball" type rather than



compact stone or iron. These are low-density, loosely bound agglomerates of dust particles and frozen gases. In their passage through the atmosphere they undergo a process of progressive fragmentation and ablation of the individual dust particles. It is quite conceivable that this type of meteoroid could produce the rough trail necessary for *b*-type echoes. Although a detailed study of the statistics of *b*-type echoes has not been made, it may be said qualitatively that they represent a small fraction of the total number of echoes observed. However, if statistics are restricted to echoes of a certain minimum duration, say durations which put the meteor in the visible range, the proportion of *b*-type echoes is greatly increased. Further, for an echo to be recorded as a *b*-type, not only a rough trail is required, but also a favorable space geometry with regard to elongation of the trail from the radiant. The identification of *b*-type echoes with "dustball" type meteors is thus still somewhat tentative.

#### ANALYSIS OF THE ECHO DURATION VS. HEIGHT CHARACTERISTIC OF *b*-TYPE ECHOES

The analysis to be made is subject to the following assumptions:

1. The ionizing efficiency of the meteoroid is proportional to the luminous efficiency.

2. Whatever the cause of the rough trail and whatever the form of the blobs of ionization, be they essentially spherical or in the form of long cylinders, the ion density in the individual scattering centers is proportional to that which would be found at the same point along a smooth trail. This assumption is difficult to justify *a priori*, and certainly from the wide variety of irregular echo forms that do occur it is obviously not true in all cases.

3. Over all but an insignificant initial portion of the trail the ionization is overdense; that is, the blobs act like metallic reflectors rather than coherent electron scatterers.

4. The ionization is dissipated by diffusion only and the diffusion coefficient is inversely proportional to atmospheric density.

The production of ionization along a meteor trail is given by (Whipple 1943)

$$\frac{\alpha}{\alpha_{\max}} = \frac{9}{4} \frac{\rho}{\rho_{\max}} \left( 1 - \frac{1}{3} \frac{\rho}{\rho_{\max}} \right)^2$$

where  $\alpha$  is the electron line density at a height where the atmospheric density is  $\rho$ ,  $\alpha_{\max}$  is the maximum line density and  $\rho_{\max}$  is that value of  $\rho$  which exists at the height of  $\alpha_{\max}$ . It is assumed that  $\rho$  is given by

$$\rho = \rho_0 \exp \left( -\frac{h}{H} \right)$$

where  $h$  is height and  $H$  is the atmospheric scale height.

It may be shown (Eshleman 1955) that the duration of the radar echo from an overdense cloud of electrons is given by

$$T = \text{constant} \times \frac{\alpha_{\max}^m}{D}$$

where  $D$  is the diffusion coefficient and the exponent  $m$  is unity for a cylindrical cloud (length much greater than diameter) and equals  $2/3$  for a spherical cloud. It should be noted that for a spherical cloud  $\alpha$  is the total number of electrons. If a cylindrical cloud is overdense for a line density greater than  $\alpha_c$  electrons/meter, a spherical cloud will be overdense if the total number of electrons is

$$\alpha > \frac{\lambda}{\pi} \alpha_c,$$

which is about  $3 \times 10^{14}$  electrons for our 9.2-meter radar. A further condition is that a spherical cloud containing this number of electrons must have a radius greater than about  $\lambda/\pi^{3/2}$  to present an overdense target.

For  $1/D \propto \rho$ ,  $T$  is given by

$$T = \text{constant} \times \left( \frac{\rho}{\rho_{\max}} \right)^{m+1} \left( 1 - \frac{1}{3} \frac{\rho}{\rho_{\max}} \right)^{2m}.$$

The maximum value of  $T$  occurs at

$$\rho = \frac{3}{2} \rho_{\max}, \quad m = 1;$$

$$\rho = \frac{5}{3} \rho_{\max}, \quad m = \frac{2}{3}.$$

Normalizing to the values of  $T_{\max}$  we have

$$\frac{T}{T_{\max}} = \frac{16}{9} \left( \frac{\rho}{\rho_{\max}} \right)^2 \left( 1 - \frac{1}{3} \frac{\rho}{\rho_{\max}} \right)^2, \quad m = 1;$$

$$\frac{T}{T_{\max}} = \frac{3^{13/3}}{2 \times 10^{5/3}} \left( \frac{\rho}{\rho_{\max}} \right)^{5/3} \left( 1 - \frac{1}{3} \frac{\rho}{\rho_{\max}} \right)^{4/3}, \quad m = \frac{2}{3}.$$

The function  $T/T_{\max}$  has been plotted in Fig. 2 along with  $\alpha/\alpha_{\max}$ . The abscissa is in units of scale height referred to the height of maximum ionization  $h_{\max}$ .

An inspection of Figs. 1(a) and 1(c) shows that these echoes conform in a qualitative way with the  $T/T_{\max}$  function. From maximum range they exhibit a gradual increase in duration down to the range at which  $T_{\max}$  occurs; from this point to minimum range there is a very rapid decrease in duration. Figure 1(a) is marred slightly as an example because the  $T_{\max}$  point of the second meteor (or second component of the same meteoroid) causes a "bump" on the upper portion of the decay curve.

Over the initial portions of the trail, that is, when  $\rho/\rho_{\max} \ll 1$ ,

$$T \propto \rho^{m+1},$$

$$T \propto \exp \left( - (m+1) \frac{h}{H} \right).$$

Thus,

$$\log_{10} T = \text{constant} - 0.434(m+1) \frac{h}{H}.$$

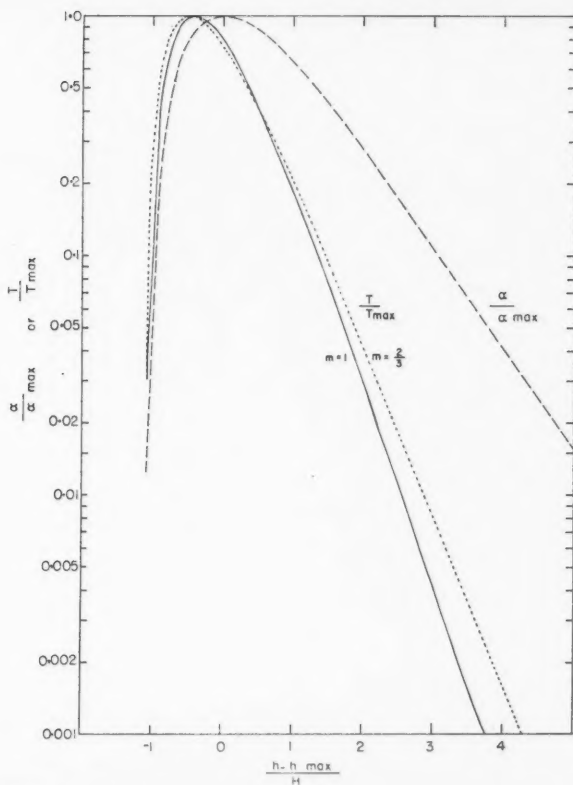


FIG. 2. Theoretical normalized electron line density  $\alpha/\alpha_{\max}$  and meteor echo duration  $T/T_{\max}$ . For the  $T/T_{\max}$  function:  $m = 1$  applies to cylindrical scatterers,  $m = 2/3$  applies to spherical scatterers. The abscissa is in units of scale height referred to the height of maximum ionization  $h_{\max}$ .

A curve of  $\log_{10} T$  vs.  $h$  has been obtained by Millman and Barker (unpublished) for each of some 80 visually observed Perseid meteors which produced  $b$ -type echoes. The mean slope  $dh/d \log_{10} T$  was estimated graphically for each curve. The calculated scale heights for  $m = 1$  are shown in Fig. 3 (crosses) along with 5-kilometer class averages. The bars indicate the standard deviations of the averages. Scale heights calculated for  $m = 2/3$  were obtained simply by multiplying the  $m = 1$  averages by 5/6. These are shown in Fig. 4 (filled circles) where the  $m = 1$  values have also been replotted.

Among other sources of data on scale height, values derived from rocket measurements are most frequently quoted. For comparison purposes we have plotted in Fig. 4 three sets of such data. They are: the Rocket Panel (1952) (dotted curve), the ARDC Model Atmosphere 1956 (Minzer and Ripley

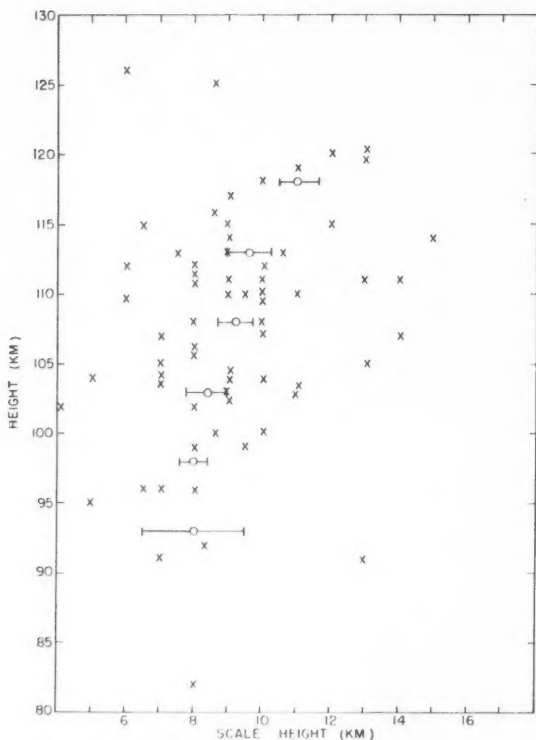


FIG. 3. Scale heights calculated from *b*-type echoes: X, assumption of cylindrical scatterers ( $m = 1$ ). The open circles are averages for 5-kilometer class intervals.

1956) (broken curve), the ARDC Model Atmosphere 1959 (Minzer, Champion, and Pond 1959) (solid curve). Although there is a wide scatter in the individual values obtained from *b*-type echoes, the 5-kilometer class averages agree well with the rocket data, and show a smooth trend toward increased scale height at increasing altitudes.

#### DISCUSSION

No attempt has been made to estimate the errors involved in reducing the data, but a few sources of error may be mentioned. Many *b*-type echoes have highly irregular contours. The worst were rejected for this analysis, but cases such as Fig. 1(a) with uniform graininess and a smooth contour are the exception rather than the rule. The irregularity is probably due to randomness in the size and density of the individual scattering centers; that is, assumption 2 is not satisfied. Many of the components will have, at formation, some aspect sensitivity which will be lost gradually due to diffusion and turbulence. A minor factor which may contribute to the irregularity of the echoes is that the

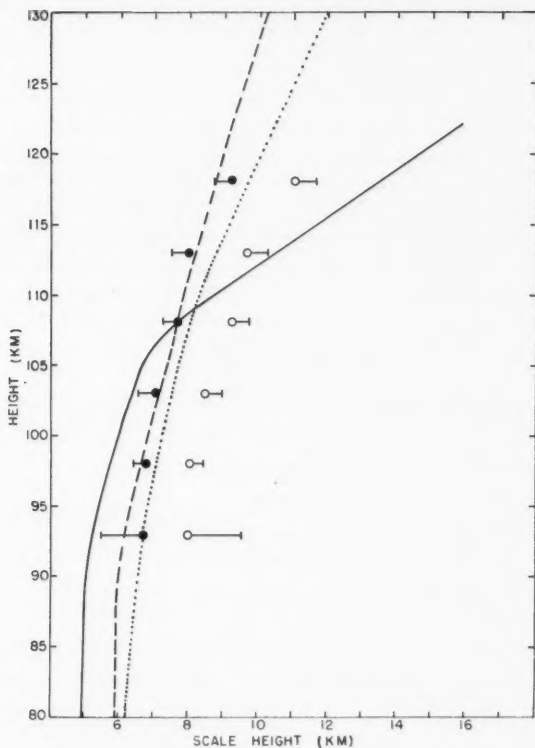


FIG. 4. Scale heights calculated from *b*-type echoes compared with rocket-measured values: open circles, assumption of cylindrical scatterers ( $m = 1$ ); filled circles, assumption of spherical scatterers ( $m = 2/3$ ); dotted curve, Rocket Panel 1952; broken curve, ARDC Model Atmosphere 1956; solid curve, ARDC Model Atmosphere 1959.

power received from long cylindrical clouds varies as  $R^{-3}$  (where  $R$  is range), whereas it varies as  $R^{-4}$  for spherical clouds.

In about fifty per cent of the cases the heights of the meteor trails were obtained from the radar range measurement and from the plot of the trail by a visual observer. These latter observations are subject to large errors. For the remaining echoes, height was determined more accurately by three-station radar triangulation.

Because of the lack of precision of the experimental data and since the rocket measurements themselves show a wide spread, positive assertions cannot be made about Fig. 4. However, the agreement is sufficiently good to lend some support to the foregoing analysis. It is reasonable to expect that the blobs of ionization along the rough meteor trail will have a variety of shapes running from cylinders to spheres. If one compares the meteor-derived scale height values with the Rocket Panel 1952 and ARDC 1956 data, it would seem that the tendency is toward more spherical shapes.

## CONCLUSIONS

It seems fairly conclusive that *b*-type echoes are a result of reflections from a large number of individual clouds of electrons produced by the passage of a meteoroid. Although the reason for this patchy ionization is not certain, it may be due to the fragmenting of a dustball type of meteoroid. It has been shown that the characteristic shape of *b*-type echoes is closely associated with the rate of production of ionization along the meteor trail and the coefficient of diffusion in the atmosphere. On the basis of a rough-trail theory, values of atmospheric scale height were determined from the duration vs. height profiles of the echoes. The fact that these values agree well with rocket measurements of scale height supports the validity of the rough-trail analysis of *b*-type echoes presented here.

## ACKNOWLEDGMENTS

The author wishes to thank Dr. Peter M. Millman for permission to use his unpublished data.

## REFERENCES

- ESHLEMAN, VON R. 1955. IRE Trans. **AP-3**, 32.  
JACCHIA, L. G., KOPAL, Z., and MILLMAN, P. M. 1950. Astrophys. J. **111**, 104.  
KAISER, T. R. 1953. Phil. Mag. Suppl. **2**, 495.  
MCKINLEY, D. W. R. 1961. Meteor science and engineering (McGraw-Hill Book Co., New York). In press.  
MCKINLEY, D. W. R. and MILLMAN, P. M. 1949. Proc. I.R.E. **37**, 364.  
MCNAMARA, A. G. and MCKINLEY, D. W. R. 1959. J. Atmospheric and Terrest. Phys. **16**, 156.  
MINZER, R. A. and RIPLEY, W. S. 1956. Air Force Cambridge Research Center, AFCRC-TN-56-204.  
MINZER, R. A., CHAMPION, K. S. W., and POND, H. L. 1959. Air Force Cambridge Research Center, AFCRC-TR-59-267.  
ÖPIK, E. J. 1958. Physics of meteor flight in the atmosphere (Interscience Publishers Inc., New York).  
RAO, M. S. and ARMSTRONG, R. L. 1958. Can. J. Phys. **36**, 1601.  
ROCKET PANEL. 1952. Phys. Rev. **88**, 1027.  
WHIPPLE, F. L. 1943. Revs. Modern Phys. **15**, 246.

# PHONON DRAG IN LEAD<sup>1</sup>

A. V. GOLD<sup>2</sup> AND W. B. PEARSON

## ABSTRACT

We have carried out measurements on the thermoelectric power of dilute alloys of lead with the solutes Cd, In, Sn, Tl, and Bi in order to test a plausible hypothesis that much of the thermoelectric behavior of pure lead at low temperatures can be ascribed to phonon drag. The results are qualitatively consistent with the phonon-drag picture only if it is assumed that the scattering of phonons by these impurities depends more critically on the valence difference between solvent and solute than on the mass difference.

The absolute thermoelectric power  $S$  of pure lead varies very rapidly with temperature below about 20° K (Christian *et al.* 1958; Fig. 1, broken curve).

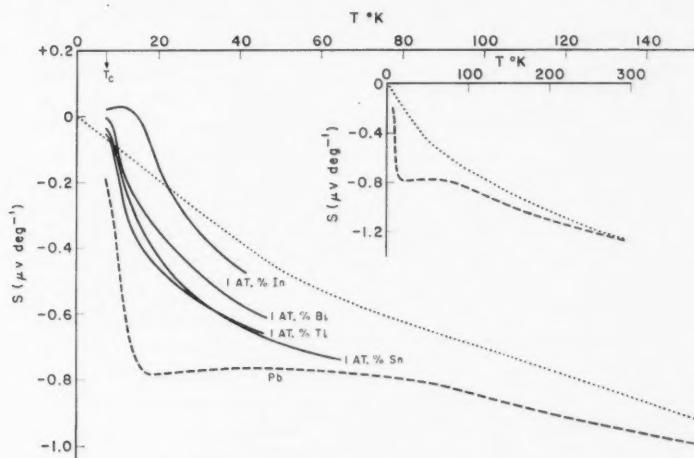


FIG. 1. Temperature dependence of absolute thermoelectric power  $S$  for pure lead (---; Christian *et al.* 1958) and for four dilute alloys (—); ·····, plausible diffusion component  $S_d$ .

We wish to show first of all how an analysis of the low-temperature data suggests that the rapid variation of  $S$  might plausibly be accounted for by the presence of a relatively large 'phonon-drag' component of thermoelectricity.

According to simple theory the ordinary diffusion thermoelectric power  $S_d$  should be proportional to the absolute temperature  $T$  (cf. Mott and Jones

<sup>1</sup>Manuscript received November 4, 1960.

Contribution from the Division of Pure Physics, National Research Council, Ottawa, Canada.

Issued as N.R.C. No. 6175.

<sup>2</sup>N.R.C. Postdoctorate Fellow. Now at Physics Department, Iowa State University, Ames, Iowa, U.S.A.

1936), while the phonon-drag thermoelectric power  $S_g$  should vary as  $T^3$  at the lowest temperatures (cf. MacDonald 1954; Hanna and Sondheimer 1957). Thus we may write

$$(1) \quad S = S_d + S_g = aT + bT^3,$$

and if this equation is obeyed at low temperatures, a plot of  $S/T$  vs.  $T^2$  should yield a straight line. This appears to be the case for the pure lead data of Christian *et al.* (Fig. 2(a)) and we find for the coefficients the values

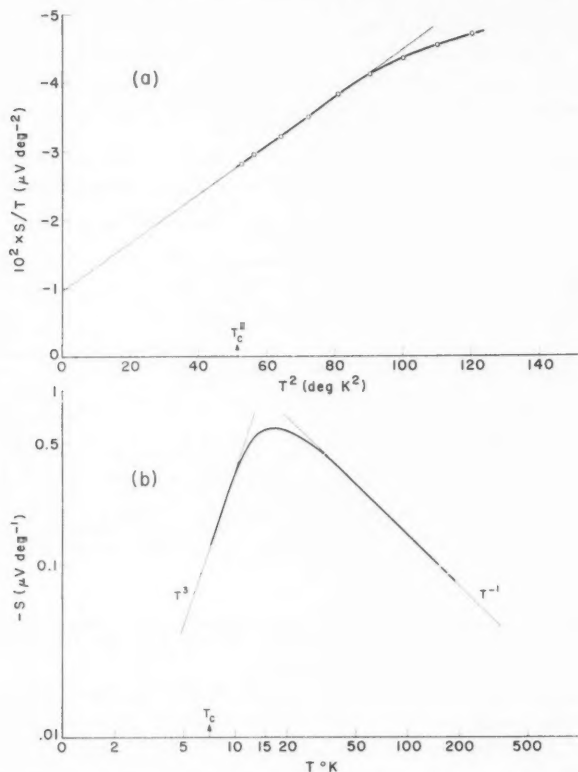


FIG. 2. (a) Plot of  $S/T$  vs.  $T^2$  for the pure lead data of Christian *et al.* (b) Phonon-drag component  $S_g$  as inferred from the discussion of pure lead.

$a = -9.8 \times 10^{-3} \mu\text{V deg}^{-2}$  and  $b = -3.5 \times 10^{-4} \mu\text{V deg}^{-4}$  from, respectively, the intercept at  $T = 0$  of the extrapolated straight line and its slope. When eq. (1) is integrated, using the values of  $a$  and  $b$  as just determined, we find good agreement with the results of Steele (1951), who measured the thermal e.m.f.  $E = \int SdT$  below the superconducting transition temperature  $T_c$  in the presence of a magnetic field sufficient to destroy the superconductivity.



If we now suppose that  $S_g$  is negligible at room temperature on account of ph non-phonon scattering, we find that the temperature dependence of  $S_d$  must depart from the low-temperature straight line in order to join up with observed results at high temperatures. A plausible curve for  $S_d$  is shown in the inset of Fig. 1 (dotted curve); such a deviation from linearity could possibly be a consequence of the rapid variation with energy of the density of states curve near the Fermi level (Gold 1960). (We should make it clear that impurity scattering effects are negligible at temperatures above  $T_c$  for lead of this high purity.) By subtracting this hypothetical curve for  $S_d$  from the observed results we obtain the presumed phonon-drag term  $S_g$  which is plotted on a logarithmic scale in Fig. 2(b). The maximum in  $S_g$  then occurs near 16° K; this temperature corresponds to approximately  $\Theta_D/5$ , the temperature near which the phonon-drag maxima are found in the alkali and noble metals (MacDonald *et al.* 1958; Gold *et al.* 1960; Pearson 1960*a, b*; Blatt and Kropschot 1960) and above the maximum  $S_g$  is found to decrease more or less as  $T^{-1}$  in accordance with theory (Hanna and Sondheimer 1957). The foregoing analysis thus makes it seem probable that much of the low-temperature behavior of the thermoelectricity in lead can be ascribed to phonon drag. In an attempt to check these conclusions we have carried out experiments on several dilute lead alloys.

Our choice of alloys to investigate has been governed by the following considerations. In order to find out if phonon drag is operative in the way we have suggested, we wish to add impurities which scatter phonons, thereby reducing the fraction of the momentum which the phonons can impart to the electrons and thus leading to a reduction in the phonon-drag component  $S_g$ . Impurities should scatter phonons effectively provided that their atomic mass differs markedly from that of the parent lattice and we have chosen in the first place the impurities Cd, In, and Sn, whose atomic masses are roughly half that of lead. However, in addition to reducing the phonon drag, the impurities will also change the diffusion term  $S_d$  because of impurity scattering of *electrons* which becomes important at low temperatures. In order to distinguish between these two effects we have also made measurements on alloys with Tl and Bi; these solutes have practically *the same* atomic mass as lead so that  $S_g$  should remain virtually unaffected and any changes in the observed thermoelectric power should be those in  $S_d$  alone.

The alloys were prepared from spectroscopically pure Johnson-Matthey lead with up to 1 at.% of spectroscopically pure Tadanac Cd, In, Sn, and Bi, and Tl from A. D. Mackay. The lead and solute were melted together under vacuum, thoroughly agitated, and then solidified by quenching in water in order to keep the impurity distribution as uniform as possible. The ingots were subsequently homogenized by keeping them at about 10 degrees below the melting temperature for several days, after which they were extruded into 0.02 in. diameter wires. Values of  $\Delta S$ , the difference in thermoelectric power between the alloy and a wire of very pure zone-refined lead, were obtained from total e.m.f. measurements using an improved version of the technique described by MacDonald and Pearson (1953), the e.m.f. being

measured at roughly  $\frac{1}{2}^\circ$  intervals on a Cambridge vernier potentiometer. This method of obtaining  $\Delta S$  is not as accurate as the differential technique of Christian *et al.*, but is much more convenient, and we believe that the  $\Delta S$  values obtained are reliable to about  $\pm 0.03 \mu\text{V deg}^{-1}$ . Curves of the temperature dependence of  $\Delta S$  for the various alloys between  $7.2^\circ\text{K}$  and about  $50^\circ\text{K}$  are shown in Fig. 3 (full curves), and the variations with temperature of the absolute thermoelectric power for the four 1% alloys have been included in Fig. 1.

We begin a discussion of the effects of alloying by considering first the changes in the ordinary diffusion term  $S_d$ . In an attempt to understand these results we shall make use of Kohler's (1949) expression for the thermoelectric power of a metal when the electrons are being scattered by both impurities and thermal vibrations (cf. also Gold *et al.* 1960, Appendix I):

$$(2) \quad S_{d,\text{alloy}} = S_{d,\text{imp}} \frac{W_{\text{imp}}}{W_{\text{imp}} + W_{\text{th}}} + S_{d,\text{th}} \frac{W_{\text{th}}}{W_{\text{imp}} + W_{\text{th}}}.$$

Here  $S_{d,\text{imp}}$  and  $S_{d,\text{th}}$  are the diffusion thermoelectric powers which would be observed if the electrons were being scattered entirely by impurities or entirely by phonons, and  $W_{\text{imp}}$  and  $W_{\text{th}}$  are the components of the electronic thermal resistivity arising from impurity and phonon scattering. The expression (2) is only approximately correct for the present work. Lead is a two-band metal with a quite complicated Fermi surface (Gold 1958), and although hole conduction is dominant (Borovik 1954), Kohler's relation strictly speaking assumes a single group of carriers with a spherical Fermi surface and isotropic relaxation time. It assumes in addition that there are no changes in the band structure and Fermi level on alloying, that lattice heat conduction is negligible, and that Matthiessen's rule holds for the *thermal* resistivities; departures from the Matthiessen rule for the *electrical* resistivities of the present alloys have been discussed by Eucken and Schürenberg (1938; see caption to Fig. 3).

Equation (2) can be simplified by noting that the absolute thermoelectric powers of the alloys become very small in the impurity scattering region below  $\sim 10^\circ\text{K}$  (Fig. 1), i.e. at low temperatures at least,  $S_{d,\text{imp}}$  is very small. At higher temperatures, on the other hand,  $W_{\text{imp}}/(W_{\text{imp}} + W_{\text{th}})$  becomes small so that we shall suppose the first term on the right side of eq. (2) to be effectively zero over the entire temperature range of the present measurements. Since  $S_{d,\text{th}}$  is simply  $S_{d,\text{Pb}}$  for pure lead, eq. (2) then gives

$$(3) \quad \Delta S_d = S_{d,\text{alloy}} - S_{d,\text{Pb}} = -S_{d,\text{Pb}} \frac{W_{\text{imp}}}{W_{\text{imp}} + W_{\text{th}}}.$$

In order to compare eq. (3) with experiment we have taken for  $W_{\text{th}}$  the thermal

FIG. 3. Temperature dependence of  $\Delta S = S_{\text{alloy}} - S_{\text{Pb}}$  (—); ·····,  $\Delta S_d$  from eq. (3) assuming phonon drag; - - -,  $\Delta S_d$  from eq. (3) assuming no phonon drag. The figures in brackets are measured values of  $\rho_0$  in  $\mu\Omega\text{cm}$  (at  $4.2^\circ\text{K}$ ), assuming  $\rho_{297^\circ\text{K}} = 20.9 \mu\Omega\text{cm}$  for pure lead. The values of  $\rho_0$  per atomic per cent solute are all smaller than those found by Eucken and Schürenberg (1938) at temperatures above  $20^\circ\text{K}$  (by as much as 50% for the Cd alloy), in line with the departures from Matthiessen's rule reported by these authors at higher temperatures.

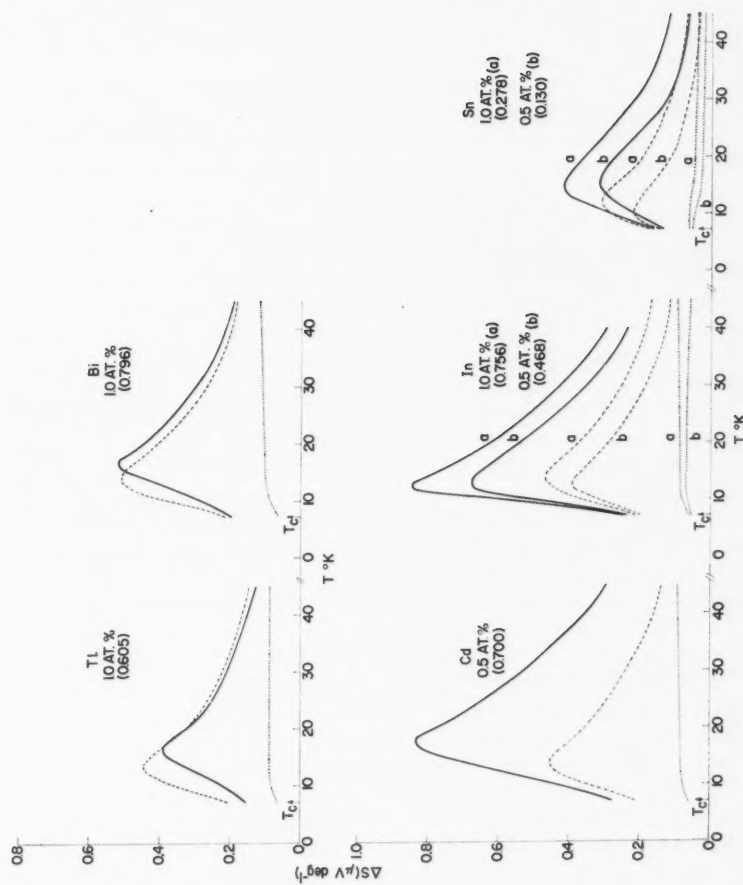


FIG. 3.

resistivity data on pure lead of de Haas and Rademakers (1940) up to 23° K, and have interpolated between these results and the 'classical' room temperature value (see Powell and Blanpied 1954).  $W_{\text{imp}}$  we have obtained from the Wiedemann-Franz-Lorenz relation

$$(4) \quad W_{\text{imp}} = \rho_0/L_0T,$$

where  $\rho_0$  is the residual resistivity and  $L_0 = \pi^2 k^2/3e^2$ ; values of  $\rho_0$  were obtained by extrapolating to zero magnetic field resistance measurements at 4.2° K in transverse fields up to 15 kilogauss.

Taking for  $S_{\text{d,pb}}$  the dotted curve in Fig. 1, as suggested by our analysis of the pure lead data, the variations of  $\Delta S_{\text{d}}$  with temperature calculated from eq. (3) are shown as the dotted curves in Fig. 3. We note first of all that the calculated curves for the alloys with Tl and Bi fall far short of the observed results and give no indication whatsoever of a maximum in  $\Delta S$  at about 16° K. Since the observed maxima occur at approximately the same temperature as the phonon-drag maximum in Fig. 2(b) it would appear that we must interpret the difference  $\Delta S - \Delta S_{\text{d}}$  between the solid and dotted curves as a reduction  $\Delta S_{\text{g}}$  in the phonon-drag component due to some phonon scattering by the Tl and Bi impurities other than by virtue of the small (<2%) mass differences involved, e.g. due to the change in elastic constants in the neighborhood of an impurity atom (Klemens 1955). Turning to the alloys with Cd, In, and Sn, we find that  $\Delta S - \Delta S_{\text{d}}$  for a given solute concentration increases as the valence difference increases whereas we should have expected  $\Delta S_{\text{g}}$  to be approximately the same for all three alloys if the phonons were being scattered on account of the mass differences alone. Thus the alloy results can be qualitatively understood in terms of a reduction in  $S_{\text{g}}$  only if it is assumed that the phonon-impurity scattering depends more critically on the *valence* difference between solvent and solute than on the mass difference, but it is difficult to make a quantitative comparison with Klemens' (1955) theory.

There might, however, be an alternative explanation of the alloy results. If we reject the *phonon-drag hypothesis entirely* and take for  $S_{\text{d,pb}}$  in eq. (3) the actual experimentally observed values of Christian *et al.*, we obtain the broken curves  $\Delta S'_{\text{d}}$  in Fig. 3. For the Tl and Bi alloys these curves have a maximum at roughly the same temperature and of about the same magnitude as the observed curves, so that we could account nicely for the behavior on alloying with Tl and Bi by assuming that the thermoelectricity in pure lead is entirely 'diffusion' in character. However, the curves for  $\Delta S'_{\text{d}}$  calculated on this assumption do not account well for the results with Cd, In, and Sn impurities suggesting that our previous interpretation is the more likely one. Again, if the phonon-drag hypothesis were to be rejected, then some other explanation would have to be invoked to account for the temperature dependence of the pure lead results.

Finally we wish to point out that the relatively large phonon-drag component proposed in Fig. 2(b) is much smaller than that predicted by simple theory (Hanna and Sondheimer 1957); the value of the coefficient  $b$  of the

low-temperature  $T^3$  term is only about 3% of the theoretical value deduced from the lattice specific heat on the assumption of one carrier per atom. This may be plausibly understood by remembering that the hole and electron Fermi surfaces in lead contain the same number of carriers (about 0.41 per atom) so that one might expect the magnitude of  $S_g$  from each band to be roughly the same for  $N$ -scattering processes alone, but of *opposite* sign; furthermore the contributions from the  $U$ - and  $N$ -processes within each band will tend to cancel each other.

#### ACKNOWLEDGMENTS

We are grateful to Drs. M. Bailyn, J. S. Dugdale, and D. K. C. MacDonald for helpful discussions.

#### REFERENCES

- BLATT, F. J. and KROPSCHOT, R. H. 1960. Phys. Rev. **118**, 480.  
 BOROVIK, E. S. 1954. J. Exptl. Theoret. Phys. U.S.S.R. **27**, 355.  
 CHRISTIAN, J. W., JAN, J.-P., PEARSON, W. B., and TEMPLETON, I. M. 1958. Proc. Roy. Soc. (London), A, **245**, 213.  
 DE HAAS, W. J. and RADEMAKERS, A. 1940. Physica, **7**, 992.  
 EUCKEN, A. and SCHÜRENBERG, H. 1938. Ann. Physik (5) **33**, 1.  
 GOLD, A. V. 1958. Phil. Trans. Roy. Soc. (London), A, **251**, 85.  
 ——— 1960. Phil. Mag. **5**, 70.  
 GOLD, A. V., MACDONALD, D. K. C., PEARSON, W. B., and TEMPLETON, I. M. 1960. Phil. Mag. **5**, 765.  
 HANNA, I. I. and SONDEHEIMER, E. H. 1957. Proc. Roy. Soc. (London), A, **239**, 247.  
 KLEMENS, P. G. 1955. Proc. Phys. Soc. (London), A, **68**, 1113.  
 KOHLER, M. 1949. Z. Physik, **126**, 481.  
 MACDONALD, D. K. C. 1954. Physica, **20**, 996.  
 MACDONALD, D. K. C. and PEARSON, W. B. 1953. Proc. Roy. Soc. (London), A, **219**, 373.  
 MACDONALD, D. K. C., PEARSON, W. B., and TEMPLETON, I. M. 1958. Proc. Roy. Soc. (London), A, **248**, 107.  
 MOTT, N. F. and JONES, H. 1936. Theory of metals and alloys (Clarendon Press, Oxford).  
 PEARSON, W. B. 1960a. Phys. Rev. **119**, 549.  
 ——— 1960b. Can. J. Phys. **38**, 1048.  
 POWELL, R. L. and BLANPIED, W. A. 1954. Natl. Bur. Standards Circ. No. 556, Washington.  
 STEELE, M. C. 1951. Phys. Rev. **81**, 262.

# MAGNETORESISTANCE AND HALL EFFECT IN ORIENTED SINGLE CRYSTAL SAMPLES OF *n*-TYPE INDIUM ANTIMONIDE<sup>1, 2</sup>

C. H. CHAMPNESS

## ABSTRACT

Measurements have been made on the angular dependence of the magnetoresistance effect and the Hall effect on oriented *n*-type indium antimonide samples. The measurements were taken at room temperature and liquid air temperature using a magnetic field strength of about 5000 gauss. Besides evidence of inhomogeneity, the results show directional dependence of the longitudinal magnetoresistance. The largest value was found in the (100) direction. This can be explained if, in addition to electrons at the central minimum, there is some filling of the (111) minima in *k* space.

## 1. INTRODUCTION

While a large amount of work has been done on the galvanomagnetic properties of *n*-type indium antimonide, there appears to have been no detailed rotational study using oriented single crystal specimens. Possibly one reason for this is that it was thought that such work would not show up anything special because cyclotron resonance and preliminary magnetoresistance experiments had indicated that, unlike germanium, the conduction band electrons of indium antimonide had an isotropic effective mass. However, it is instructive to review briefly some of the experiments supporting the idea of spherical energy surfaces.

The observation of cyclotron resonance carried out by Dresselhaus, Kip, Kittel, and Wagoner (1955) was isotropic under a rotation in a (100) plane. This indicates that at the temperature of the experiment, namely 4° K, spherical energy surfaces prevail. In the room temperature cyclotron resonance experiments of Burstein *et al.* (1956) and of Keyes *et al.* (1956) rotation of the crystals was not carried out. Hence isotropy at room temperature has not been definitely established.

So far as magnetoresistance is concerned, the first angular dependence was studied by Pearson and Tanenbaum (1953) on a polycrystalline sample which was *p*-type below 175° K. This work showed that the magnetoresistance almost vanished when the current (*I*) and the magnetic field (*H*) were parallel. Measurements on *n*- and *p*-type single crystal samples at room temperature and 77° K were later carried out by Tanenbaum, Pearson, and Feldman (1954); the samples were cut with their current axes along the [100] and the [110] directions. They reported that they obtained the same results as on the polycrystalline material but no published curves of these particular measurements have appeared. Other workers, however, have found that the magneto-

<sup>1</sup>Manuscript received October 14, 1960.

Contribution from the Eaton Electronics Research Laboratory, Dept. of Physics, McGill University, Montreal. This work was supported by the Office of Naval Research and in part by the Defence Research Board.

<sup>2</sup>Submitted in partial fulfilment of the Ph.D. degree, McGill University.

resistance does not fall to zero when  $I$  and  $H$  are parallel. Work on degenerate polycrystalline material by Mansfield (1955) showed that the longitudinal magnetoresistance could be an appreciable fraction of the transverse effect. Work on two single crystal unoriented samples by Frederikse and Hosler (1957) showed in one case a longitudinal magnetoresistance which was positive at small fields but became negative as the magnetic field was increased; the other sample showed a positive effect for  $I$  parallel to  $H$  but underwent changes of sign to negative and then back to positive values as the angle between  $I$  and  $H$  was increased. Using pulsed fields up to 180 kilogauss, Haslett and Love (1959) found longitudinal magnetoresistance values up to 25 at 78° K. At this temperature they found that no "freeze out" effects occurred (Keyes and Sladek 1956). Both Frederikse and Hosler and Haslett and Love state that the non-zero longitudinal magnetoresistance can be explained on the basis of a quantum transport treatment such as that of Argyres and Adams (1956). It is difficult to believe that this is so, at least as far as room temperature is concerned. At this temperature and a field of  $10^4$  gauss, the reduced Landau splitting energy  $\hbar\omega_c/kT$  would only be about 0.15, taking as the effective mass ratio a "room temperature" value of 0.03. Here  $\omega_c$  is the cyclotron resonance angular frequency,  $T$  is the absolute temperature,  $\hbar$  is Planck's constant divided by  $2\pi$ , and  $k$  is Boltzmann's constant.

According to Herman (1955), the band structure of indium antimonide should be similar to that of the group four elements with minima in  $\mathbf{k}$  space at the center of the reduced zone, along the  $\langle 100 \rangle$  axes and along the  $\langle 111 \rangle$  axes (see Fig. 1). To explain the cyclotron resonance experiments at 4° K, it

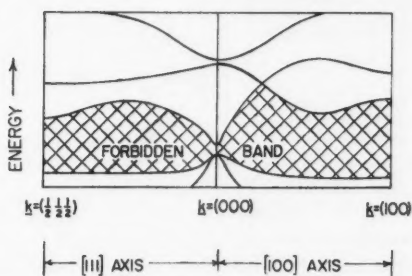


FIG. 1. Schematic energy band diagram for indium antimonide (after Herman 1955).

is supposed that the central minimum must lie below the other minima; the non-central minima are therefore assumed to be unpopulated at low temperatures. Two questions arise. Firstly, how does the presence of an impurity band affect the picture and secondly do the non-central valleys become populated at higher temperatures?

In order to throw some light on these questions, some magnetoresistance measurements were made at room temperature and liquid air temperature on oriented single crystal samples. The measurements were made as a function of the angle  $\theta$  between  $I$  and  $H$  using the same method as that described by



Pearson and Suhl (1951) on germanium. Specifically, the special point of interest was to find the magnitude of the longitudinal magnetoresistance and to see if it was directionally dependent. Some possible evidence for deviation from perfectly spherical energy surfaces was found by Bate, Willardson, and Beer (1959). They found a hump in the variation of the Hall coefficient with magnetic field. However, it is learned (private communication) that this effect may have been due to inhomogeneity in the samples.

## 2. SAMPLES

Three samples were cut from a single crystal of *n*-type indium antimonide with long axes in the [100], [110], and [111] directions. The other faces of the samples were cut as in Fig. 2. The sample dimensions were approximately

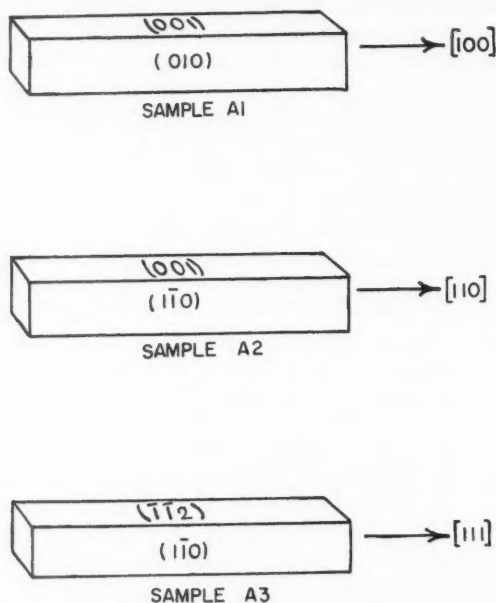


FIG. 2. The orientations of the three samples used for measurement.

$7 \times 1 \times 1$  mm. The material was kindly supplied by the Minneapolis Honeywell Research Center. Figures for the Hall coefficient, conductivity, and Hall mobility taken from the measurements described later are shown in Table II. The mobilities can be roughly accounted for taking into account impurity scattering with  $3 \times 10^{15}$  as the number of impurity centers/cc from the liquid air Hall coefficient. There is therefore no appreciable compensation present.

## 3. METHOD OF MEASUREMENT

Each of the samples was mounted in a special sample holder consisting of a micarta rod with a double flat filed at one end. The sample was mounted in a



slot cut at right angles to the axis of the rod (Fig. 3). The ends of the sample were indium soldered to two small screws tapped in the base of the slot. The screws were made from thin brass wire using a watchmaker's die. Short lengths of platinum wire 0.003 in. in diameter and coated with indium were used for

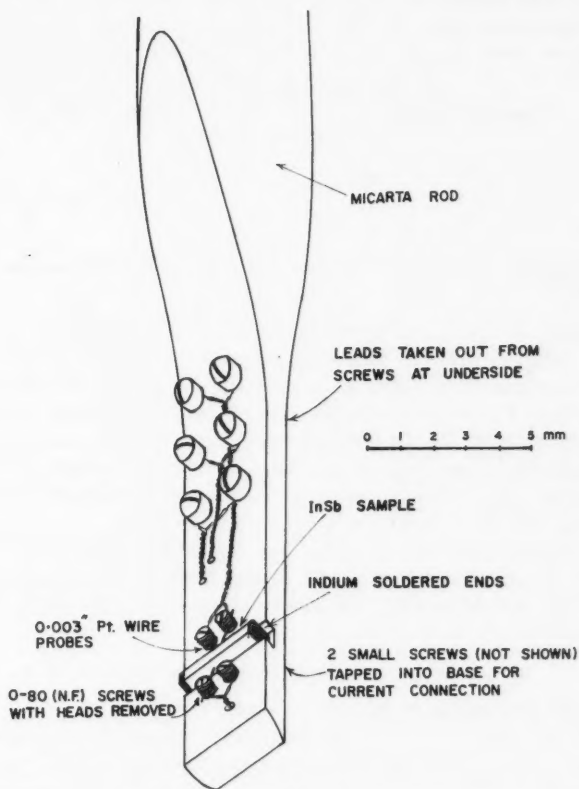


FIG. 3. Sample holder used in the measurements.

the potential probes. These were threaded through small transverse holes drilled in 0-80 (N.F.) screws using watchmakers' drills. The heads of the 0-80 screws were sawn off and screwdriver slots cut in the stems. By twisting the screws in the holder, it was possible for the platinum wires to make contact with the sides of the sample. Good electrical contact was ensured by discharging a  $2.5\text{-}\mu\text{f}$  condenser at 50 volts between each probe and one end of the sample.

Four probes were used on each sample so that two conductivity and two Hall readings could be taken. The sample holder was mounted vertically between the poles of a rotatable 6-in. electromagnet. Alignment of the long

sample axis (current axis) with the magnetic field was done by eye. With the sample fixed, the electromagnet could be rotated round it so as to obtain any angle  $\theta$  between  $I$  and  $H$  (Fig. 4).

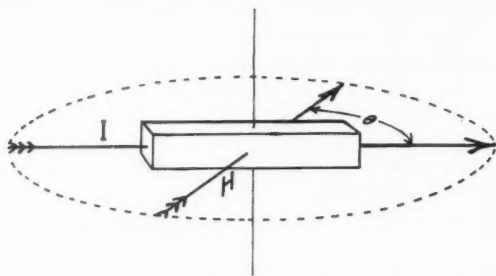


FIG. 4. Schematic diagram showing the position of the probes and the angle of rotation of the magnetic field.

A constant current ( $I$ ) of about 10 ma at room temperature and 1 ma at liquid air temperature was passed through the sample and four potential difference readings were taken at a time using a Leeds and Northrup K.2 potentiometer. To avoid thermoelectric effects, the current was reversed through the sample. To distinguish clearly between the magnetoresistance and the Hall effects, the magnetic field was also reversed for each set of readings. Because of this field reversal, it was only necessary to make the measurements over an angle of  $180^\circ$  of rotation.

Measurements were also made of the variation of the Hall coefficient, transverse magnetoresistance, and longitudinal magnetoresistance with magnetic field strength up to 4880 gauss. The results of this part of the work will be reported in a later publication.

#### 4. EXPERIMENTAL RESULTS

##### 4.1. Angular Dependence of Magnetoresistance

The variation of the magnetoresistance ratio  $\Delta\rho/\rho_0$  with the angle  $\theta$  is given in Figs. 5, 6, 7, and 8 for the three samples; measurements in two planes of rotation of  $H$  were carried out on sample A2. Here  $\rho_0$  is the zero field resistivity and  $\Delta\rho$  is the increase in the resistivity due to a magnetic field. In the measurements, the magnetic field was maintained at 4880 gauss.

The experimental curves in Figs. 5 to 8 show the following general features:

- (a) The magnetoresistance is not zero when  $I$  and  $H$  are apparently parallel at  $\theta = 0^\circ$ .
- (b) The positions of the minima in general deviate from  $\theta = 0^\circ$ .
- (c) The magnetoresistance values at the minima are not zero.
- (d) Negative values occur for some of the minima at room temperature as well as at liquid air temperature.
- (e) Negative values do not occur together on the two sets of probes; if one pair gives a negative value the other pair gives a positive one at the same temperature.

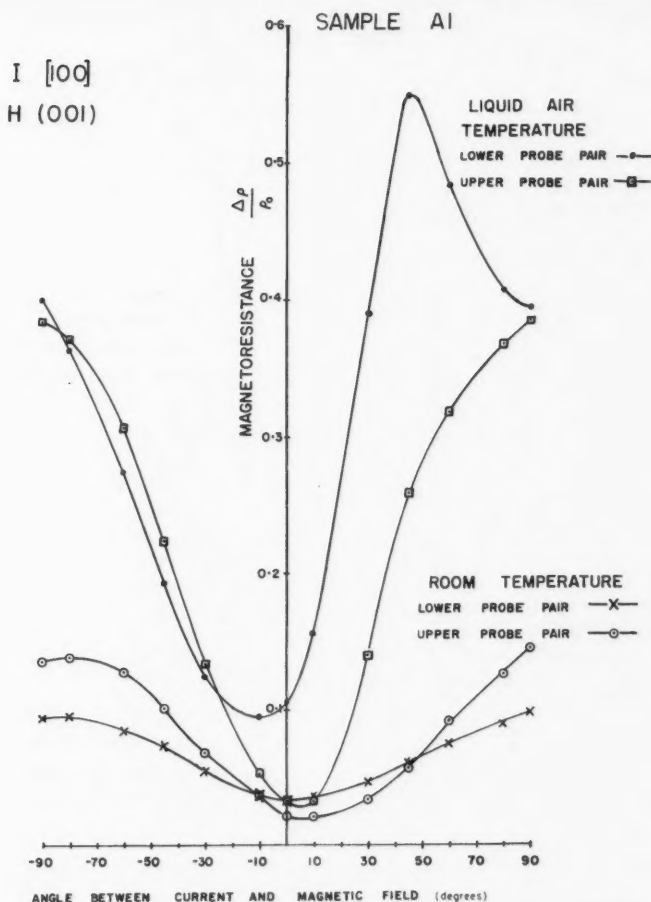


FIG. 5. Variation of the magnetoresistance in the [100] direction of sample A1 with rotation of the magnetic field (4880 gauss) in an (001) plane.

(f) The maxima in general are displaced in the same direction as the corresponding minima. Most of the minima are displaced to the right of the origin.

(g) The values at the minima for the [100] sample (A1) are larger than for the other cases. In particular, no negative magnetoresistance is observed either at room or at liquid air temperature on this sample.

(h) There are no subsidiary minima near  $\theta = 0^\circ$ , such as were observed by Frederikse and Hosler (1957).

(i) Apart from the above-mentioned deviations, the curves have roughly the shape of a  $\sin^2 \theta$  curve, which would ideally correspond, for weak fields, to spherical energy surfaces.

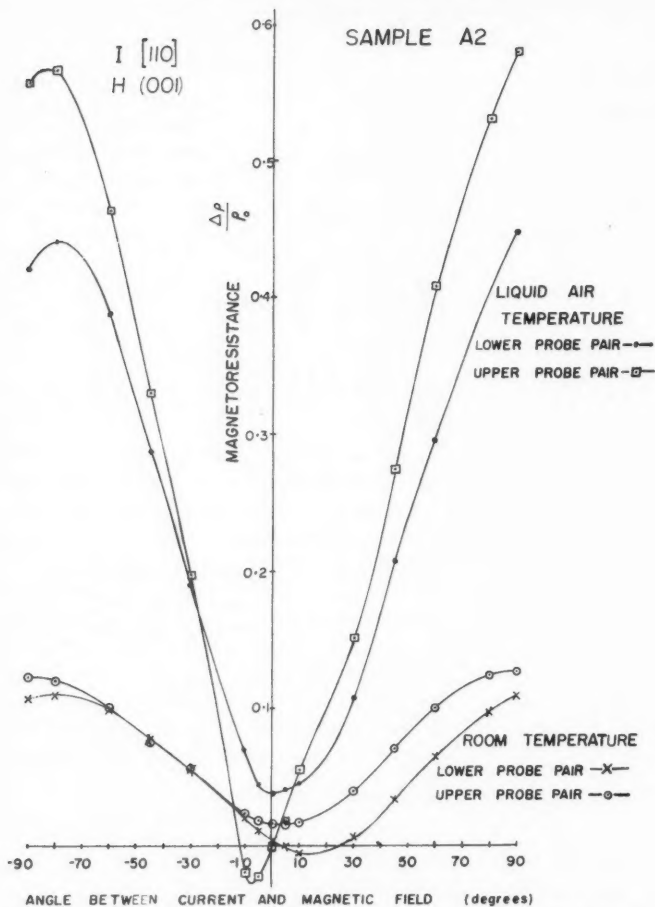


FIG. 6. Variation of the magnetoresistance in the [110] direction of sample A2 with rotation of the magnetic field (4880 gauss) in an (001) plane.

TABLE I  
Average magnetoresistance values at 4880 gauss on three oriented samples

Sample	Current direction	Transverse magnetoresistance $\Delta\rho/\rho_0$			Longitudinal magnetoresistance $\Delta\rho/\rho_0$		
		Room temp. (298° K)	Liq. air temp. (77–90° K)	Magnetic field direction	Room temp. (298° K)	Liq. air temp. (77–90° K)	Magnetic field direction
A1	[100]	0.116	0.46	[010]	0.028	0.061	[100]
A2	[110]	0.117	0.51	[110]	0.0045	0.01	[110]
		0.110	0.41	[001]	0.008	–0.02	[110]
A3	[111]	0.105	0.30	[112]	–0.006	0.0075	[111]

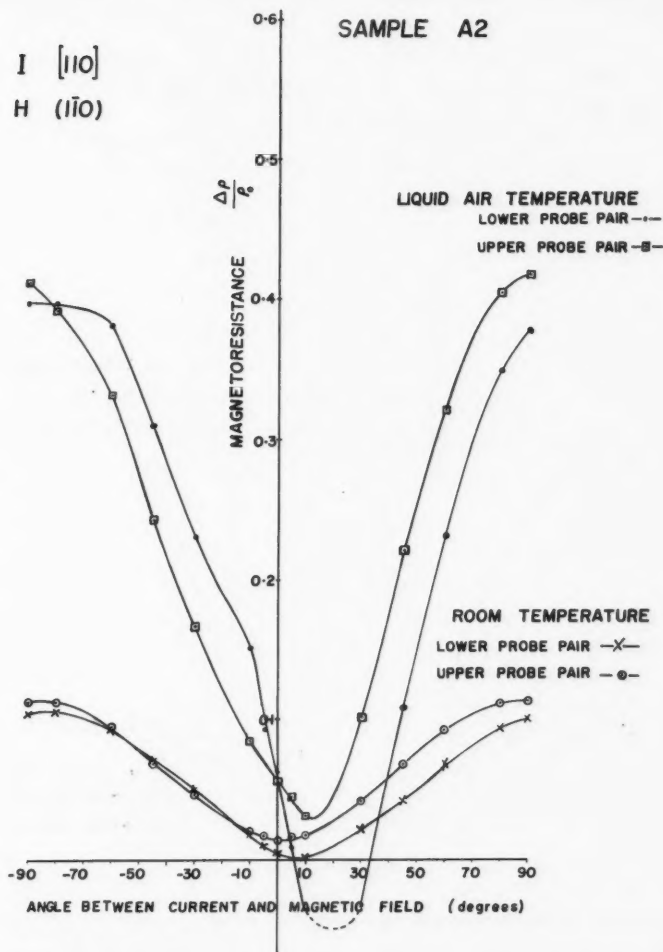


FIG. 7. Variation of the magnetoresistance in the [110] direction of sample A2 with rotation of the magnetic field (4880 gauss) in a ( $\bar{1}\bar{1}0$ ) plane.

For the longitudinal magnetoresistance, values were taken at the minima rather than at  $\theta = 0^\circ$ . Table I shows these values together with the transverse magnetoresistance values averaged, in both cases, for the two sets of probes. It is clearly seen from the table that the longitudinal effect is largest in the [100] direction both at room temperature and at liquid air temperature. The smallest effect is not so clearly shown; it is apparently in the [111] direction at room temperature and in the [110] direction at liquid air temperature. The transverse effect does not appear to show any marked dependence on direction.

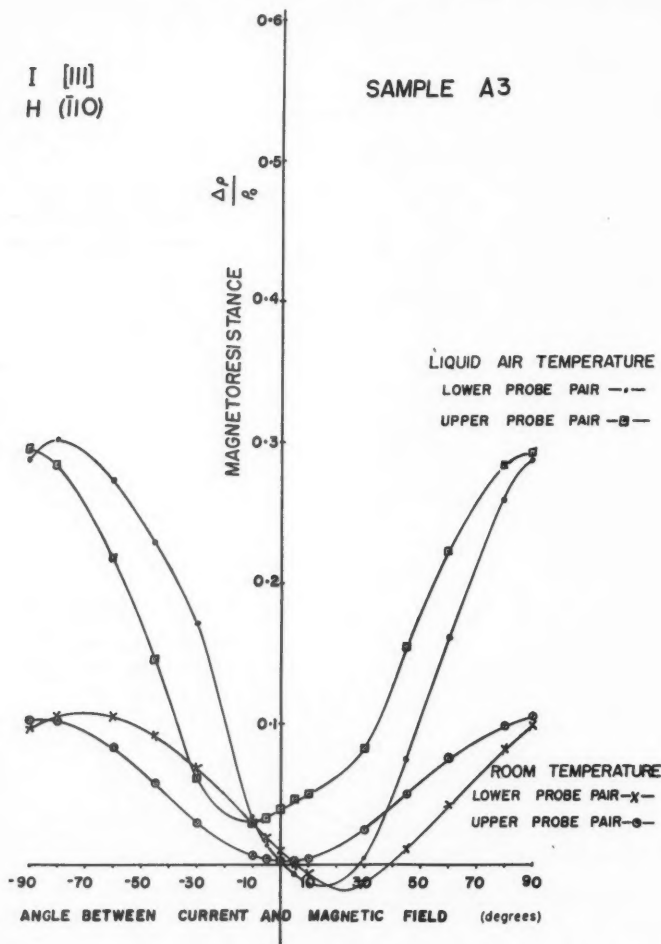


FIG. 8. Variation of the magnetoresistance in the [111] direction of sample A3 with rotation of the magnetic field (4880 gauss) in a (110) plane.

#### 4.2. Angular Dependence of Hall Effect

From the readings, values of the quantity  $10^8 V_H t / IH$  cm<sup>3</sup>/coulomb were worked out ( $V_H$  is the Hall potential difference measured across the sample in volts,  $I$  is the sample current in amperes,  $H$  is the magnetic field in oersteds, and  $t$  is the sample thickness in centimeters). This quantity, which could be called the reduced Hall voltage, is equal to the Hall coefficient ( $R_H$ ) when  $I$  and  $H$  are perpendicular to each other. Ideally it would be equal to  $R_H \sin \theta$ . It is plotted against  $\theta$  for the three samples in Figs. 9, 10, 11, and 12 corresponding respectively to the previous four sets of magnetoresistance data in

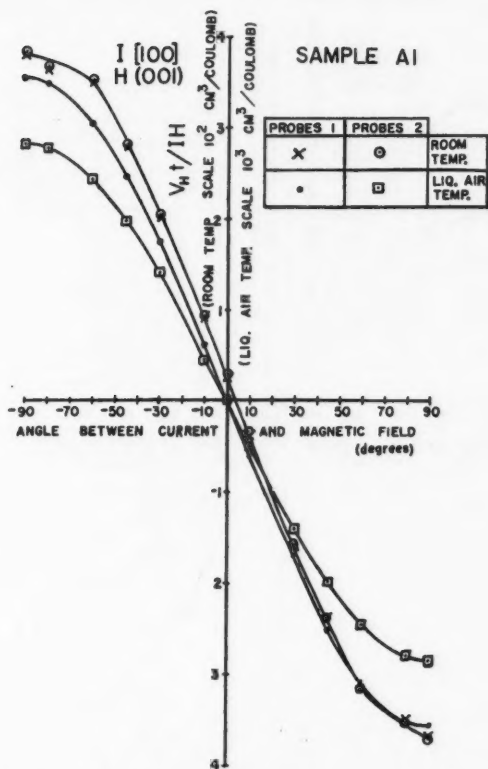


FIG. 9. Variation in sample A1 of the reduced Hall voltage  $10^3 V_H/IH$  for current in the [100] direction with rotation of the magnetic field (4880 gauss) in an (001) plane.

Figs. 5, 6, 7, and 8. The curves show the following features:

- The variation with angle appears to be as  $\sin \theta$ .
- The Hall zeros occur much closer to  $\theta = 0^\circ$  than the corresponding magnetoresistance minima; the largest deviation is about  $6^\circ$  whereas the largest magnetoresistance deviation is about  $25^\circ$ .
- The results on the two sets of probes agree well at room temperature.
- At liquid air temperature, the Hall voltages on the two pairs of probes differ from each other by something like a third. Hence, there is a gradient of electron concentration, at this temperature, of about a third or so in the distance of a probe spacing, which is about 0.15 cm.

The averaged values of the Hall coefficient for the two pairs of probes are given in Table II, together with (zero field) conductivity and Hall mobility values. The conductivities in the three samples are not exactly the same. That in the [100] direction (A1) is rather less than the others. The difference ought not to be directly connected with crystal directions because the cubic symmetry

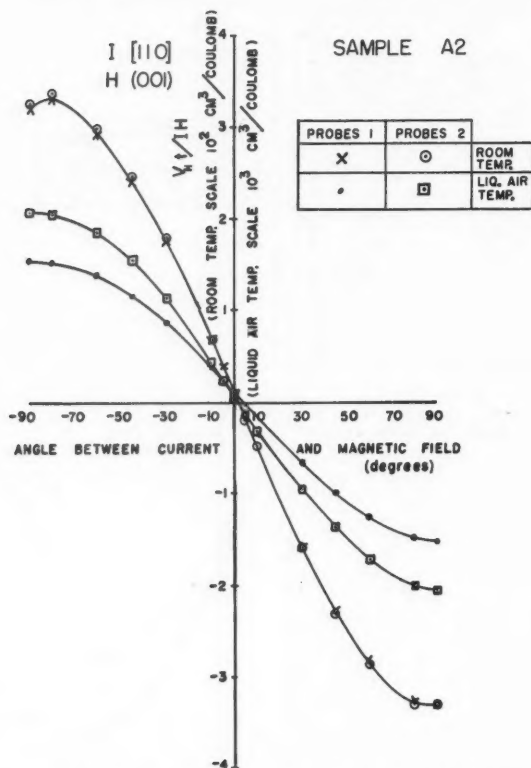


FIG. 10. Variation in sample A2 of the reduced Hall voltage  $10^4 V_{Ht}/IH$  for current in the [110] direction with rotation of the magnetic field (4880 gauss) in an (001) plane.

of the zinc blende lattice implies isotropic conductivity in the absence of external fields. It is rather a matter of an actual difference in the samples themselves. It is clear from the table, in fact, that the conductivity in sample A1 is lower than the other two samples because both the electron concentration and the mobility are smaller; the reason for these two things being smaller is, however, not known.

## 5. DISCUSSION

According to Herring (1955), the longitudinal magnetoresistance vanishes along the principal axes of an ellipsoidal energy surface in  $k$  space. An array of ellipsoids along the  $\langle 100 \rangle$  axes, as in silicon for instance, would give a zero effect along the three directions [100], [010], and [001]. For ellipsoids arrayed along other axes, it would not be possible to find directions which would be parallel to all the principal axes at the same time and so there would be no



TABLE II  
Average conductivity and Hall coefficient values on three oriented samples

Sample	Current direction	Conductivity $\sigma$		Hall coefficient $R_H$ at $H = 4880$ gauss			Hall mobility	
		$\sigma$ at room temp. ( $\Omega^{-1} \text{ cm}^{-1}$ )	$\sigma$ at liq. air temp. ( $\Omega^{-1} \text{ cm}^{-1}$ )	Face on which probes were placed	$R_H$ at room temp. ( $\text{cm}^2/\text{coulomb}$ )	$R_H$ at liq. air temp. ( $\text{cm}^2/\text{coulomb}$ )	$R_H \sigma$ at room temp. ( $\text{cm}^2/\text{v sec}$ )	$R_H \sigma$ at liq. air temp. ( $\text{cm}^2/\text{v sec}$ )
A1	[100]	164	28.2	(001)	$-3.7 \times 10^3$	$-3.18 \times 10^3$	$6.07 \times 10^4$	$8.97 \times 10^4$
A2	[110]	199	55	(001)	$-3.3 \times 10^3$	$-1.79 \times 10^3$	$6.57 \times 10^4$	$9.85 \times 10^4$
		197	53	(110)	$-3.3 \times 10^3$	$-1.77 \times 10^3$	$6.50 \times 10^4$	$9.38 \times 10^4$
A3	[111]	209	53	( $\bar{1}10$ )	$-3.15 \times 10^3$	$-1.77 \times 10^3$	$6.58 \times 10^4$	$9.38 \times 10^4$

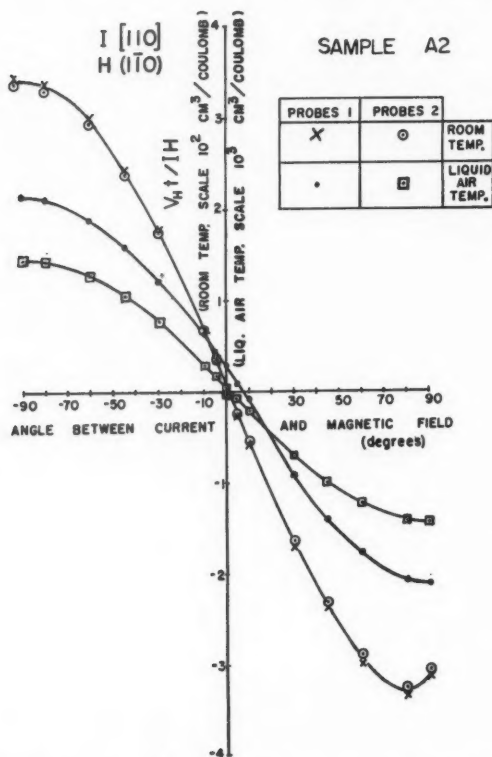


FIG. 11. Variation in sample A2 of the reduced Hall voltage  $10^8 V_H/IH$  for current in the [110] direction with rotation of the magnetic field (4880 gauss) in a (110) plane.

directions of zero magnetoresistance. However, the longitudinal magnetoresistance would be a minimum for certain directions which are nearly parallel to principal ellipsoidal axes. Conversely, the longitudinal magnetoresistance would be a maximum for those directions which are the most skew to the principal axes. Consideration of the theoretical results of Shibuya (1954) for just the  $\langle 100 \rangle$ ,  $\langle 110 \rangle$ , and  $\langle 111 \rangle$  directions shows that of these the directions of greatest magnetoresistance are the  $\langle 111 \rangle$  directions for a model (a) with ellipsoids along  $\langle 100 \rangle$  axes,  $\langle 100 \rangle$  or  $\langle 110 \rangle$  for (b) ellipsoids along  $\langle 110 \rangle$  axes, and  $\langle 100 \rangle$  for (c) ellipsoids along  $\langle 111 \rangle$  axes.

The experimental results shown in Table I appear, from the above considerations, to be consistent with a model in which the energy surfaces consist of a central sphere and a set of ellipsoids along the  $\langle 111 \rangle$  directions. In other words, the band structure is that postulated by Herman (1955) with the  $\langle 111 \rangle$  minima low enough to be populated, at least above liquid air temperature. This assumed model would predict (Glicksman 1958) for weak fields in the  $\langle 100 \rangle$ ,

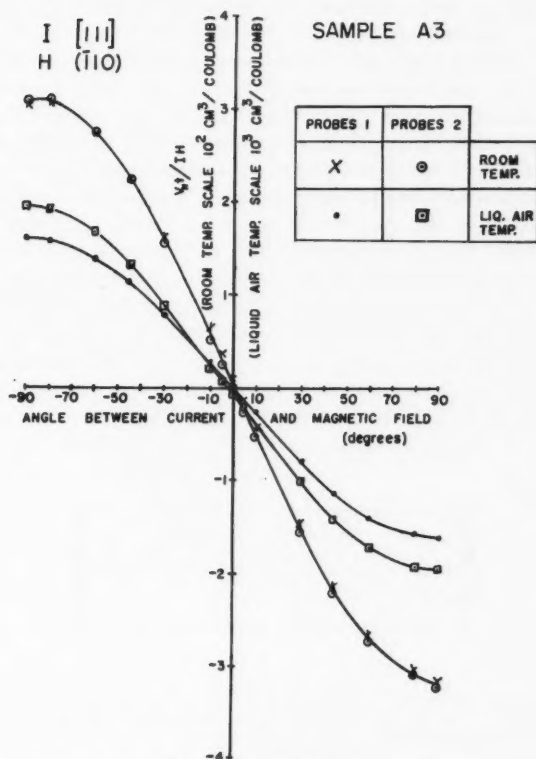


FIG. 12. Variation in sample A3 of the reduced Hall voltage  $10^4 V_{Ht}/IH$  for current in the  $[111]$  direction with rotation of the magnetic field (4880 gauss) in a  $(\bar{1}10)$  plane.

$\langle 110 \rangle$ , and  $\langle 111 \rangle$  directions longitudinal magnetoresistance values in the ratio 6:3:2 respectively.\* For strong fields, the relative values would depend to a certain extent on  $K$ , the ratio (Abeles and Meiboom 1954) of the longitudinal to the transverse mass for the electrons in the ellipsoids. For instance, taking the saturation longitudinal magnetoresistance coefficients worked out by Shibuya (1954, in this paper  $K = 1/r$ ), we find the relative values are approximately 10:6:3 for  $K = 0.5$  and 8:3:3 for  $K = 2$ . The transverse magnetoresistance in this model would be almost entirely due to the central spherical energy surfaces. This is borne out by the fact that the transverse values given in Table I appear to have no significant directional dependence. It should be mentioned that anisotropy in the relaxation time could also explain the observed results.

The impurity band in indium antimonide would have to be taken into

\*The ratio would be  $b+c+d : b+c+d/2 : b+c+d/3$  with  $b+c = 0$  using the notation of Glicksman (1958).

account in inferring band structure from the experimental data. It is not known how this could be done but one could hazard a guess that the impurity band would have an isotropic average mass and would "add" to the central minimum.

In addition to the trends shown in Table I, the results exhibit marked evidence of inhomogeneity in the samples. This is shown up by the effects (b), (d), (e), and (f) of Section 4.1 and effects (b) and (d) of Section 4.2. Further evidence for inhomogeneity is the fact that sometimes, in the taking of the potentiometer measurements, the relative values of the readings at zero magnetic field would change order in going from room temperature to liquid air temperature. The deviations of the magnetoresistance minima from  $\theta = 0^\circ$  cannot be due to error in alignment because the Hall zeros occur much nearer the origin. For the same reason deviations cannot be due predominately to currents flowing in directions not parallel to the sample axis. However, the negative effects can be explained on the basis of the following idealized model. Let us suppose a sample consisted of two halves of different conductivity joined together as in Fig. 13. The current in the absence of a magnetic field

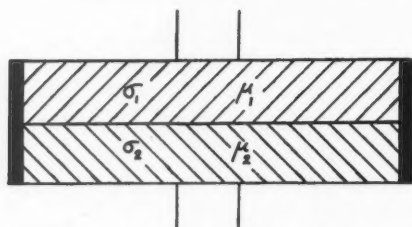


FIG. 13. Hypothetical sample with one half having a different conductivity from the other half. Redistribution of the current in such a sample in the presence of a magnetic field could lead to an apparent negative magnetoresistance.

would divide itself in the ratio of the conductances of the two halves. Now in the presence of a magnetic field the current would redistribute itself. For instance, if the upper part had a higher mobility than the lower part, it would have a larger magnetoresistance effect and so it would receive less current in the presence of a magnetic field. The lower half would at the same time receive more current. Thus the probes on the upper half would show an apparent increase in the magnetoresistance and those on the lower half would show a reduced or even a negative apparent magnetoresistance. In fact the samples have probably a more complex form of conductivity inhomogeneity than the one just considered but the same general effect would occur.

It is possible that the observed anisotropy in the longitudinal magnetoresistance could also be due in some way to inhomogeneity and not to band structure. However, the larger longitudinal effect in sample A1 cannot be attributed to a larger mobility. Table II shows in fact that the Hall mobility is smaller than for the other two samples. Furthermore, the transverse effect in this sample is not significantly different from the values on the other two samples. Nevertheless, it is hoped to repeat, in the near future, measurements

on another [100] sample cut from the same ingot. Definite existence of the anisotropy cannot be really decided upon until such measurements have been made on a number of *n*-type indium antimonide crystals.

#### ACKNOWLEDGMENTS

The author wishes to thank Professor G. A. Woonton and Dr. R. Stevenson of the Eaton Electronics Research Laboratory for making the work possible and to the U.S. Office of Naval Research and the Defence Research Board of Canada for financial assistance.

#### REFERENCES

- ABELES, B. and MEIBOOM, S. 1954. *Phys. Rev.* **95**, 31.  
ARGYRES, P. N. and ADAMS, E. N. 1956. *Phys. Rev.* **104**, 900.  
BATE, R. T., WILLARDSON, R. K., and BEER, A. C. 1959. *J. Phys. Chem. Solids*, **9**, 119.  
BURSTEIN, E., PICUS, G. S., and GEBBIE, H. A. 1956. *Phys. Rev.* **103**, 825.  
DRESSELHAUS, G., KIP, A. F., KITTEL, C., and WAGONER, G. 1955. *Phys. Rev.* **98**, 556.  
FREDERIKSE, H. P. R. and HOSLER, W. R. 1957. *Phys. Rev.* **108**, 1136.  
GLICKSMAN, M. 1958. *Progress in semiconductors*, Vol. 3 (John Wiley and Sons Inc., New York), p. 7.  
HASLETT, J. C. and LOVE, W. F. 1959. *J. Phys. Chem. Solids*, **8**, 518.  
HERMAN, F. 1955. *J. Electronics*, **1**, 103.  
HERRING, C. 1955. *Bell System Tech. J.* **34**, 237.  
KEYES, R. J., ZWERDLING, S., FONER, S., KOLM, H. H., and LAX, B. 1956. *Phys. Rev.* **104**, 1804.  
KEYES, R. W. and SLADEK, R. J. 1956. *J. Phys. Chem. Solids*, **1**, 143.  
MANSFIELD, R. 1955. *J. Electronics*, **1**, 175.  
PEARSON, G. L. and SUHL, H. 1951. *Phys. Rev.* **83**, 768.  
PEARSON, G. L. and TANENBAUM, M. 1953. *Phys. Rev.* **90**, 153.  
SHIBUYA, M. 1954. *Phys. Rev.* **95**, 1385.  
TANENBAUM, M., PEARSON, G. L., and FELDMAN, W. L. 1954. *Phys. Rev.* **93**, 912.

---

## NOTES

---

### STRUCTURE OF THE LINE AT 2892 GAUSS CM IN THE CONVERSION ELECTRON SPECTRUM OF THE ACTIVE DEPOSIT OF $\text{RdTh}^*$

J. L. WOLFSON

The conversion electron spectrum of the active deposit of  $\text{RdTh}$  has been the subject of exhaustive study for several decades. Ellis (1932, 1934), Surugue (1937, 1938), Flammersfeld (1939), Martin and Richardson (1948), Elliott *et al.* (1954*a, b, c, d, e*), Krisiuk *et al.* (1956), Vorob'ev *et al.* (1957), Zhernovoi *et al.* (1957) have all made comprehensive measurements of the momenta and intensities of the numerous conversion lines in the spectrum. A curious feature of this spectrum is the existence of a complex line at 2892 gauss cm, known in the notation of Ellis (1932) as the  $M$  line. This line has long been known to consist of the  $K$  conversion line of a 583-keV transition, and the  $L$  conversion lines of a 511-keV transition, both occurring in  $\text{Pb}^{208}$ . The difference in transition energies is coincidentally so closely the same as the difference between the  $K$  and  $L$  binding energies in  $\text{Pb}$  that the separate lines have never been resolved. This has led in turn to uncertainty as to the relative intensities of the corresponding electron groups.

The means for effecting a resolution of the lines recently became available with the construction of the 100 cm  $\pi\sqrt{2}$  air core magnetic electron spectrometer at the Chalk River Laboratories of the Atomic Energy of Canada Limited (Graham, Ewan, and Geiger 1960). With the permission and co-operation of the Chalk River scientists the author was recently given the opportunity of attempting the resolution of these lines.

The source was prepared by collecting active deposit of  $\text{RdTh}$  on a disk of aluminum, 0.5 mm thick. The deposit was confined to a rectangular region 2 cm in length and approximately 0.5 mm in width by masking the face of the disk with adhesive vinyl tape which was afterwards removed. The source was left uncovered for purposes of this measurement. The spectrometer was adjusted for an instrumental line width of approximately 0.015% in momentum at half maximum intensity, and the study began by observing the  $\gamma$  511  $K$  line at  $2607.17 \pm 0.30$  gauss cm (Lindstrom 1955). The more detailed study of the line group at 2892 gauss cm which was subsequently made is shown in Fig. 1.

It will be observed that the  $\gamma$  511  $L$  conversion lines have been quite well though not completely resolved from the more intense  $\gamma$  583  $K$  conversion line. Mechanical resolution was effected using the line shape of the  $\gamma$  511  $K$  conversion line as a guide. The greater width of the  $\gamma$  583  $K$  line as compared with the  $\gamma$  511  $L$  lines is ascribed to the greater width of the  $K$  shell atomic level in  $\text{Pb}$  as compared with the  $L$  subshells.

\*Issued as N.R.C. No. 6167.

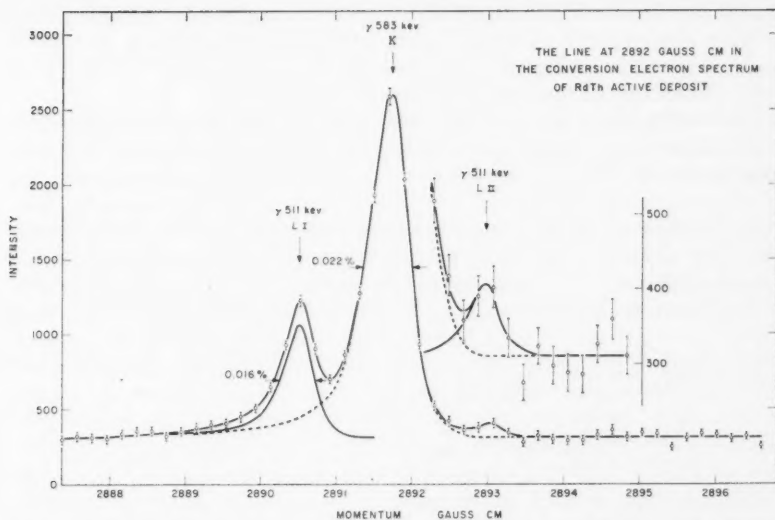


FIG. 1. The separate lines are shown after subtraction of the  $\gamma$  583 K line. The dashed lines represent the  $\gamma$  583 K line in the region of the L lines, as found using the accurately measured shape of the  $\gamma$  511 K line as a guide. The insert shows the  $\gamma$  511  $L_{II}$  line with ordinate scale expanded five times. The vertical bars give the standard deviations of the plotted points.

Using the  $\gamma$  511 K line as calibration point for both momentum and intensity,<sup>1</sup> the following information is obtained from Fig. 1:

Line	$B\rho$ (gauss cm)	$E_e$ (kev)	$E_\gamma$ (kev)	Relative intensity
$\gamma$ 511 K	$2607.17 \pm 0.30$	$422.84 \pm 0.08$	$510.84 \pm 0.08$	1.000
$\gamma$ 583 K	$2891.74 \pm 0.32$	$495.33 \pm 0.08$	$583.33 \pm 0.08$	$0.687 \pm 0.014$
$\gamma$ 511 $L_I$	$2890.50 \pm 0.36$	$495.01 \pm 0.09$	$510.87 \pm 0.09$	$0.173 \pm 0.014$
$\gamma$ 511 $L_{II}$	$2892.99 \pm 0.40$	$495.65 \pm 0.10$	$510.85 \pm 0.10$	$0.021 \pm 0.006$

The transition energies  $E_\gamma$  listed in column 4 were deduced using the critical X-ray absorption energy values given by Hill (1955).

It is of interest to examine these results in the light of the values of conversion coefficients calculated by Sliv and Band (1956, 1958). For the 511-kev transition, the ratio of intensities  $L_I$  to  $L_{II}$  is 8.2 (+3.5 or -1.9) which corresponds to an intensity ratio  $E2$  to  $M1$  radiation of 0.12 (-0.12 or +0.25). Theoretical values for the  $K/L_I$  ratio lie between 6.26 and 6.70 for all mixtures of  $E2$  and  $M1$  radiation, having the lowest value, 6.26, for pure  $M1$  radiation. The experimental value, 5.8 (+0.5 or -0.4), is about 8% lower than this. For this

<sup>1</sup>The ratio of the intensity of the line group at 2892 gauss cm to that of the  $\gamma$  511 K line was not accurately measured in this experiment. The value used, viz.  $0.881 \pm 0.010$ , is the mean of the value 0.888 found by Krišniuk *et al.* (1956), and that found by Elliott *et al.* (1954e),  $0.874 \pm 0.012$ .

transition, Wood and Jastram (1955) measured the intensity ratio  $E2/M1$  to be  $0.04 \pm 0.02$  while Emery and Kane (1960) found a value of  $0.18 \pm 0.15$ . Using the results of Elliott *et al.* (1954*d*) one arrives at a value of 0.4 ( $+0.4$  or  $-0.2$ ), based on the measured  $K$  conversion coefficient.<sup>2</sup>

For the 583-keV transition it is known that the radiation is pure  $E2$  (Elliott *et al.* 1954*a*). The experimental  $K/L$  ratio,<sup>3</sup>  $3.36 \pm 0.12$ , is in good agreement with the theoretical  $E2$  ratio of 3.43.

The author is indebted to the scientific and technical staff of the Atomic Energy of Canada Limited for their generous co-operation and assistance. It is a pleasure also to acknowledge critical discussions of the results with Drs. L. G. Elliott, R. L. Graham, and G. T. Ewan of the Chalk River Laboratories.

- ELLIOTT, L. G., GRAHAM, R. L., WALKER, J., and WOLFSON, J. L. 1954*a*. Phys. Rev. **93**, 356.  
 ——— 1954*b*. Phys. Rev. **94**, 795A.  
 ——— 1954*c*. Proc. Roy. Soc. (Can.) **48**, 12A.  
 ——— 1954*d*. Nuclear Data Sheets, Natl. Acad. of Sciences.  
 ——— 1954*e*. Unpublished.  
 ELLIS, C. 1932. Proc. Roy. Soc. A, **138**, 318.  
 ——— 1934. Proc. Roy. Soc. A, **143**, 350.  
 EMERY, G. T. and KANE, W. R. 1960. Phys. Rev. **118**, 755.  
 FLAMMERSFELD, A. 1939. Z. Physik, **114**, 227.  
 GRAHAM, R. L., EWAN, G. T., and GEIGER, J. S. 1960. Submitted for publication in Nucl. Inst. and Methods.  
 HILL, R. D. 1955. In Beta and gamma ray spectroscopy, edited by K. Siegbahn (North-Holland Publishing Company, Amsterdam), p. 914.  
 KRISIUK, E. M., VITMAN, A. D., VOROB'EV, V. D., LATYSHEV, G. D., and SERGEEV, A. G. 1953. Izvest. Akad. Nauk. S.S.S.R. **20**, 877 (Translation: Bull. Acad. Sci. U.S.S.R. **20**, 797).  
 LINDSTROM, G. 1955. In Beta and gamma ray spectroscopy, edited by K. Siegbahn (North-Holland Publishing Company, Amsterdam), p. 920.  
 MARTIN, D. and RICHARDSON, H. 1948. Proc. Roy. Soc. A, **195**, 287.  
 ROSE, M. E., GOERTZEL, G. H., and PERRY, C. L. 1951. Oak Ridge National Laboratory Report ORNL-1023.  
 SLIV, L. A. and BAND, I. M. 1956. Leningrad Physico-Technical Institute Report (Translation: Report 57 ICC K1, Physics Dept., University of Illinois, Urbana, Illinois).  
 ——— 1958. Akad. Nauk. S.S.S.R. Physico-Technical Institute, Moscow.  
 SURUGUE, J. 1937. Ann. phys. **8**, 484.  
 ——— 1938. J. phys. radium, **9**, 438.  
 VOROB'EV, V. D., IL'IN, K. I., KOL'CHINSKAIA, T. I., LATYSHEV, G. D., SERGEEV, A. G., TROFINOV, Iu. N., and FADEEV, V. I. 1957. Izvest. Akad. Nauk. S.S.S.R. **21**, 954 (Translation: Bull. Acad. Sci. U.S.S.R. **21**, 956).  
 WOOD, G. T. and JASTRAM, P. S. 1955. Phys. Rev. **100**, 1237A.  
 ZHERNOVOI, A. I., KRISIUK, E. M., LATYSHEV, G. D., REMENNYI, A. S., SERGEEV, A. G., and FADEEV, V. I. 1957. Soviet Phys. JETP **5**, 563.

RECEIVED NOVEMBER 28, 1960.

X-RAYS AND NUCLEAR RADIATIONS SECTION,  
 DIVISION OF APPLIED PHYSICS,  
 NATIONAL RESEARCH COUNCIL,  
 OTTAWA, CANADA.

<sup>2</sup>This is the value obtained using the theoretical conversion coefficients of Sliv and Band (1956). The value quoted in the reference, viz.  $\delta^2 = 1.0 \pm 0.4$ , was found using the older theoretical conversion coefficients calculated by Rose, Goertzel, and Perry (1951) without making allowance for finite nuclear size.

<sup>3</sup>The intensity of the  $\gamma$  583 L line relative to that of the  $\gamma$  511 K line has been taken as the mean of the value 0.207 found by Krišuk *et al.* (1956), and that found by Elliott *et al.* (1954*e*),  $0.201 \pm 0.007$ .



## LINEARLY POLARIZED GAMMA RAYS FROM NUCLEAR REACTIONS\*

A. E. LITHERLAND AND H. E. GOVE

The purpose of this note is to point out that a measurement which has been made on gamma rays following  $\beta$ -decay and following Coulomb excitation can also readily be applied to gamma rays from nuclear reactions. The measurement in question is that of the degree of linear polarization of the gamma rays. It is interesting to note, furthermore, that such gamma rays are often strongly linearly polarized. By choosing a suitable reaction it is, in fact, possible to produce monoenergetic gamma rays which are nearly 100% linearly polarized and of a source strength limited only by beam current and target life. A good example (Litherland and Gove 1958) is the  $\text{Mg}^{24}(pp'\gamma)\text{Mg}^{24}$   $Q = -1.37$  Mev reaction at the two prominent resonances at 2.01 and 2.43 Mev bombarding energy. It can be shown, from the equations given in the review article on "Polarization of Nuclear Gamma Rays" by Fagg and Hanna (1959) and the relevant angular distribution coefficients given by Litherland *et al.* (1956), that at  $90^\circ$  to the incident beam of protons the 1.37-Mev gamma rays are very nearly 100% polarized at each resonance. This prediction has been checked at both resonances in the reaction by using the sensitivity of the angular distribution of the Compton scattering process to the plane of polarization of the gamma rays (Fagg and Hanna 1959).

Figure 1 shows the results of an experiment which was carried out to demonstrate the high degree of linear polarization of the gamma rays at the 2.01-Mev resonance in the  $\text{Mg}^{24}(pp'\gamma)\text{Mg}^{24}$  reaction. A small NaI(Tl) crystal, A, 1.25 in. in diameter by 1 in. long was placed with its front face 2.75 inches below the target spot. A 3-in. diameter by 3-in. long NaI(Tl) crystal, B, was placed 12 inches away from the axis of the small crystal, A, on a mount which permitted the crystal B to rotate about the small crystal in the manner shown in Figs. 1(a) and 1(b). The average angle of scattering of the gamma rays was close to  $90^\circ$ . Pulses from the recoil Compton electrons in crystal A were put into coincidence with the pulses from the scattered gamma rays detected in crystal B. The coincidence pulse opened a linear gate which permitted the pulses from the crystal A to be displayed on a 100-channel kicksorter. Figures 1(a) and 1(b) show coincidence spectra at  $\phi = 0^\circ$  and  $\phi = 90^\circ$  respectively. Figure 1(c) shows the angular correlation of the counts recorded in the peak of the spectra. The coefficients of this angular correlation can be related to the coefficients of the angular distribution of the gamma rays with respect to the beam of protons. The angular distribution of the gamma rays can be expressed as a Legendre polynomial series

$$W(\theta) = a_0 + a_2 P_2(\cos \theta) + a_4 P_4(\cos \theta).$$

If the gamma ray is pure electric quadrupole and is observed at  $90^\circ$  to the beam then the ratio  $P$ , of the linear polarization intensity parallel to the plane

\*Issued as A.E.C.L. No. 1179.

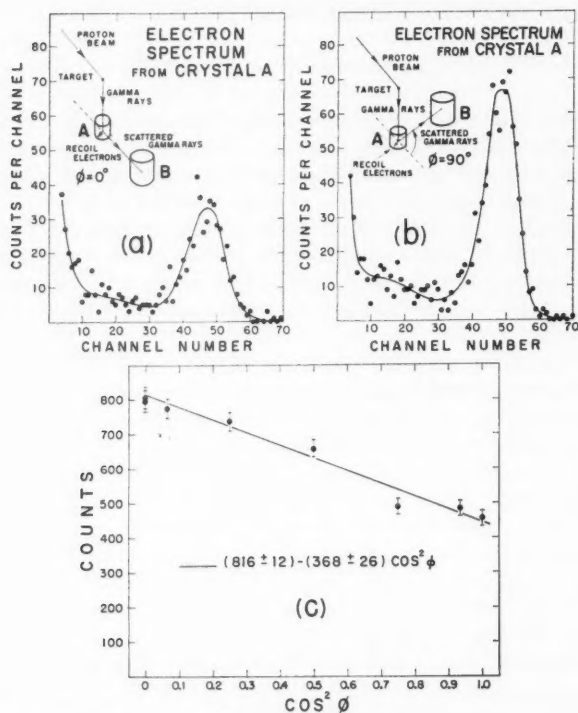


FIG. 1. (a) and (b) show the geometrical arrangement of counters used to measure the linear polarization of the gamma rays from the nuclear reaction  $\text{Mg}^{24}(pp'\gamma)\text{Mg}^{24}$   $Q = -1.37$  Mev at the resonance at 2.01 Mev. Also shown are the pulse spectra from counter A taken in coincidence with pulses from counter B at  $\phi = 0^\circ$  and  $\phi = 90^\circ$ . (c) shows the measured angular correlation together with the results of a least squares fit to the points.

defined by the reaction divided by the linear polarization intensity perpendicular to the plane of the reaction, is given by equation (1),

$$(1) \quad P = \frac{a_0 + a_2 + a_4}{a_0 - 2a_2 - \frac{1}{4}a_4}.$$

For the Compton polarimeter shown in Figs. 1(a) and 1(b) the number of coincidence counts at  $\phi = 90^\circ$  divided by the number of coincidence counts at  $\phi = 0^\circ$  is given by equation (2),

$$(2) \quad \frac{N(90^\circ)}{N(0^\circ)} = \frac{P+S}{PS+1}.$$

In equation (2),  $S$  is the differential Compton scattering cross section parallel to the electric vector of the radiation to the cross section perpendicular to the electric vector for the geometrical arrangement of counters used in the experiment.  $S$  can be evaluated from the expressions given by Fagg and Hanna (1959).

An analysis of the data shown in Fig. 1(c) yields an experimental value for  $P$  of  $16_{-7}^{+54}$  using a value of  $S = 0.50 \pm 0.03$ . The value of  $P$  derived from the angular distribution coefficient quoted by Litherland *et al.* (1956) and corrected for the effects of finite geometry ( $a_z/a_0 = 0.45 \pm 0.02$ ) is  $14.5_{-5}^{+10}$ . These values of  $P$  imply that the electric vector lies predominantly in the plane defined by the reaction, which is in agreement with the known electric quadrupole nature of the 1.37-Mev gamma ray. Similar agreement was also obtained between the linear polarization measurements and the angular correlation measurements of the 1.37-Mev gamma ray at the 2.43-Mev resonance.

Preliminary measurements (Litherland and Gove 1958) have been made of the linear polarization of the 1.64-Mev gamma ray from the second excited state of  $N^{14}$  and of the 0.94-Mev gamma ray from the first excited state of  $F^{18}$  (Kuehner *et al.* 1961). The reactions employed were  $C^{12}(He^3, p)N^{14}$  and  $O^{16}(He^3, p)F^{18}$  respectively. The 0.94-Mev level in  $F^{18}$  was shown to have the same parity as the ground state and the 3.95-Mev level in  $N^{14}$  was shown to have the same parity as the first-excited state at 2.31 Mev.

In conclusion, measurements of the linear polarization and angular distributions of gamma rays from such reactions as  $Mg^{24}(pp'\gamma)Mg^{24}$  can yield the parity change of the gamma-ray transition and can, when combined with other data such as angular distributions from capture reactions, yield in principle unambiguous information on dipole-quadrupole admixtures.

FAGG, L. W. and HANNA, S. S. 1959. *Revs. Modern Phys.* **31**, 711.

KUEHNER, J. A., ALMQVIST, E., and BROMLEY, D. A. 1961. To be published.

LITHERLAND, A. E. and GOVE, H. E. 1958. *Bull. Am. Phys. Soc. Ser. II*, **3**, 200.

LITHERLAND, A. E., PAUL, E. B., BARTHOLOMEW, G. A., and GOVE, H. E. 1956. *Phys. Rev.* **102**, 208.

RECEIVED DECEMBER 8, 1960.

PHYSICS DIVISION,  
ATOMIC ENERGY OF CANADA LIMITED,  
CHALK RIVER, ONTARIO.

## THE DISTANCE CORRELATION BETWEEN PHOTONS IN BLACK BODY RADIATION

F. A. KAEMPFER

One of the macroscopic manifestations of permutation symmetry is the distance correlation between particles of any quantum mechanical system, which may give rise, among other things, to large deviations from the pressure expected in the corresponding classical system. Thus, for an ideal isotropic Bose gas of  $N$  particles per unit volume, with  $\bar{n}_k$  denoting the average occupation number of a quantum state of momentum  $k$ , the average density of particles at distance  $r$  from any given particle,

$$(1) \quad D(r) = D(\infty) \left\{ 1 + \frac{1}{N^2} \left[ \left( \sum_p \bar{n}_p \frac{\sin(k_p r)}{k_p r} \right)^2 - \sum_p \bar{n}_p^2 \right] \right\}$$

where  $D(\infty)$  is the classical value, has been evaluated by London (1943) for the nonrelativistic case in thermal equilibrium, with the result that for temperatures below the Einstein condensation temperature  $T_0 = (1/2\pi m)(N/2.6)^{2/3}$  a long-range correlation proportional to  $1/r$  exists, which can be looked upon as the reason for the drastic reduction in pressure in the ideal Bose gas below  $T_0$  as compared with the pressure in the corresponding Boltzmann gas. For temperatures above  $T_0$  the distance correlation becomes proportional to  $\exp(-r)$ , is of short range, and thus does not affect the macroscopic pressure appreciably.

Expression (1) is still valid in the extreme relativistic case of the photon gas making up black body radiation governed by Planck's law

$$(2) \quad \bar{n}(k) = [\exp(\beta k) - 1]^{-1}$$

where  $\beta = T^{-1}$  is the inverse absolute temperature (natural units  $\hbar = c = (\text{Boltzmann's constant}) = 1$  are used throughout this note). Evaluation of (1) is straightforward if the  $\sum_p$  is replaced by the corresponding integral  $4\pi \int_0^\infty k^2 dk$  in momentum space. Contrary to the case of an ideal gas of massive particles, the number  $\bar{n}_0$  of photons of vanishing energy and momentum is not included in the sum, because the corresponding occupation states are counted as part of the vacuum state, in accordance with the usual convention which yields for the total number of photons present in a unit volume at temperature  $\beta^{-1}$

$$(3) \quad N = \sum_p \bar{n}_p = 4\pi \int_0^\infty \bar{n}(k) k^2 dk = \frac{8\pi}{\beta^3} \zeta(3)$$

where  $\zeta(x)$  is the Riemann zeta function

$$(4) \quad \zeta(x) = \sum_{v=1}^{\infty} v^{-x}.$$

The integrals needed for the evaluation of (1) can be calculated in terms of (2) and (3). One finds

$$(5) \quad \sum_p \bar{n}_p \frac{\sin(k_p r)}{k_p r} = \frac{4\pi}{r} \int_0^\infty \frac{\sin(kr) k dk}{e^{\beta k} - 1} = \frac{N}{\zeta(3)} \sum_{v=1}^{\infty} v^{-3} \left(1 + \frac{r^2}{v^2 \beta^2}\right)^{-2},$$

$$(6) \quad \sum_p \bar{n}_p^2 = -4\pi \left[ \frac{d}{d\lambda} \int_0^\infty \frac{k^2 dk}{e^{\lambda + \beta k} - 1} + \int_0^\infty \frac{k^2 dk}{e^{\lambda + \beta k} - 1} \right]_{\lambda=0} = N \left\{ \frac{\zeta(2)}{\zeta(3)} - 1 \right\}.$$

It is seen that the term

$$(7) \quad \frac{1}{N^2} \sum_p \bar{n}_p^2 = O\left(\frac{1}{N}\right)$$

is negligible, and the density of photons at distance  $r$  from any given photon becomes

$$(8) \quad D(r) = D(\infty) \left\{ 1 + \left[ \frac{1}{\zeta(3)} \sum_{v=1}^{\infty} v^{-3} \left(1 + \frac{r^2}{v^2 \beta^2}\right)^{-2} \right]^2 \right\}.$$

For small  $r$ , i.e.  $r \ll \beta$ ,  $D(r)$  is in first order

$$(9) \quad D(r) = 2D(\infty) \left\{ 1 - \frac{r^2 \zeta(5)}{\beta^2 \zeta(3)} + \dots \right\}$$

and is thus seen to approach twice the classical value in the limit  $r = 0$ . The asymptotic behavior for  $r \gg \beta$ , on the other hand, is obtained if the sum  $\sum_{\nu=1}^{\infty}$  is replaced by the integral  $\int_0^{\infty} d\nu$ . The lower limit of the integral may be taken as zero with impunity, because for large  $r/\beta$  the terms with  $\nu < r/\beta$  contribute nothing to the sum in the limit  $r \rightarrow \infty$ . With

$$(10) \quad \sum_{\nu=1}^{\infty} \nu^{-3} \left( 1 + \frac{r^2}{\nu^2 \beta^2} \right)^{-2} \sim \int_0^{\infty} \frac{\nu d\nu}{[\nu^2 + (r^2/\beta^2)]^2} = \frac{\beta^2}{2r^2}$$

one has thus the asymptotic expression

$$(11) \quad D(r) \sim D(\infty) \left\{ 1 + \frac{\beta^4}{4[\zeta(3)]^2} \frac{1}{r^4} \right\}.$$

Though falling off proportional to  $1/r^4$ , this distance correlation must be classified as being of long range.  $D(r)$  will deviate from  $D(\infty)$  appreciably whenever  $r$  is less than the intermediate value

$$(12) \quad r_1 = \beta^{-1} \approx \lambda_{\max}$$

where  $\lambda_{\max} = (0.288/T)$  cm is the wavelength of the intensity maximum according to Wien's displacement law.

Since  $\lambda_{\max}$  is large compared with atomic dimensions for the case of visible light, there appears to be no fundamental reason why the correlation (9) should not be, in principle, observable with the help of some coincidence technique, in which the number of photon coincidences is measured as a function of the distance of two independent absorbers.

LONDON, F. 1943. J. Chem. Phys. 11, 203.

RECEIVED NOVEMBER 30, 1960.  
DEPARTMENT OF PHYSICS,  
UNIVERSITY OF BRITISH COLUMBIA,  
VANCOUVER 8, B.C.

## LETTERS TO THE EDITOR

*Under this heading brief reports of important discoveries in physics may be published. These reports should not exceed 600 words and, for any issue, should be submitted not later than six weeks previous to the first day of the month of issue. No proof will be sent to the authors.*

### Excitation of the First Negative System of $O_2^+$ by a Proton Beam in Air and Oxygen

The discovery by Vegard (1950a, b, 1952) and by Meinel (1950, 1951) of features in the auroral spectrum excited by fast incoming solar protons (Doppler shifted and broadened Balmer lines of hydrogen) has stimulated a number of laboratory investigations on the excitation of gases by positive ions and electrons. The spectra and other results obtained in these experiments depend significantly upon the pressure of the target gas, and thus a variety of spectral identifications and of temperatures have been published (Smith and Arnot 1930; Branscomb *et al.* 1954; Fan and Meinel 1953; Fan 1956; Roesler *et al.* 1958; Carleton 1957, 1958).

However, in these proton spectra in air, excited at a few millimeters pressure, the  $O_2^+$  first negative system apparently had not appeared. Nevertheless, bands of this system have been recorded in low altitude auroral spectra (Vegard 1950c; Gartlein and Sherman 1952; Dahlstrom and Hunden 1951). It is not certain whether these are excited by the proton or the electron component of the exciting solar particles.

The preliminary results of a further laboratory study reported here concern the excitation of the bands of the  $O_2^+$  first negative ( $b^4\Sigma_g^- - a^4\Pi_u$ ) system by 40-keV proton beams in air and oxygen at low pressures. The resulting emission spectra have been investigated over the pressure range  $10^{-1}$  to  $10^{-3}$  mm Hg, and over the wavelength range 2300 to 7000 Å. A recently constructed 40-to-100 keV accelerator (Reeves 1959) provided the proton beam, and spectroscopic observations were made with Kodak 103a0 and 103aF emulsions, using a Hilger  $f/4$  glass and quartz spectrograph, and a Bausch and Lomb 1.5-meter grating spectrograph.

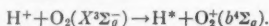
The identified spectral features in air and oxygen are shown in Fig. 1, in which it is seen that the main emitters are  $N^+$ ,  $O^+$ ,  $N_2^+$ , and  $O_2^+$ . It will be noted that nitrogen features show up in the oxygen spectra, because of an intrinsic leakage of air into the collision chamber. More recent spectra, for which the collision chamber was surrounded by an atmosphere of oxygen, do not show these features.

The leading two or three bands in each of the  $\Delta v = -2, -1$ , and 0 sequences of the  $N_2^+$  first negative ( $B^2\Sigma - X^2\Sigma$ ) system, and of the  $\Delta v = -1, 0$ , and  $+1$  sequences of the  $O_2^+$  first negative ( $b^4\Sigma_g^- - a^4\Pi_u$ ) system, are excited together with lines of NII, OII, and HI.

In air, the  $O_2^+$  bands are much weaker than those of  $N_2^+$ . For example, the  $N_2^+$  (0,0) band is easily recorded in a few seconds, while the  $O_2^+$  (0,0) band requires several hundred seconds. Measured rotational temperatures of the  $N_2^+$  bands are close to room temperature over the pressure range  $10^{-1}$  to  $10^{-3}$  mm Hg. The  $O_2^+$  bands in pure oxygen on the other hand are excited very strongly. About 60 seconds exposure is sufficient to record them photographically.

The proton beam is very sharply defined at these low pressures and the bands arise from the center of the beam, evidently from direct proton excitation.

Detailed comments upon possible excitation mechanisms in this and other experiments will shortly be made elsewhere. It does seem likely, however, that a significant contribution is from direct excitation with charge transfer:



- BRANSCOMB, L. N., SHALEK, R. T., and BONNER, T. W. 1954. *Trans. Am. Geophys. Union*, **35**, 107.  
 CARLETON, N. P. 1957. *Phys. Rev.* **107**, 110.  
 ——— 1958. *Conference on Physics of Electronic and Atomic Collisions*, New York Univ., January.  
 DAHLSTROM, C. E. and HUNTER, D. M. 1951. *Phys. Rev.* **84**, 378.  
 FAN, C. Y. 1956. *Phys. Rev.* **103**, 1740.  
 FAN, C. Y. and MEINEL, A. B. 1953. *Astrophys. J.* **118**, 205.  
 GARTLEIN, C. W. and SHERMAN, D. F. 1952. *Mém. soc. roy. sci. Liège*, **12**, 187.  
 MEINEL, A. B. 1950. *Phys. Rev.* **80**, 1096.  
 ——— 1951. *Astrophys. J.* **113**, 583.  
 REEVES, E. M. 1959. Ph.D. Thesis, University of Western Ontario.  
 ROESLER, F. L., FAN, C. Y., and CHAMBERLAIN, J. W. 1958. *J. Atmospheric and Terrest. Phys.* **12**, 200.  
 SMITH, H. D. and ARNOT, E. C. F. 1930. *Phys. Rev.* **36**, 1023.  
 VEGARD, L. 1950a. *Nature*, **114**, 1089.  
 ——— 1950b. *Am. Geophys.* **6**, 157.  
 ——— 1950c. *Compt. rend. acad. sci. Paris*, **230**, 1884.  
 ——— 1952. *Geophys. Publ. (Oslo)* **18**, No. 5.

RECEIVED JANUARY 20, 1961.  
 DEPARTMENT OF PHYSICS,  
 UNIVERSITY OF WESTERN ONTARIO,  
 LONDON, CANADA.

L. HERMAN\*  
 H. I. S. FERGUSON  
 R. W. NICHOLLS

\*Visiting professor, on leave from the Centre National de la Recherche Scientifique, Paris, France.

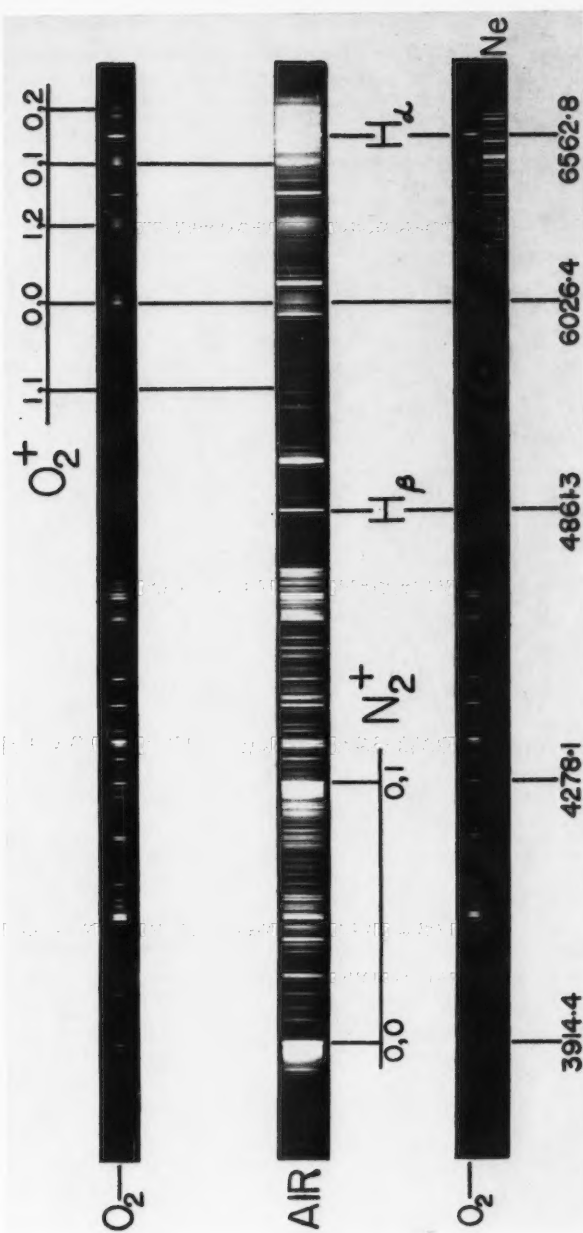
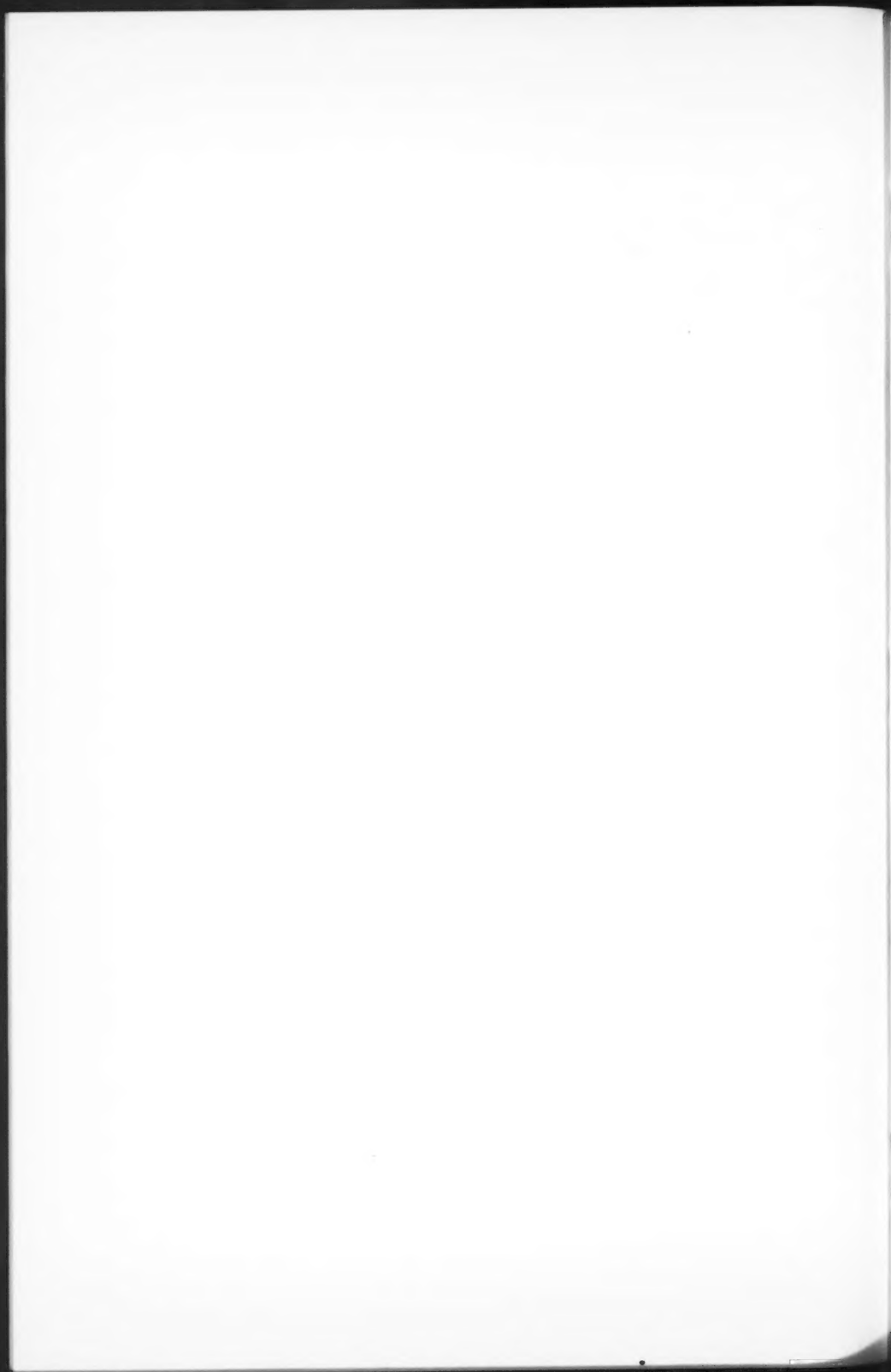


FIG. 1. Spectra excited in air and oxygen by 40-keV protons.





Frequency Measurement of Standard Frequency Transmissions<sup>1, 2</sup>

Measurements are made at Ottawa, Canada, using N.R.C. caesium-beam frequency resonator as reference standard (with an assumed frequency of 9 192 631 770 c.p.s.). Frequency deviations from nominal are quoted in parts per  $10^{10}$ . A negative sign indicates that the frequency is below nominal.

Date, December 1960	MSF, 60 kc/s	GBR, 16 kc/s		WWVB, 60 kc/s
		8½-hour average*	24-hour average†	
1	-154	-159	-158	-151
2	-160	-154	-152	-151
3	-153	-151	-153	N.M.
4	-146	-151	-149	N.M.
5	-150	-148	-146	-149
6	-152	-148	-148	-151
7	-154	-147	-147	-150
8	N.M.	-143	-146	-150
9	-145	-143	-142	-150
10	-145	-140	-143	N.M.
11	-141	-142	-139	N.M.
12	-139	-142	-140	-147
13	-148	-134	-137	-146
14	N.M.	-136	-138	N.M.
15	-151	-136	-136	-150
16	-155	-134	-139	-152
17	N.M.	-141	-149	N.M.
18	N.M.	-145	-146	N.M.
19	-154	-149	-150	N.M.
20	N.M.	-148	-149	N.M.
21	-150	-147	-149	N.M.
22	-144	-141	-144	N.M.
23	-152	-140	-143	N.M.
24	-139	-142	-141	N.M.
25	-136	-140	-141	N.M.
26	N.M.	-138	N.M.	N.M.
27	-136	-137	-138	N.M.
28	-137	-137	-139	N.M.
29	-143	-135	-137	-152
30	-138	-131	-136	-149
31	N.M.	-134	-136	N.M.
Average	-147	-142	-144	-150
Midmonthly mean of WWV	-150			

NOTE: N.M. no measurement.

\*Time of observations: 22.30 to 07.00 U.T.

†From 15.00 to 15.00 U.T.

After 11 November the frequency values published are free from a previously included non-statistical error arising from the leak of high-frequency radiation from the cavity. The stability of the resonator is now believed to be of the order of  $\pm 3 \times 10^{-10}$ . Improvements in the methods of measuring the frequencies of v.l.f. stations is expected to be made in the near future.

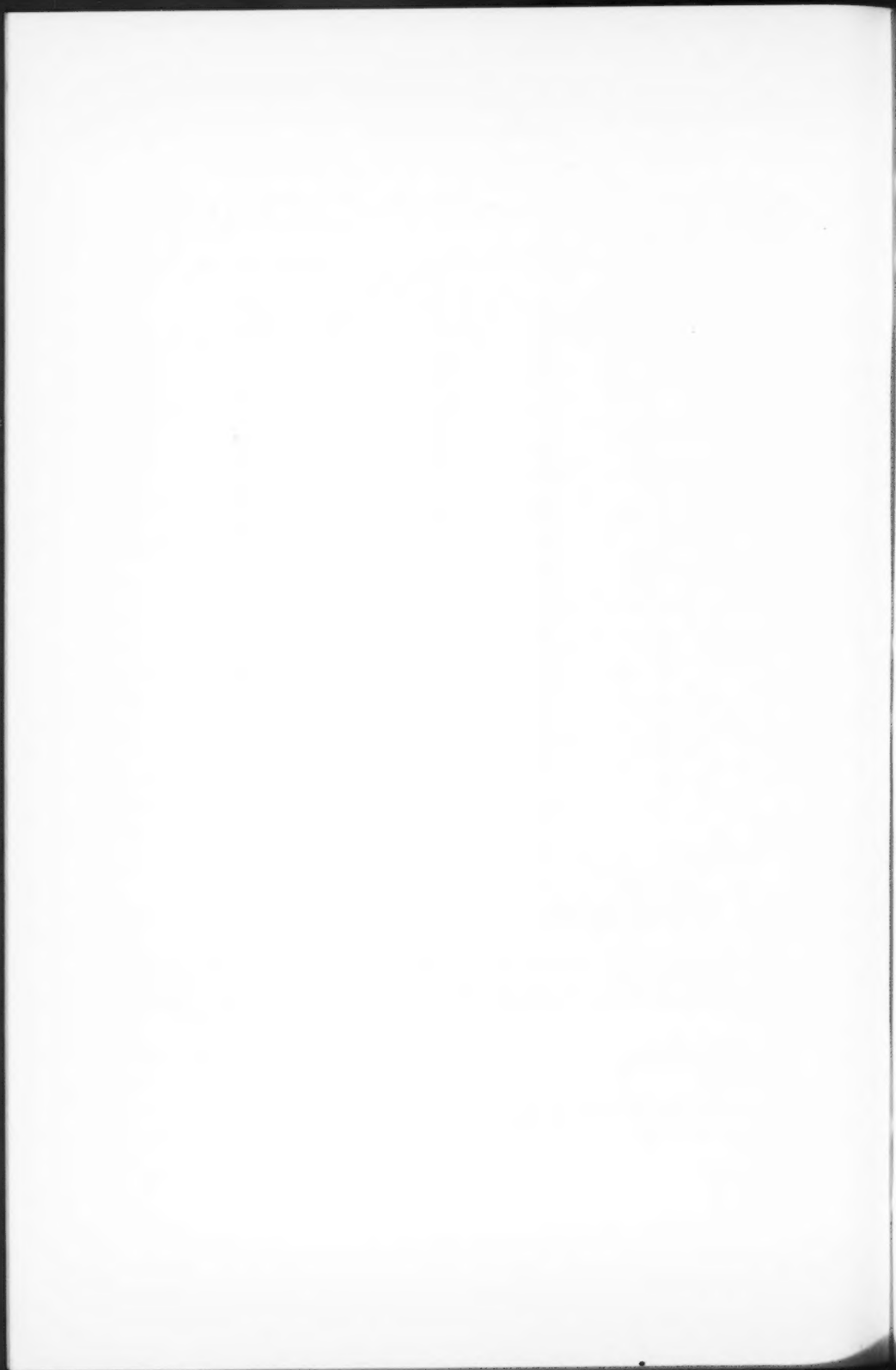
RECEIVED JANUARY 16, 1961.  
DIVISION OF APPLIED PHYSICS,  
NATIONAL RESEARCH COUNCIL,  
OTTAWA, CANADA.

S. N. KALRA

<sup>1</sup>Issued as N.R.C. No. 6169.

<sup>2</sup>Cf. Kalra, S. N. 1959. Can. J. Phys. 37, 1328.

Can. J. Phys. Vol. 39 (1961)







## NOTES TO CONTRIBUTORS

### *Canadian Journal of Physics*

#### MANUSCRIPTS

**General.**—Manuscripts, in English or French, should be typewritten, double spaced, on paper  $8\frac{1}{2} \times 11$  in. **The original and one copy are to be submitted.** Tables and captions for the figures should be placed at the end of the manuscript. Every sheet of the manuscript should be numbered. Style, arrangement, spelling, and abbreviations should conform to the usage of recent numbers of this journal. Greek letters or unusual signs should be written plainly or explained by marginal notes. Characters to be set in boldface type should be indicated by a wavy line below each character. Superscripts and subscripts must be legible and carefully placed. Manuscripts and illustrations should be carefully checked before they are submitted. Authors will be charged for unnecessary deviations from the usual format and for changes made in the proof that are considered excessive or unnecessary.

**Abstract.**—An abstract of not more than about 200 words, indicating the scope of the work and the principal findings, is required, except in Notes.

**References.**—References should be listed **alphabetically by authors' names**, unnumbered, and typed after the text. The form of the citations should be that used in current issues of this journal; in references to papers in periodicals, titles should not be given and only initial page numbers are required. The names of periodicals should be abbreviated in the form given in the most recent *List of Periodicals Abstracted by Chemical Abstracts*. All citations should be checked with the original articles and each one referred to in the text by the authors' names and the year.

**Tables.**—Tables should be numbered in roman numerals and each table referred to in the text. Titles should always be given but should be brief; column headings should be brief and descriptive matter in the tables confined to a minimum. Vertical rules should not be used. Numerous small tables should be avoided.

#### ILLUSTRATIONS

**General.**—All figures (including each figure of the plates) should be numbered consecutively from 1 up, in arabic numerals, and each figure referred to in the text. The author's name, title of the paper, and figure number should be written in the lower left corner of the sheets on which the illustrations appear. Captions should not be written on the illustrations.

**Line drawings.**—Drawings should be carefully made with India ink on white drawing paper, blue tracing linen, or co-ordinate paper ruled in blue only; any co-ordinate lines that are to appear in the reproduction should be ruled in black ink. Paper ruled in green, yellow, or red should not be used. All lines must be of sufficient thickness to reproduce well. Decimal points, periods, and stippled dots must be solid black circles large enough to be reduced if necessary. Letters and numerals should be neatly made, preferably with a stencil (**do NOT use typewriting**) and be of such size that the smallest lettering will be not less than 1 mm high when the figure is reduced to a suitable size. Many drawings are made too large; originals should not be more than 2 or 3 times the size of the desired reproduction. Whenever possible two or more drawings should be grouped to reduce the number of cuts required. In such groups of drawings, or in large drawings, full use of the space available should be made; the ratio of height to width should conform to that of a journal page ( $4\frac{1}{2} \times 7\frac{1}{2}$  in.), but allowance must be made for the captions. **The original drawings and one set of clear copies (e.g. small photographs) are to be submitted.**

**Photographs.**—Prints should be made on glossy paper, with strong contrasts. They should be trimmed so that essential features only are shown and mounted carefully, with rubber cement, on white cardboard, with no space between those arranged in groups. In mounting, full use of the space available should be made. **Photographs are to be submitted in duplicate; if they are to be reproduced in groups one set should be mounted, the duplicate set unmounted.**

#### REPRINTS

A total of 100 reprints of each paper, without covers, are supplied free. Additional reprints, with or without covers, may be purchased at the time of publication.

Charges for reprints are based on the number of printed pages, which may be calculated approximately by multiplying by 0.6 the number of manuscript pages (double-spaced type-written sheets,  $8\frac{1}{2} \times 11$  in.) and including the space occupied by illustrations. Prices and instructions for ordering reprints are sent out with the galley proof.

## Contents

<i>P. Glentworth and R. H. Betts</i> —Production of $\text{Lu}^{178}$ by the $\text{Ta}^{181}(n, \alpha) \text{Lu}^{178}$ reaction in the NRX reactor - - - - -	381
<i>John W. Clark</i> —The role of repulsive cores in the photonuclear effect - -	385
<i>A. Boivin and R. Tremblay</i> —Interféromètre micro-onde à fond cohérent -	393
<i>R. Tremblay</i> —Déphaseur micro-onde à prismes diélectriques - - - -	409
<i>R. A. Olafson, M. A. Thomas, and H. L. Welsh</i> —The Raman spectrum of methane- $d_4$ - - - - -	419
<i>B. A. McIntosh</i> —Analysis of a type of rough-trail meteor echo - - - -	437
<i>A. V. Gold and W. B. Pearson</i> —Phonon drag in lead - - - - -	445
<i>C. H. Champness</i> —Magnetoresistance and Hall effect in oriented single crystal samples of <i>n</i> -type indium antimonide - - - - -	452
 Notes:	
<i>J. L. Wolfson</i> —Structure of the line at 2892 gauss cm in the conversion electron spectrum of the active deposit of $\text{RdTh}$ - - - - -	468
<i>A. E. Litherland and H. E. Gove</i> —Linearly polarized gamma rays from nuclear reactions - - - - -	471
<i>F. A. Kaempffer</i> —The distance correlation between photons in black body radiation - - - - -	473
 Letters to the Editor:	
<i>L. Herman, H. I. S. Ferguson, and R. W. Nicholls</i> —Excitation of the first negative system of $\text{O}_2^+$ by a proton beam in air and oxygen - - -	479
<i>S. N. Kalra</i> —Frequency measurement of standard frequency transmissions	477

